University of Puerto Rico

Faculty of Natural Sciences

Department of Chemistry

Rio Piedras Campus

Cross-linked cytochrome c-based nanoparticles for targeted and controlled cancer therapy

By

Irivette Dominguez Martinez

May 6, 2022

Accepted by the Faculty of Natural Sciences from University of Puerto Rico in Partial

Fulfillment of Requirement to obtain the degree of Doctor in Philosophy

Accepted by the Faculty of Natural Sciences of the Doctoral Program in Chemistry of the University of Puerto Rico in partial fulfillment of the requirements for the degree of

Doctor of Philosophy

_____

Kai H. Griebenow, Ph.D.
Professor of the Department of Chemistry
Thesis Advisor

_____

Arthur Tinoco, Ph.D.
Coordinator of the Chemistry Graduate Program
Thesis Committee Member

_____

Nestor Carballeira, Ph.D.
Dean Faculty of Natural Science
Thesis Committee Member

_____

Yancy Ferrer, Ph.D.
Professor of the Central University of the Caribbean
Thesis Committee Member

_____

Marvin Bayro, Ph.D.
Professor of the Department of Chemistry
Thesis Committee Member

Table of Contents

2. Chapter 2: Materials and Methods

Tables Captions

Figure Captions

Figure 1.1. Estimated new lung and bronchus cancer cases deaths by sex in the United States, 2021. Long-term trends in lung and bronchus cancer incidence (1975-2017) and mortality (1975-2018) rate.

Figure 1.2. Nanoparticle platforms for drug delivery.

Figure 1.3. Passive targeting and active targeting strategies for anticancer drug delivery system. (*Top*) By the EPR effect, NPs passively diffuse through the leaky vasculature and accumulate in tumor tissues. In this case, drug may be released in the extracellular matrix and then diffuse through the tissue (a). (*Down*) In active targeting, once particles have extravasated in the tumor tissue, the presence of targeting ligands (e.g., FA) on the NP surface facilitates their interaction with receptors that are present on tumor cells, resulting in enhanced accumulation and preferential cellular uptake through receptor-mediated endocytosis (b).

Figure 1.4. The reaction of DSP with amine-containing molecules yields amide bond crosslinks. The conjugates may be cleaved by reduction of the disulfide bond in the cross-bridge with GSH.

Figure 1.5. Intrinsic pathway for apoptosis. The intrinsic pathway, typically initiated by DNA damage, activates p53. p53 then activates the pro-apoptotic proteins, which cause mitochondrial outer membrane permeabilization, leading to Cyt c in the cytoplasm. Cyt c associates with Apaf-1 to form the apoptosome complex in the cytoplasm. The apoptosome causes the conversion of inactive pro-caspase-9 into active caspase-9.

Caspase-9 then activates caspase-3, leading to the caspase cascade, resulting in apoptosis.

Figure 1.6. Protein-based nanoparticles prepared by nanoprecipitation method leading to submicron particles. The addition of the non-solvent phase leads to a state of supersaturation which allows the beginning of the nanoprecipitation process and the formation of nanoparticles.

Figure 3.1. Synthesis route of cross-linked Cyt c NP by one-step nanoprecipitation.

Figure 3.2. Effect of cross-linker concentration (DSP) on mean diameter and zeta potential values of cross-linked Cyt c NPs. Data shown are expressed as the mean ± SD of experiments performed in triplicate (n = 3). Statical analysis by ordinary one-way ANOVA with Tukey's multiple comparison analysis demonstrated a significant difference in the mean sizes and zeta potential values of Cyt c NPs cross-linked by different concentrations. The asterisks indicate significant differences: ** $p \leq 0.01$ *** $p = 0.0005$, and **** $p < 0.0001$. No significant (*ns*) differences were observed in mean diameters from 0.2 mg/mL to 0.5 mg/mL and zeta potential values between 1 mg/mL and 1.5 mg/mL of cross-linker concentrations.

Figure 3.3. Effect of cross-linking concentration on morphological characterization of nanoparticles. SEM images of Cyt c NPs cross-liked with different concentration of DSP: (a) 0.2 mg/mL, (b) 0.3 mg/mL, (c) 0.5 mg/mL, (d) 1.0 mg/mL, and (e) 1.5 mg/mL. Scale bar = 1 µm.

Figure 3.4. Effect of non-solvent/cross-linking injection rate on (a) mean size and (a) zeta potential values of cross-linked Cyt c NPs. Data are the mean ± SD of experiments

performed in triplicate (n = 3). Statical analysis by ordinary one-way ANOVA multiple comparison analysis demonstrated a significant difference between cross-linking injection rates on the mean size of NPs. The asterisks (*) indicate significant differences: ** p = 0.002, and **** $p < 0.0001$. No significant (ns) differences in zeta potential values between NPs prepared at different injection rates were observed.

Figure 3.5. Effect of cross-linking injection rate on the morphological characterization of NPs. SEM images of Cyt c NPs cross-linked at different flow rate: (a) 125 mL/h, (b) 200 mL/h, and (c) 300 mL/h. Scale bar = 1 µm.

Figure 3.6. Synthesis route of cross-linked Cyt c NP by two-step nanoprecipitation.

Figure 3.7. The effect of cross-linking method variation on the (a) mean diameter and (b) zeta potential values of cross-linked Cyt c nanoparticles. Data shown are the mean ± SD of experiments performed in triplicate (n =3). The asterisks (*) indicate significant differences: * p = 0.02 and ** p = 0.01, assessed by two-tailed unpaired t-test analysis.

Figure 3.8. SEM micrographs of the Cyt c NPs cross-linked by (a) one-step and (b) two-step nanoprecipitation methods. Cross-linker concentration (0.5 mg/mL DSP) and injection rate (300 mL/h) were maintained constant during nanoparticle formation. Scale bar = 1 µm.

Figure 3.9. Cumulative in vitro release profile of Cyt c from cross-linked Cyt c NPs synthesized by one-step (red circle) and two-step (blue square) methods. NPs were dissolved in PBS buffer with 10 mM GSH at 37°C to simulate the intracellularly (reducing) physiological condition. Data are the mean ± SD of experiments performed in triplicate

(*n*= 3). Statistical analysis by two-tailed paired t-test analysis demonstrated a significant difference between one-step and two-step cross-linking methods, ** $p < 0.05$.

Figure 3.10. Activation of caspase 3/7 using a cell-free caspase assay. (a) Compared to untreated cells (control), cross-linked Cyt c NPs synthesized by one-step and two-step methods activated caspase 3/7 to a similar extent to the activity provided by native Cyt c protein. (b) Relative caspase 3/7 activation of Cyt c NPs cross-linked by one-step and two-step methods compared with the relative activation by native Cyt c. When comparing the relative caspase activity of NPs obtained from one-step and two-step methods, no statistically significant (ns) difference was found using ordinary one-way ANOVA and multiple comparison Tukey's test (95% confidence interval). Data are the mean ± SD of experiments performed in triplicate (*n*= 3); (*** $p = 0.0007$).

Figure 4.1. (a) Synthesis route of cross-linked Cyt c-PEG-FA NPs. SEM micrographs of (b) crosslinked Cyt c NPs and (c) cross-linked Cyt c-PEG-FA NPs. (d) Cumulative in vitro release profile of Cyt c from cross-linked Cyt c-PEG-FA NPs at 37 °C. NPs were dissolved in PBS buffer with zero GSH (triangles), 0.001 mM GSH (squares), and 10 mM GSH (circles) to simulate extracellular (non-reducing) and intracellular (reducing) physiological conditions. Data are the mean ± SD of experiments performed in triplicate. Statistical analysis by ordinary one-way ANOVA multiple comparison analysis demonstrated a significant difference between the intracellular and extracellular conditions when compared with the control, $p < 0.0001$.

Figure 4.2. Activation of caspase 3/7 using a cell-free caspase assay. (a) Compared to untreated cells (control), cross-linked Cyt c-PEG-FA NPs activated caspase 3/7 to a significantly greater extent, similar to the activity provided by the native Cyt c protein. (b)

Caspase 3/7 activation of cross-linked Cyt c-PEG-FA NPs compared with the caspase 3/7 activation by native Cyt c. LLC lysate treated with cross-linked Cyt c-PEG-FA NPs was able to activate the caspase 3/7 significantly, similar to that afforded by native Cyt c. The relative caspase activity offered by cross-linked Cyt c-PEG-FA NPs was not significantly different compared to the native Cyt c protein. **** Indicates a significant difference ($p < 0.0001$) in an unpaired t-test analysis with $n = 6$. Error bars represent the calculated SD.

Figure 4.3. MTS cell viability assay of LLC cells after 24 h of incubation with folate-containing cross-linked Cyt c-PEG-FA NPs in a concentration-dependent manner. The percent of cell viability for the Cyt c-PEG-FA NPs is shown in gray columns, at increasing concentrations from 12.5 to 300 μg/ml. This dose-response curve was used to determine the IC_{50} value of the cross-linked Cyt c-PEG-FA NPs. As controls, we used the native Cyt c (protein alone, no NPs; first black column), PEG-FA (Folate-poly(ethylene glycol)-succinimidyl ester alone; second black column), and Cyt c-DSP NPs (Cyt-c with the homo-bifunctional crosslinker DSP, without folate; gray dotted column). All controls were added at a concentration of (300 μg/ml). Cytotoxicity of the folate-free formulation and the folate-bearing NPs at the highest concentration were compared by unpaired t-test analysis (****, $p< 0.0001$, $n= 9$). Data shown are expressed as the mean ± SD.

Figure 4.4. Comparison of the cytotoxicity of cross-linked Cyt c-PEG-FA NPs in cancerous and non-cancerous cell lines. Cell viability MTS assay after 24 h of NPs treatment at 100 μg/ml using FR-positive cells (LLC and HeLa cells) and FR-negative cells (NIH/3T3 cells). The mean ± SD was obtained from three independent experiments

performed in triplicate. The results were analyzed statistically using an unpaired t-test (****, $p < 0.0001$, n=9).

Figure 4.5. Study of DAPI and propidium iodide (PI) colocalization for the detection of apoptotic cells after 24 h of incubation with cross-linked Cyt c-PEG-FA NPs. (b) Selective induction of apoptosis was observed in LLC cells incubated with NPs. (c) No cellular apoptosis was observed in NIH/3T3 cells when incubated with NPs. (a, d) Untreated LLC and NIH/3T3 cells were used as controls, respectively.

Figure 4.6. Caspase 3/7 activation in LLC cells after 24 h of incubation with 100 µg/ml of cross-linked Cyt c-PEG-FA NPs. The caspase 3/7 activity was assayed by CellEvent™ caspase 3/7 fluorescent green detection reagent and measured by CLSM. (a) The left panel shows untreated LLC cells used as a negative control to establish the green autofluorescence background, and the right panel shows LLC cells treated with the NPs. Scale bar = 25 µm. (b) Quantitative analysis of green fluorescence (488 nm Ex.) in untreated versus NP-treated cells. The results are expressed as mean ± SD and were significantly different (**, $p = 0.003$, unpaired t-test analysis, n =3).

Figure 4.7. Endosomal colocalization of Cyt c-PEG-FA NPs in LLC cells using Z-stack confocal imaging. LLC cells were incubated with FITC-labeled NPs (green fluorescence) at 100 µg/ml concentration and FM-464 endosome marker (red fluorescence) for 24 h. The cell nuclei were stained with DAPI shown in blue. The yellow color indicates the localization of the NPs in the endosomes [1]. Scale bar = 25µm.

Figure 4.8. Internalization of FITC-labeled cross-linked Cyt c-PEG-FA NPs by FR-positive cancer LLC and HeLa cells and FR-negative non-cancer NIH/3T3 cells.

Confocal images of both cells treated with FITC-labeled cross-linked Cyt c-PEG-FA NPs and endosome marker (FM-464) after a 24 h incubation. The yellow color in the merged images indicates the localization of the NPs in the endosomes [1]. Nuclear stain DAPI is shown in blue. Scale bar = 25 μm.

Figure 4.9. Infrared (IR) signal of organs and tumors after injection of IR-labeled-NPs. Upper panel: A high-resolution image of the ventral side of tumors shows what appears to be NPs in the NP-injected mouse tumor but not in the control mouse. Lower left panel: Five min after tail vein injection of IR-labeled nanoparticles or no nanoparticles into LLC tumor-bearing mice, tumors, and organs were excised and scanned for IR signal at 680 nm (high intensity in red and low in blue) using an infrared scanner (LI-COR). Lower right panel: Percentage of IR signal in the organs of an IR-NP-injected mouse after 5 min compared to control.

Figure 4.10. Treatment regime in C57BL/6J mice. Male mice (36-60 weeks) were divided into two groups and treated with: 90% PEG 400/10% ethanol vehicle (i.p.) or 7 mg/kg NPs dissolved in vehicle (i.p.) at days 3 and 8 after tumor implant. Tumor monitoring was performed manually by caliper measurement at days 3, 6, 9, and 12, and weight was monitored as a general health measurement in our mouse model.

Figure 4.11. Percentage of tumor growth and mouse weight in NP-treated and untreated mice. (a) Tumor growth monitoring was performed in male mice manually by caliper measurement. (b) Weight was monitored using a rodent balance. T-test and Kolmogorov-Smirnov post-test on percent tumor growth showed *p= 0.0385,

while animal weight was not significantly different between both groups. Vehicle (n=6) and NP-treated (n=7).

Abbreviations

Apaf-1	Apoptotic protease activator factor 1
CLSM	Confocal laser scanning microscopy
Cyt c	Cytochrome c
DAPI	4’,6-diamidino-2-phenylindole
DDS	Drug delivery system
DLS	Dynamic light scattering
DMEM	Dulbecco's Modified Eagle Medium
DSP	Dithiobis(succinimidyl propionate)
EPR	Enhanced Permeation and Retention effect
FA	Folic acid
FBS	Fetal bovine serum
FDA	Food and drug administration
FITC	Fluorescein isothiocyanate
FR	Folate receptor
GSH	Glutathione
h	Hours
HeLa	Cervical cancer human cell line

LLC	Lewis lung carcinoma cell line
NHS	N-Hydrosuccinimide
NP	Nanoparticle
NSCLC	Non-small cell lung cancer therapy
OS	Overall survival
PBS	Phosphate buffer saline
PEG	Polyethylene glycol
PLGA	Poly(lactide-co-glycolide acid)
PI	Propidium iodide
PS	Performance status
RES	Reticuloendothelial system
RT	Room temperature
SCLC	Small cell lung cancer
SD	Standard deviation
SEM	Scanning electron microscopy
UV-Vis	Ultraviolet/Visible
WHO	World Health Organization
ZP	Zeta potential

Abstract

Cancer is a major public health problem worldwide and is the second leading cause of death in the United States. The persistent need to develop cancer therapeutics with improved safety and efficacy provides constant fuel to drive the development and optimization of protein-based therapeutics [2]. Proteins are an excellent natural building block for drug delivery systems (DDS) fabrication due to their unique advantages [3]. They are naturally produced by the body and often well tolerated with poorly immunogenicity. Therefore, proteins that exhibit potent cytotoxic activities are also attractive substitutes for cytotoxic drugs because they are highly specific and less toxic than conventional small drug molecules. In this context, cytochrome c (Cyt c) has drawn attention to cancer research because it is non-toxic, and when delivered to the cytoplasm of cancer cells, it can kill them by inducing apoptosis. Various nano vehicles have been explored to protect the sensitive load and facilitate the intracellular delivery of protein therapeutics with different degrees of success. Recently, our research group overcame biocompatibility and off-target limitations commonly seen in anticancer therapeutics by designing a Cyt c-based DDS coated with a biodegradable polymer, PLGA-PEG-FA, which is 253 nm in size [4]. However, this delivery system showed no cytotoxicity after an in vivo injection using a lung carcinoma immune-competent mouse model. For the in vivo application, it has been reported that spherical particles that are 100-200 nm in size have the highest potential for prolonged circulation because they are large enough to avoid uptake in the liver but small enough to prevent filtration to the spleen. In addition, the folate receptor alpha (FR) is overexpressed in 40% of human cancers, including non-small cell lung carcinoma (NSCLC), and can be utilized for active tumor targeting to afford more effective

cancer therapies. Therefore, this dissertation aims to develop a redox-sensitive protein-based nanoparticle (NP) that uses Cyt c as a drug and carrier material for targeted and controlled cancer therapy.

In *Chapter 3*, we substantially simplify our previously reported system by employing another strategy for preventing protein dissolution in buffer and blood, which uses a homo-bifunctional redox-sensitive cross-linking, dithiobis(succinimidyl propionate) (DSP). This cross-linker contains a disulfide bond that is reduced under intra-cellular conditions, thus affording the dissolution of the NPs in the cytoplasm of target cells. It is reported that the non-solvent nanoprecipitation method is an easy and reproducible technique to prepare Cyt c NPs. However, the size, size distribution, surface charge, and delivery properties of nanoparticles are highly influenced by the nanoprecipitation operation process conditions such as protein concentration [4], cross-linker concentration [5], and injection rate [6]. Therefore, this chapter aims to optimize the nanoprecipitation method to establish a simpler and straightforward method for preparing cross-linked nanoparticles based on a single step with controllable size and distribution for delivery applications. Special attention has been dedicated to a systematic study to understand the effect of the operating parameters of the one-step nanoprecipitation method, such as cross-linker concentration, non-solvent/cross-linking injection rate, and method variation (i.e., one-step vs. two-step) on the physicochemical and delivery properties of the nanoparticles. To the best of our knowledge, this is the first work investigating the impact of the cross-linking process on the preparation of Cyt c-based nanoparticles by the nanoprecipitation process. Our results demonstrated that an increase in cross-linker concentration led to an increase in NP size and a decrease in zeta potential. In addition,

the diameter of cross-linked Cyt c NPs decreases as the cross-linking/nanoprecipitation rate increases. For Cyt c NPs cross-linked with the one-step method, the mean size was smaller (179 ± 4 nm) than the two-step method (189 ± 2 nm) (*p = 0.02). However, the two-step nanoprecipitation method demonstrated a more efficient release profile, with 71% of Cyt c released in the initial 24 h compared with the 40% of the one-step method. Finally, for both methods, the activity of the encapsulated Cyt c is mainly conserved after the cross-linking process. Therefore, it can be concluded that the non-solvent nanoprecipitation method using a one-step or two-step cross-linking approach presents an excellent opportunity for the smart delivery of Cyt c as a therapeutic protein for cancer treatment.

In *Chapter 4*, we select the two-step method to prepare the folate-decorated cross-linked Cyt c NPs because they present a more efficient drug release profile than the one-step method. To achieve receptor-mediated internalization by FR-overexpressing cancer cells, we conjugated folate-poly(ethylene glycol) (FA-PEG) to the surface of the NPs. Cyt c nanoparticles (NPs, 169 ± 9 nm) were obtained by solvent precipitation with acetonitrile and then stabilized by reversible homo-bifunctional cross-linking to accomplish a Cyt c-based drug delivery system combines stimulus-responsive release and active targeting. Cyt c was released under intracellular redox conditions due to an S-S bond in the NPs linker, while NPs remained intact without any release under extracellular conditions. The NP surface was decorated with a hydrophilic folic acid–polyethylene glycol (FA-PEG) polymer for active targeting. The FA-decorated NPs specifically recognized and killed cancer cells (IC_{50} = 47.46 μg/mL) that overexpressed FR but showed no toxicity against FR-negative cells. Confocal microscopy confirmed the preferential uptake and apoptosis

induction of our NPs by FR-positive cancer cells. In vivo experiments using a Lewis lung carcinoma (LLC) mouse model showed visible NP accumulation within the tumor and inhibited the growth of LLC tumors. Our data demonstrate a substantial improvement over our previous Cyt c delivery system both in vitro, using the Lewis lung carcinoma (LLC) cell line, and in vivo, using the LLC mouse model. This mouse model is a practical in vivo approach to studying drug safety and testing whether targeted NP therapies reach their target in the presence of a functional immune system.

Keywords: cancer; cytochrome c; drug delivery; folate receptor; crosslinker; protein therapeutics

Author’s Biography

Irivette Dominguez-Martinez was born in Caguas, Puerto Rico, on May 2, 1993. In 2016, she graduated from the University of Puerto Rico, Cayey Campus, with a B.S. in Chemistry. She is a biochemistry Ph.D. candidate working with Dr. Griebenow in the Department of Chemistry at the University of Puerto Rico, Rio Piedras Campus (UPR-RP). Her doctoral research at Dr. Griebenow’s Applied Biochemistry and Biotechnology Laboratory focuses on developing and characterizing a cross-linked cytochrome c-based nanoparticle for tumor-targeted drug delivery. She received the PR-NASA Space Grant Fellowship and NIH-RISE Scholarship for this work. Irivette has recently collaborated in peer-reviewed published work in Cancers and Inorganics and presented her work in national and international meetings. She also worked as an undergraduate teaching assistant for the Chemistry Laboratory course at the UPR-RP and as a mentor and supervisor for undergraduate research in the (NIGMS/NIH)-Pre-MARC and NSF-REU programs. Currently, she is in her first year of a medical doctor (MD) at the Autonomous University of Guadalajara, Mexico. Irivette expected to contribute to patients' lives as a physician-scientist by providing scientific perspectives on issues of clinical aspects, medical intervention, and translational research.

Peer-Reviewed Publications

Dominguez-Martinez, I., Joaquin-Ovalle, F., Ferrer-Acosta, Y., & Griebenow, K. H. (2022). Folate-Decorated Cross-Linked Cytochrome c Nanoparticles for Active Targeting of Non-Small Cell Lung Carcinoma (NSCLC). *Pharmaceutics*, 14(3), 490.

Barcelo-Bovea, V., **Dominguez-Martinez, I.**, Joaquin-Ovalle, F., Amador, L. A., Castro-Rivera, E., MedinaÁlvarez, K., McGoron, A., Griebenow, K., Ferrer-Acosta, Y. (2020). Optimization and Characterization of Protein Nanoparticles for the Targeted and Smart Delivery of Cytochrome c to Non-Small Cell Lung Carcinoma. *Cancers*, 12(5), 1215.

Gaur, K., Vázquez-Salgado, A., Duran-Camacho, G., **Dominguez-Martinez, I.**, Benjamín-Rivera, J., FernándezVega, L., Carmona Sarabia, L., Cruz García, A.; Pérez-Deliz, F., Méndez Román, J.A., Vega-Cartagena, M. LozaRosas, S.A., Rodriguez Acevedo, X., Tinoco, A.D. (2018). Iron and Copper Intracellular Chelation as an Anticancer Drug Strategy. *Inorganics*, 6(4), 126.

Dedication

I dedicate my dissertation to God and my dear parents, Jose Domínguez and Ana Martínez, who has always supported me at every stage of this beautiful career. I also dedicate this work to the patients who fight cancer and the committed scientists who work hard to find alternatives to cure or improve the quality of the patient's life.

Acknowledgments

Many people have contributed to the successful completion of my Ph.D. degree. I wish to express my most sincere gratitude and appreciation to my PI and advisor, Dr. Kai Griebenow, a great scientist, scholar, educator, and mentor, for his direction, support, inspiration, and faith in me throughout the development of my Ph.D. I also want to give my deepest appreciation to my committee members, Dr. Arthur Tinoco, Dr. Yancy Ferrer, Dr. Nestor Carballeira, and Dr. Marvin Bayro, for their invaluable guidance and support as I transitioned from student to scientist.

I greatly appreciate Dr. Yancy Ferrer for her advice, dedication, and collaboration in this project. Moreover, I am very grateful for your trust in recommending me for medical school after finishing my Ph.D. research work. In addition, I am very thankful to Melisa Vega for their continued support in my research and for her friendship throughout the time of my research work. Also, I am immensely grateful to my friend Freisa Joaquin for her support and for sharing her knowledge and experience with me at the beginning of my research.

In addition, I want to give my most appreciation to the National Institute on Minority Health and Health Disparities (NIMHD) and the National Institute of Allergy and Infectious Diseases (NIAID) of the National Institutes of Health for the support of this work under the award number U54MD007587. Also, I acknowledge the National Aeronautics and Space Administration Cooperative Agreement no. 80NSSC20M0052 (Puerto Rico Space Grant Consortium).

Chapter 1

INTRODUCTION

1.1. Cancer statistics and treatments

Cancer is a heterogeneous group of diseases defined by the uncontrolled proliferation of abnormal cells. Malignant cells can invade the surrounding tissue and cause metastasis. According to the World Health Organization (WHO), cancer is a major public health problem worldwide and is the second leading cause of death globally. In 2021, 1,898,160 new cancer cases and 608,570 cancer deaths were projected to occur in the United States, the equivalent of 5,200 new cases each day [7]. In the United States, lung cancer has the highest incidence of mortality among all cancer types in both females and males (Figure 1.1.). From this projection for 2021, it was expected that 13% and 22% of new cases and deaths, respectively, will be caused by lung and bronchus cancer [7]. According to the statistics of the American Cancer Society, the probability (%) between 2013 to 2015 of developing invasive lung and bronchus cancer from birth to death was 6.7% (1 in 15) in males and 5.9% (1 in 17) in female. In contrast to the steady increase in survival for most cancers, advances have been slow for lung cancer, for which the 5-year relative survival rate is currently over 21% [7].

There are two main types of lung cancer: non-small cell lung cancer (NSCLC) and small cell lung cancer (SCLC). Lung cancer cells of both types grow and spread in different ways. NSCLC comprises about 85% of lung cancer diagnoses, while SCLC comprises approximately 15% [8]. NSCLC is a heterogeneous aggregate, including squamous cell carcinoma, adenocarcinoma, and large cell carcinoma [9]. Most patients

will have an advanced-stage non-operable disease at the time of diagnosis. In this disease setting, treatment aims to slow down the progression of the disease, relieve the patients from lung cancer symptoms, and, whenever possible, increase the overall survival (OS). Existing therapeutic strategies for lung cancer include surgery, radiation therapy, and chemotherapy, which can be used alone or in combination with other therapies [10]. Other treatment options include immunotherapy and targeted therapy. These therapeutic approaches have improved patient survival. However, systemic therapies still show poor treatment for most patients [11]. The choice of therapy depends upon the location, grade of the tumor, and the stage of the disease.

Chemotherapy is the application of chemicals or drugs to kill cancer cells, and its effects are systemic. Earlier therapeutic options have been limited because of high cytotoxicity toward the non-cancerous cell, leading to systemic toxicity and adverse effects. Approximately 40% of newly diagnosed lung cancer patients are stage IV. The goal of treating these patients is to improve survival and reduce disease-related adverse events. For stage IV NSCLC, cytotoxic combination chemotherapy is the first-line therapy, which might be influenced by histology, age, and performance status (PS) [12]. The American Society of Clinical Oncology states that treatment for a patient with a PS of 0 or 1 is a regimen of platinum (cisplatin or carboplatin) plus paclitaxel, gemcitabine, docetaxel, vinorelbine, irinotecan, or pemetrexed [13]. Reports from multicenter randomized clinical trials have shown that no single regimen demonstrated significant superiority over any other combination [14-16]. The median OS for patients in these studies was approximately 8–10 months [14-16]. The specific combination depends on the types and frequencies of toxic effects and should be decided individually. However,

adenocarcinoma patients may benefit from pemetrexed [17]. Cisplatin is the more effective platinum; however, it has been associated with more side effects. For patients with a PS of 2, evidence suggests that they may need only one drug, typically not platinum [18]. Chemotherapy treatment is usually well tolerated by patients with performance status (PS) 0 and 1 but is rarely effective in patients with a PS 3 and 4, where palliative care is preferred [19]. Despite its toxicity profile and short-term effectiveness, chemotherapy remains the first-line treatment for NSCLC.

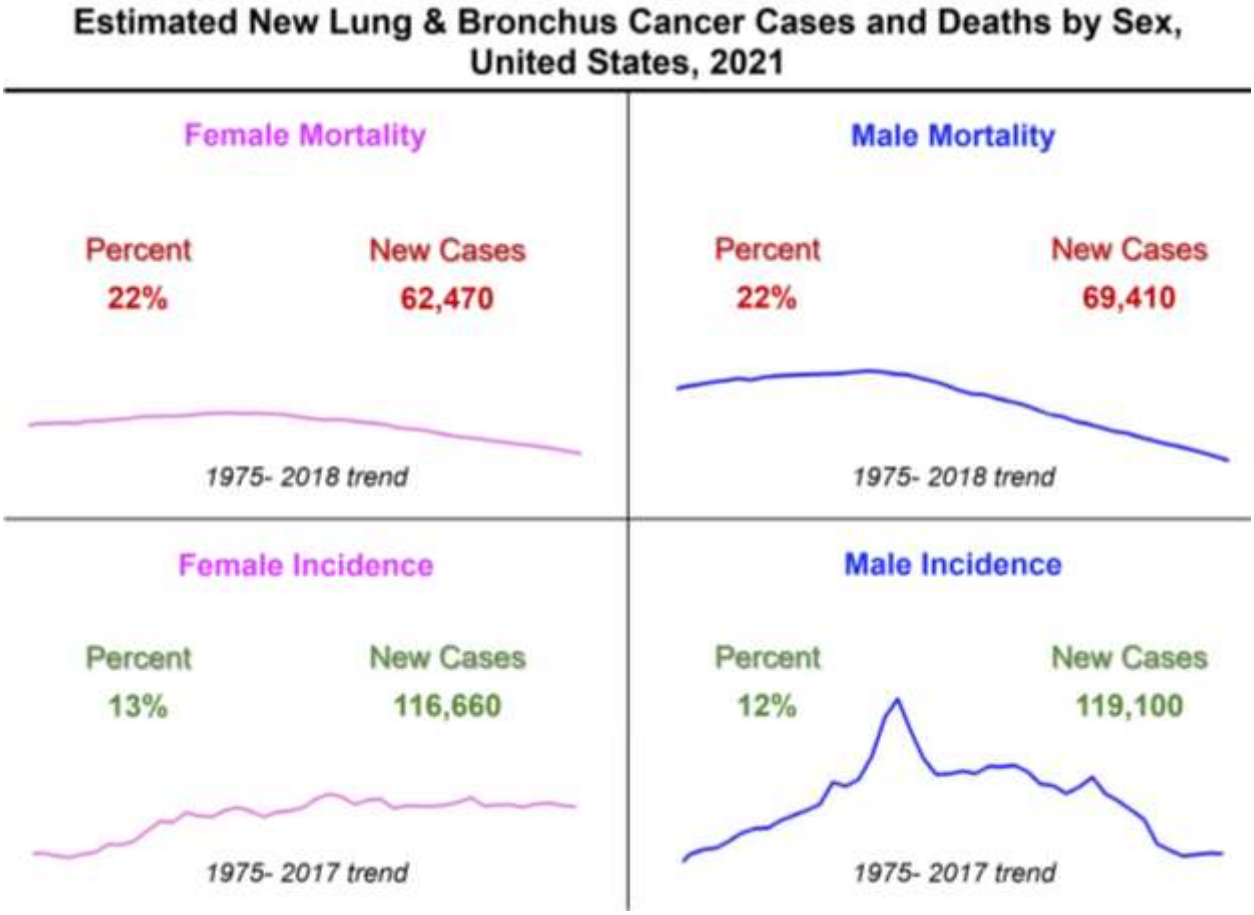

Figure 1.1. Estimated new lung and bronchus cancer cases deaths by sex in the United States, 2021. Long-term trends in lung and bronchus cancer incidence (1975-2017) and mortality (1975-2018) rate. Adapted from Ref [7].

1.2. Nanoparticles in cancer therapeutics

Rapid growth in nanotechnology toward developing nanomedicine agents holds massive promise to improve therapeutic approaches against cancer. Nanoparticles (NPs) are nanometer-sized (≤100 nm) colloidal particles, typically with a therapeutic agent encapsulated within the particle-matrix, adsorbed, or conjugated through functional modifications onto the surface, which results in improved drug stability and targeted efficacy. Nanocarriers change the pharmacokinetic properties of drugs to improve their efficiency and decrease their side effects [20]. Anticancer drugs in nano-formulations exhibit enhanced therapeutic index due to their ability to improve drug solubility, enable targeting of specific tissues, reduce systemic toxicity, and increase cellular uptake of encapsulated or attached drugs at the target site [21]. Due to their sub-micron size, NPs have deep tissue penetration, can cross epithelial fenestrations, and are generally taken up efficiently by target cells, improving the bioavailability of therapeutic moieties [22]. In contrast, conventional drugs are rapidly cleared from the body, reducing the amount of drug at the tumor site [23].

There are many advantages to using nanoparticles as a drug delivery system. First, NPs have the potential to enable the preferential delivery of drugs to tumors owing to the enhanced permeability and retention (EPR) effect and the delivery of more than one therapeutic agent for combination therapy [24]. The extent and rate of release of the drug can be optimized by manipulating the surface characteristics of the NP. Other advantages of NPs include specific binding of drugs to targets in cancer cells or the tumor microenvironment, simultaneous visualization of tumors using innovative imaging techniques, enhanced drug-circulation times, and superior dose scheduling for improved

patient compliance [25]. Since many tumor types are inherently resistant to available chemotherapeutics, a stable association between the drug and NP enhances the potential to overcome these problems [26].

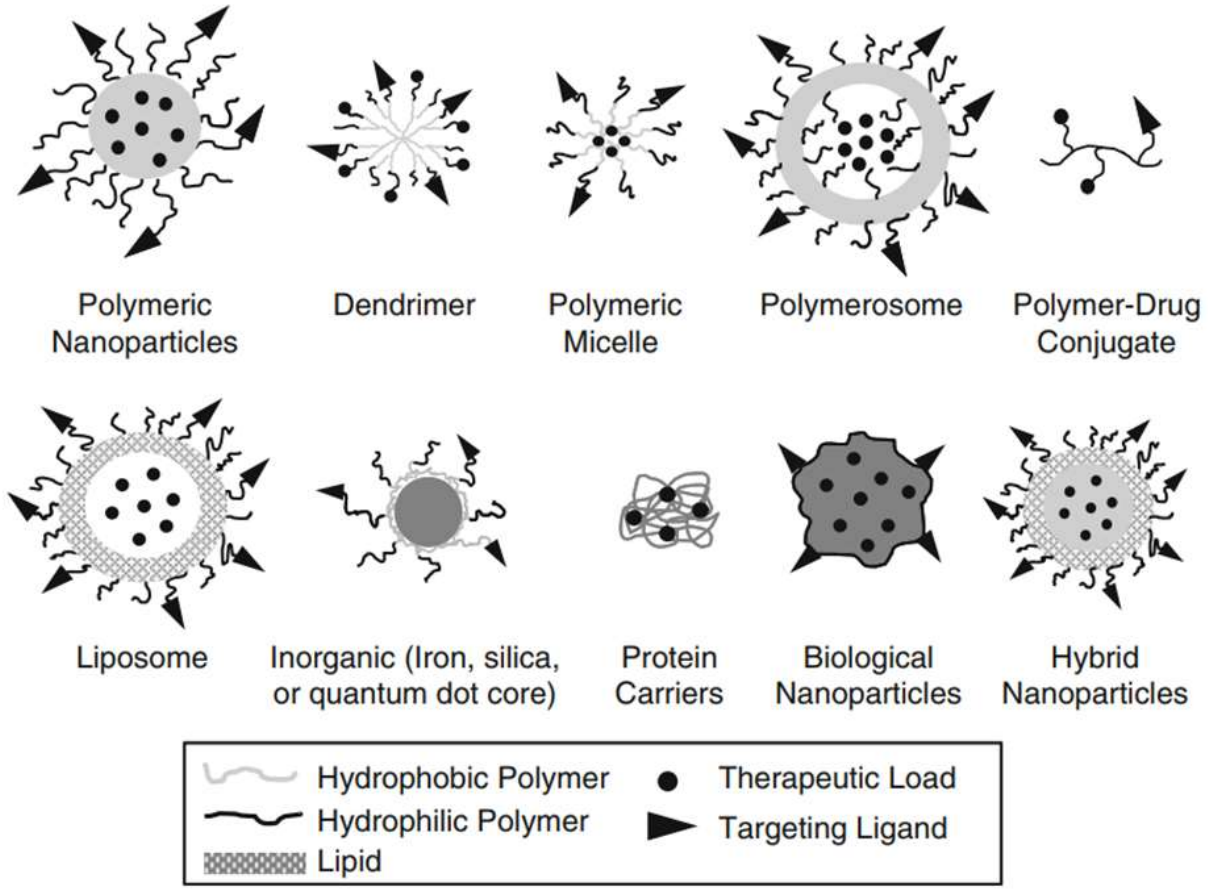

Figure 1.2. Nanoparticle platforms for drug delivery. Reproduced from ref [27].

Nanoparticle technologies for cancer therapy include polymeric NPs [28], dendrimers [29], micelles [30], polymersome [31], polymer conjugates [32], liposomes [33], inorganic NPs [34], protein carriers [35], biological NPs [36], and hybrid NPs [37] (Figure 1.2.). The diversity of delivery systems allows NPs to be developed with a diverse array of shapes, sizes, and components to be tailored for specific applications [38].

However, when designing any drug delivery system, the primary consideration is to achieve more effective therapies by controlling the drug concentration in the therapeutic window, reducing cytotoxic effects, and improving patient compliance. This allows effective treatment cycles to be maintained while reducing damage to healthy cells and minimizing recovery. Currently, there are FDA-approved drugs within some of these categories where nanotechnology seems to improve their therapeutic effects, overcoming their intrinsic conventional limits (Table 1.1.).

Table 1.1. Active and completed nanomedicine-based chemotherapeutics drug clinical trials [39].

Drug	Nano Delivery System	NSCLC Stage	Phase	Clinical Trial
Doxorubicin Hydrochloride (Adryamycin®, Rubex ®)	Pegylated Liposome	IIIB–IV	II	NCT01051362
	Aerosolized Liposome	IIIB	I	NCT00020124
	Liposome	IIIB–IV	IV	NCT02996214
Paclitaxel	Polymeric micelle (Genexol-PM®)	IV	II	NCT01023347 NCT01770795
Camptothecin	Aerosolized Liposome	IIIB–IV	Pre-clinical	NCT00277082
Lurtotecan	Liposome	IIIB	I	NCT00006036

1.3. Targeting of tumor microenvironment

Multidisciplinary research efforts in the field of drug delivery have led to the development of a variety of nanomaterials designed for the site-specific delivery of therapeutic anticancer agents. As the knowledge about cancer development progresses, it highlights the complexity of the disease characterized by inter-tumor and intra-tumor heterogeneity between cancer types [40]. These morphological changes can be exploited to design drug delivery systems (DDSs) that can be specifically targeted to these regions. Angiogenesis, defined as the formation of new blood vessels from existing ones, is an important characteristic that allows the tumors to thrive, providing them with an enriching supply of oxygen and nutrients [41]. The blood vessels then continue to proliferate rapidly, producing a severely irregular and aberrant vasculature, thus resulting in regions with high blood or poor blood supply compared with healthy vessels in normal organs. Tumor vessels can become excessively leaky due to deficient basement membranes and incomplete endothelial linings caused by the extremely compromised ability of endothelial cells to completely envelop the proliferating cells forming the vessel walls [42]. In response, this allows nanoparticles to accumulate inside the tumor fenestrae. This phenomenon is termed the Enhanced Permeation and Retention (EPR) effect (Figure 1.3.) [24].

The permeability of the compromised vasculature and retention can accumulate even macromolecules, increasing their tumor concentration by 70-fold [43]. The EPR effect alone increases the tumor specificity of NPs by 20-30% over critical normal organs [44]. Various important factors such as circulation time, targeting, and the capability to overcome barriers are heavily reliant on the shape, size, and surface area of these

particles [38]. To produce long-circulating NPs that can accumulate inside tumor tissues, a diameter between 30 nm and 200 nm is desired [25]. Using this approach, researchers may induce passive accumulation of nanomaterials inside a tumor by changing the diameter of a nanoparticle [45]. The capacity of smaller particles to navigate between the tumor interstitium after extravasation increased with decreasing size [38]. However, they must be bigger than 20 nm to avoid renal filtration during circulation [46]. By contrast, larger nanoparticles (≥400 nm) do not extravasate far beyond the blood vessel because they remain trapped in the extracellular matrix between cells [47]. For the in vivo application, it has been reported that spherical particles that are 100-200 nm in size have the highest potential for prolonged circulation because they are large enough to avoid uptake in the liver but small enough to prevent filtration to the spleen [48].

When administered into the blood, most nanomaterials are taken up within minutes or hours by the phagocytic cells of the mononuclear phagocyte system. This rapid clearance can be avoided by adding poly(ethylene) glycol (PEG) to the surface of DDS. Several studies showed the increased half-life of nanomaterials by simply adding PEG to their surface [49]. By preventing opsonization, the addition of PEG drastically increases the blood half-life of all nanomaterials regardless of surface charge [38]. Generally, the blood half-life of gold nanoparticles is also increased by increasing the length of PEG, which causes the protective layer to thicken [45]. The chemistry used to attach PEG, overall PEG length, and surface density affects the NP stability [45,50,51]. Alternative molecules such as lipids and silica were investigated, but PEG remains the most widely used approach [52].

Active targeting NPs also rely on the EPR effect to access the intra-tumoral space. Targeting moieties for molecular recognition (e.g., antibodies, peptides, and small molecules) are used to potentially increase total accumulation by anchoring the NPs onto the tumor cells. This targeting strategy allows specific retention and uptake of NPs by promoting ligand-receptor interactions at the surface of tumor cells, inducing receptor-mediated endocytosis and drug release inside the cell [53]. The high proliferation rate of tumor cells demands a higher nutritional supply resulting in the increased expression of nutrient receptors, such as folic acid receptors (FRs), to respond to the high request for folate or folic acid (FA) for DNA synthesis [54]. FA is a vitamin B, necessary for cellular proliferation, DNA synthesis, and modification [55]. The FRα is a well-known tumor marker overexpressed in 40% of human cancers [56]. Studies have found that levels of FRs expression are associated with tumor stage and survival, specifically in NSCLC [57,58]. In addition, there is a lower distribution of FRs in normal tissues compared to the expression of this receptor in several cancer types [59]. This overexpression in tumors promotes FA ligand-drug conjugates to binding and subsequent internalize via FR-mediated endocytosis [60]. Hence, combining the passive EPR-mediated targeting with an additional tumor-abundant ligand, such as FA, not only amplifies the specificity of therapeutic NPs but also facilitates their cellular uptake.

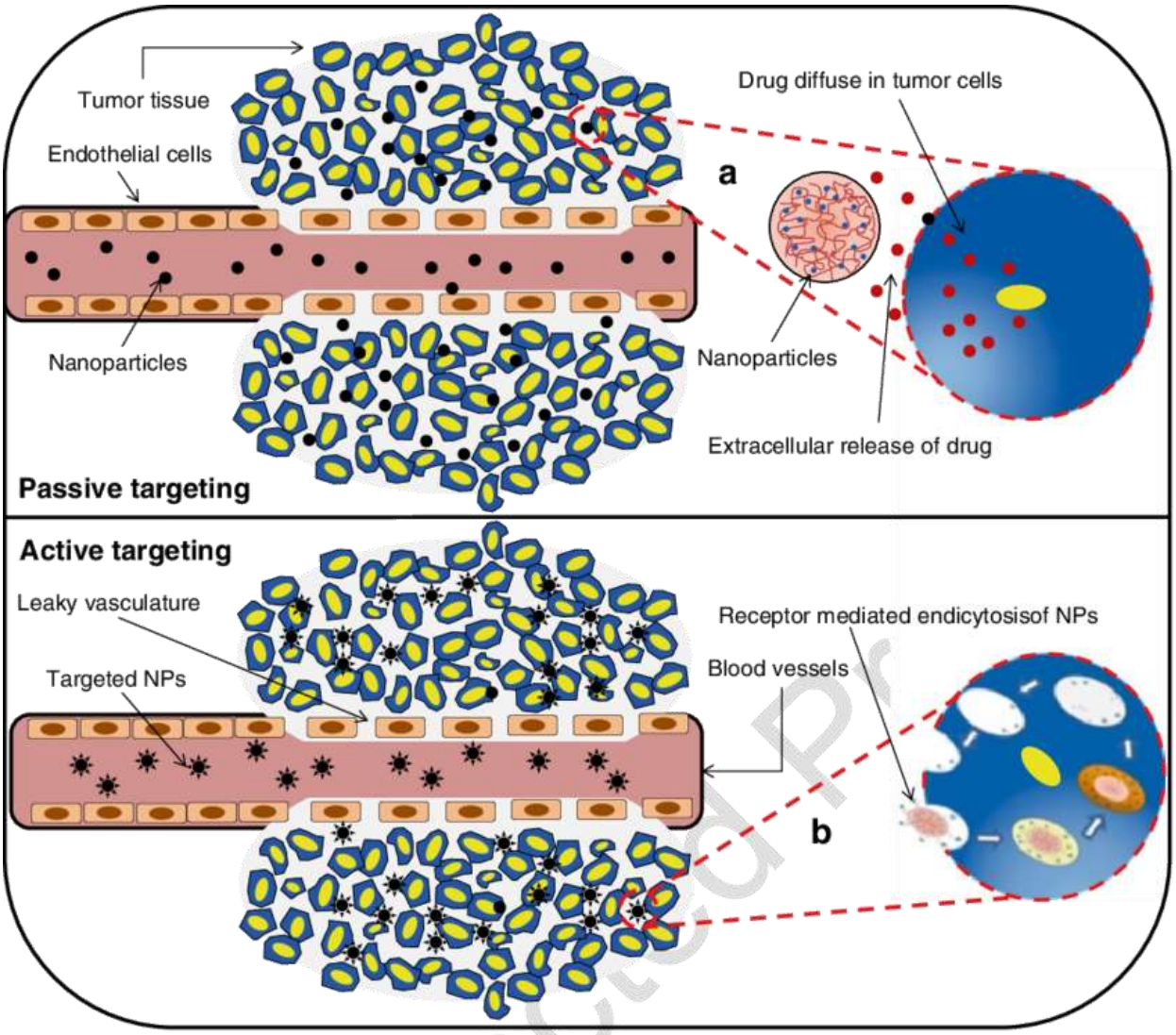

Figure 1.3. Passive targeting and active targeting strategies for anticancer drug delivery system. (*Top*) By the EPR effect, NPs passively diffuse through the leaky vasculature and accumulate in tumor tissues. In this case, drug may be released in the extracellular matrix and then diffuse through the tissue (a). (*Down*) In active targeting, once particles have extravasated in the tumor tissue, the presence of targeting ligands (e.g., FA) on the NP surface facilitates their interaction with receptors that are present on tumor cells, resulting in enhanced accumulation and preferential cellular uptake through receptor-mediated endocytosis (b). Reproduced from ref [61].

1.4. Stimulus-responsive delivery

Since efficient uptake of drug carriers into target cells is central to effective drug delivery, a comprehensive understanding of the intracellular chemical environment can facilitate the development of “smart” DDSs capable of preventing off-targets and enhancing therapeutic outcomes. In general, stimulus-responsive release systems allow the controlled release of drugs by responding to endogenous (e.g., pH, enzymes, and redox sensitivity) or exogenous (e.g., heat and light) activation [62]. Among different internal stimuli-responsive DDSs, redox-responsive nanoparticles have shown a significant potential for controlling drug release [63].

Redox-responsive NPs are considered efficient for “smart” transport and delivery of anticancer agents to target tumors [64]. Glutathione (GSH) is the most abundant and powerful reducing agent in mammalian cells because of its intrinsic thiol group and serves as an interesting internal stimulus for the delivery of anticancer drugs [65,66]. There is a marked difference in the redox potential between the intracellular and extracellular spaces. The intracellular concentration of GSH is about 2–10 mM, while the GSH concentration in extracellular fluid in tissue is only about 2–20 μM [67]. Consequently, the concentration of GSH in tumor tissues and the cytosol of tumor cells are at least 4 times higher than that in normal tissues, so tumors can be considered a reducing environment [68]. It has also been demonstrated that tumor tissues are significantly more hypoxic than normal healthy cells [69]. This ensures the usefulness of the glutathione disulfide-glutathione redox couple (GSSG/GSH) in developing redox-responsive nanocarriers [46].

Thiol-cleavable cross-linkers are used as a common synthetic method to form stable bonds under aerobic conditions, preventing the disintegration of the nanoparticle

in an aqueous environment but reducing it to a thiol group in highly reducing conditions [70]. In particular, the DSP (dithiobis(succinimidyl propionate)) cross-linker contains a disulfide bond that has been used to trigger the release of pro-apoptotic proteins in cancer cells, making it useful for redox-responsive delivery [71]. This homo-bifunctional N-hydroxysuccinimide (NHS) ester cross-linker has identical reactive groups at either end and reacts rapidly with any primary amine-containing molecule (Figure 1.4.) [72]. Since this type of cross-linker can be used in one-step reactions can save more time and material. Indeed, chemical cross-linking reagents can also affect different nanostructure features, including size and shape [71,73]. Several studies have reported that redox-sensitive cross-linkers reduce enzymatic degradation, raising circulation time in vivo and controlling drug release from the NPs [74]. Many nano vehicles with redox-responsive properties have been developed, but not many studies have investigated how redox-responsive cross-linking affects the colloidal and functional properties of the nanoparticles [75]. Finally, it is reported that when combined with passive and active targeting, stimulus-responsive strategies can potentially enhance the efficiency of anticancer action towards tumor tissues with good site-specific targeting and controlled release while lowering cancer multidrug resistance [64].

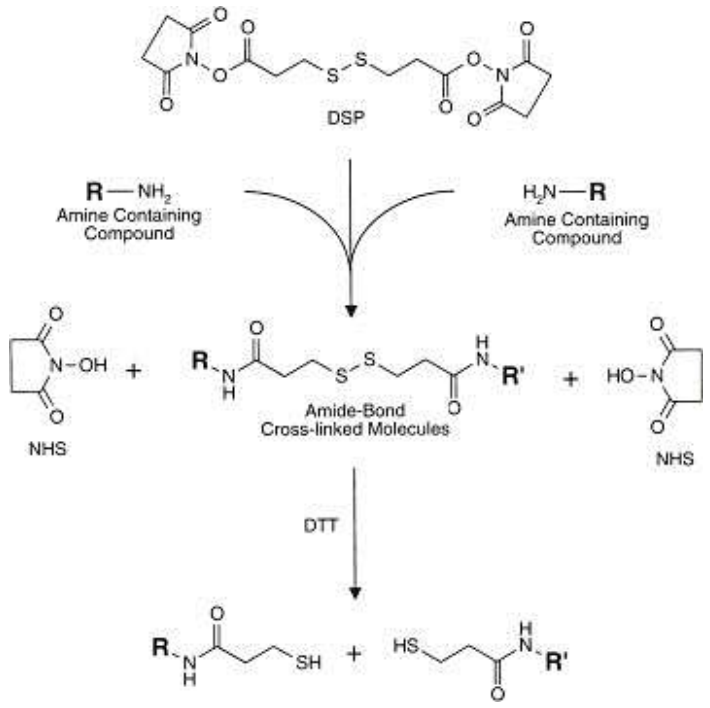

Figure 1.4. The reaction of DSP with amine-containing molecules yields amide bond crosslinks. The conjugates may be cleaved by reduction of the disulfide bond in the cross-bridge with GSH. Reproduced from ref [72].

1.5. Therapeutic proteins

Proteins are a class of natural molecules with unique functionalities and potential applications in biomedical and material sciences [76]. Since the approval of *insulin* (a *recombinant protein)* by the US Food and Drug Administration (FDA) in 1982, protein therapeutics have been extensively developed [77]. More than 200 therapeutic proteins are currently on the market and above 1000 are in clinical development [78]. Therapeutic protein drugs have a critical advantage over small-molecule drugs that are currently more dominant in the pharmaceutical market [79]. They perform highly specific and complex functions that are not easily mimicked by small molecules. Therapeutic proteins have

maintained their research and development spotlight over the past several decades to treat some high-incidence human diseases, including cancer, metabolic disorders, and autoimmune diseases. To date, FDA-approved therapeutic proteins have already played a significant role in cancer treatment (Table 1.2.) [79]. However, despite the success of early protein drugs, numerous challenges have reduced their efficacy in the clinical setting, such as limited therapeutic index, acquired resistance, inefficient delivery, and individual patient variation [80]. Thus, the persistent need to develop cancer therapeutics with improved safety and efficacy provides constant fuel to drive the optimization of protein biologics[2].

Table 1.2. Protein-based NPs for cancer treatment. Reproduced from ref [79].

Protein-based NP	Trade name	Function	Examples of clinical use
Bevacizumab [81]	Avastin®	Humanized mAb that binds all isoforms of VEGFA	Colorectal cancer, non-small-cell lung cancer
Cetuximab [82]	Erbitux®	Humanized mAb that binds EGFR	Colorectal cancer, head, and neck cancer
Panitumumab [83]	Vectibix®	Human mAb that binds EGFR	Metastatic colorectal cancer
Alemtuzumab [84]	Campath®	Humanized mAb directed against	B-cell chronic lymphocytic leukaemia in patients who have been treated with

		CD52 antigen on T and B cells	alkylating agents and who have failed fludabarine therapy
Rituximab [85]	Rituxan®	Chimeric (human/mouse) mAb that binds CD20, a transmembrane protein found on over 90% of B-cell non-Hodgkin's lymphomas (NHL); synergistic effect with some small-molecule chemotherapeutic agents has been demonstrated in lymphoma cell lines	Relapsed or refractory low-grade or follicular $CD20^+$ B-cell NHL, primary low-grade or follicular $CD20^+$ B-cell NHL in combination with CVP chemotherapy; diffuse large B-cell $CD20^+$ NHL in combination with CHOP or other anthracycline-based chemotherapy; rheumatoid arthritis in combination with methotrexate
Trastuzumab [86]	Herceptin®	Humanized mAb that binds HER2/Neu cell surface receptor and controls cancer cell growth	Breast cancer

Proteins are the engines of life that perform essential functions inside cells, such as enzyme catalysis, signal transduction, and gene regulation, and maintain a fine balance between cell survival and programmed death. Protein therapeutics are categorized into two types based on the active sites of proteins. One is the protein therapeutics with extracellular targets (i.e., take effect outside the cell), such as antibodies and protein antigens [87]. The other is protein therapeutics with intracellular targets (i.e., act in the cytosol), being the most reported caspase-3, ribonuclease A (RNase A), and cytochrome c (Cyt c) [88-91]. In this frame, pro-apoptotic proteins, such as Cyt c, are gaining importance as therapeutic candidates in cancer therapy [92].

Cytochrome c as an anticancer drug

All chemotherapeutic drugs, regardless of their specific target or mechanism of action, produce the same cytotoxic end effect in sensitive cells: cell death. Contrary to necrosis, apoptosis is when intracellular components are degraded to a less complex byproduct, which can undergo clearance by lymphocytes and macrophages with minimum adverse effects on the healthy adjacent tissue [93]. However, the apoptotic DNA damage response requires the involvement of the p53 tumor suppressor pathway, which is mutated/inactivated in ~50% of human cancers [94] and approximately 70% of lung adenocarcinoma cases [95]. The P53 pathway consists of activating pro-apoptotic Bcl-2 protein family members, such as Bax, which cause mitochondrial outer membrane permeabilization leading to the release of Cyt c into the cytoplasm [96]. Such oncogenic mutations that disrupt the apoptosis pathway contribute to tumor initiation, progression, and metastasis [95]. For example, Taxol®, a current first-line lung cancer treatment, causes damage leading to p53-tumor-suppressor-dependent apoptosis and often results

in the development of resistance, leading to therapy failure and relapse [97]. In addition, the dose-limiting toxicity of most anticancer drugs leads to a low therapeutic index and adverse toxic effects. Such limitations have spurred efforts to identify more effective chemotherapeutic agents that can be tolerable in higher doses and act independently of the p53 pathway [98].

As an alternative approach, proteins that exhibit potent cytotoxic activities can be exploited to develop new anti-tumor drugs [79]. Cyt c fulfills this requirement because it is non-toxic in the cytoplasm and acts downstream in the apoptosis cascade, thus evading many steps with potential mutations. This protein is a highly conserved (~12 kDa) and water-soluble, consisting of a 104 amino acid single peptide with a heme group [99]. Cyt c is primarily known for its function in the mitochondria as a key participant in the life-supporting function of ATP synthesis [100]. Specifically, Cyt c is a crucial mediator of apoptosis when released from the mitochondria and acts downstream of p53 in the apoptotic pathway activating the effector caspases, making the programmed cell death process irreversible [96]. During Cyt c-mediated apoptosis, the apoptosome formation (Apaf-1/Cyt c complex), which cleaves procaspase-9 to active caspase 9, is a critical event responsible for activating effector caspases 3 and 7, which mediate apoptosis (Figure 5) [101]. Indeed, delivering Cyt c from an external source into the cytoplasm of cancer cells could help overcome the apoptotic upstream blockage making it less prone to inactivation by mutations [44]. Hence, Cyt c has drawn the attention of some research groups for its potential to be developed into a highly effective and selective anticancer drug [44,90,102,103]. However, their therapeutic effectiveness is compromised by various biological barriers, including protease degradation and denaturation, hindered

delivery to the cytosol by crossing cell membranes, and escape from endosomes [104,105]. In addition, since Cyt c is a cell-membrane-impermeable protein, it must be linked to an uptake process. Thus, their potential as therapeutic proteins often requires modification, encapsulation, or immobilization with biocompatible matrices to improve their stability, activity, immunogenicity, and delivery [106].

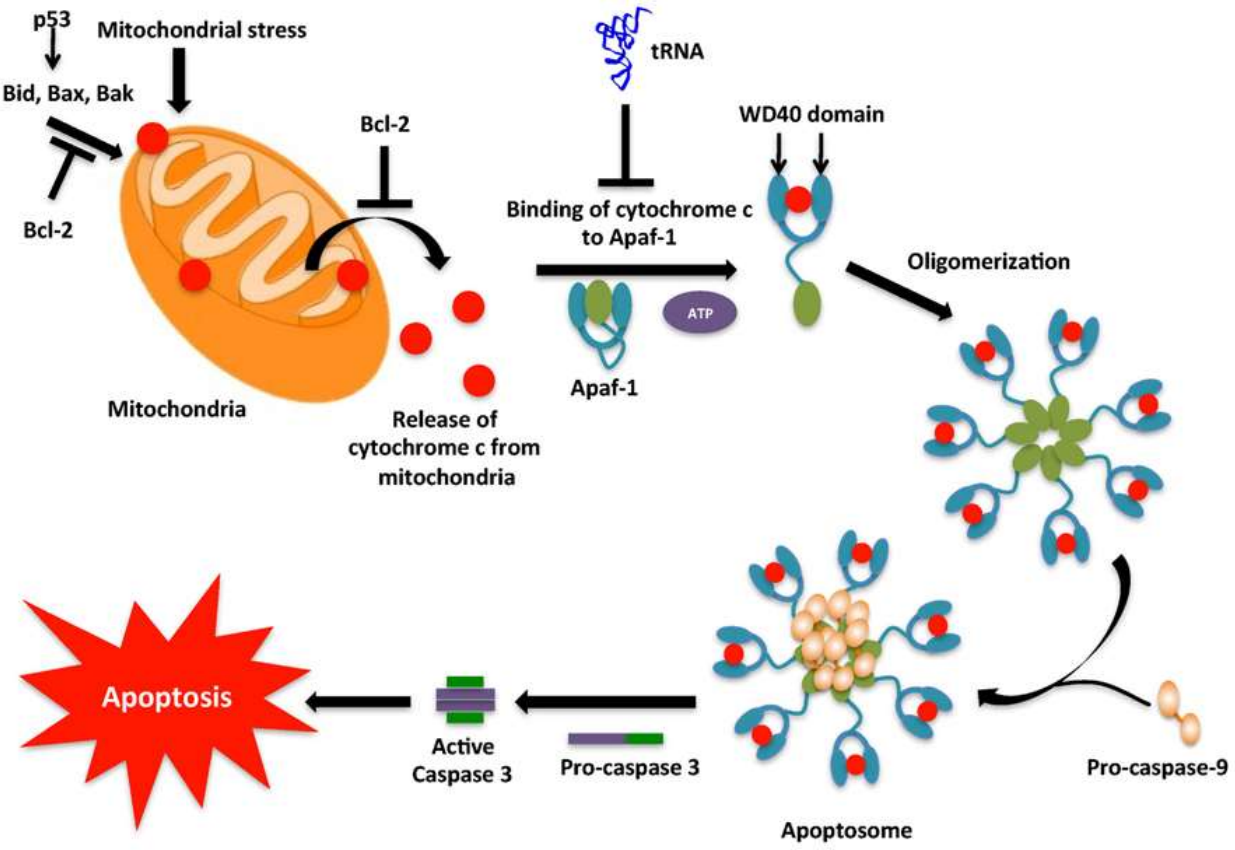

Figure 1.5. Intrinsic pathway for apoptosis. The intrinsic pathway, typically initiated by DNA damage, activates p53. p53 then activates the pro-apoptotic proteins, which cause mitochondrial outer membrane permeabilization, leading to Cyt c in the cytoplasm. Cyt c associates with Apaf-1 to form the apoptosome complex in the cytoplasm. The apoptosome causes the conversion of inactive pro-caspase-9 into active caspase-9.

Caspase-9 then activates caspase-3, leading to the caspase cascade, resulting in apoptosis. Reproduced from ref [101].

Cytochrome c delivery systems for cancer therapy

To facilitate intracellular Cyt c delivery, previous studies mainly focused on developing effective delivery vehicles. Kam et al. explored single-walled carbon nanotubes as intracellular Cyt c transporters through the nonspecific binding between protein and nanotube, and the proteins were found to be easily transported into various mammalian cells by the endocytosis pathway to enable the induction of cell apoptosis [107]. Similarly, mesoporous silica NPs [108], lipid-apolipoprotein NPs [103], and graphene oxide [109], have also been investigated as Cyt c nanocarriers to promote cellular internalization. However, most nanocarriers featured that Cyt c was loaded onto their surface so that it could activate the apoptotic pathways in both tumor and normal cells without specificity.

To mitigate such adverse effects to normal cells, responsive nanocarriers were utilized as an efficient intracellular transporter of Cyt c for cancer treatment [110]. Reduction-sensitive nanoplatforms, such as S−S bonds hybrid polymer [111], hyaluronic acid (also called hyaluronan, HA) nanogel [112], and Cyt c-transferrin conjugate [113], have been demonstrated to realize specific Cyt c delivery in tumor cells, due to the highly reductive environment of tumor cells over normal cells.

1.6. Protein-based nanoparticles preparation via nanoprecipitation method

Recently, protein-based NPs prepared by the nanoprecipitation method could be found in the literature [6]. Morales-Cruz et al. presented a novel targeted NP-based

delivery of Cyt c in which the nanoparticle core consisted of Cyt c itself [114]. For stabilization, the Cyt c NP was coated with the amphiphilic copolymer (FA-PEG-PLGA-SH) attached to Cyt c through a redox-sensitive bond via a hetero-bifunctional linker succinimidyl-3-(2-pyridyldithio) propionate. This system showed a diameter of 338 nm as determined by dynamic light scattering (DLS). The FA-PEG-PLGA-S-S-Cyt c NP were examined in C57BL/6 mice implanted with GL261 glioma tumor. Tumor tissue and healthy tissue examined one day after the termination of treatment revealed significant apoptosis only in the tumor area. To improve this design, Barcelo-Bovea et al. optimized the Cyt c NPs synthesis procedure to reduce the NPs diameter and enhance tumor entry when applied systemically [4]. The optimized Cyt c PLGA-PEG-FA NPs showed selective cytotoxicity towards non-small cell lung carcinoma cells overexpressing FR, including LLC and HeLa, but not towards normal cells. However, even though the NP reached places such as the brain, heart, lung, kidneys, and liver, the mice showed no sign of toxicity after injection. For instance, these results show that nanoprecipitation is a successful and promising approach for preparing Cyt c NPs using the natural, biodegradable, non-toxic pro-apoptotic protein as starting materials.

The nanoprecipitation method is based on reducing the quality of the solvent in which the main constituent of nanoparticles is dissolved. Such variation in solvent quality can be achieved by altering the pH, salt concentration, solubility conditions, or the addition of a non-solvent [115]. This work is based on the non-solvent precipitation method. In brief, protein is dissolved in an aqueous solvent while the organic phase (non-solvent) is used as a poor solvent for the protein with good water miscibility (Figure 1.6.) [6]. By mixing both phases, supersaturation of the protein occurs, followed by the

formation of protein nuclei. The free protein units will condense around the nuclei, creating protein nanoparticles. This technique is known to produce small-sized particles with uniform distribution.

The non-solvent nanoprecipitation process includes three steps: generation of supersaturation, nucleation, and growth. Each step is affected by one or more of the experimental parameters, and the physicochemical properties of nanoparticles are affected by the rate and the behavior of the formulation in each precipitation step [6]. Thus, the experimental parameters could affect the physicochemical properties of nanoparticles [116].

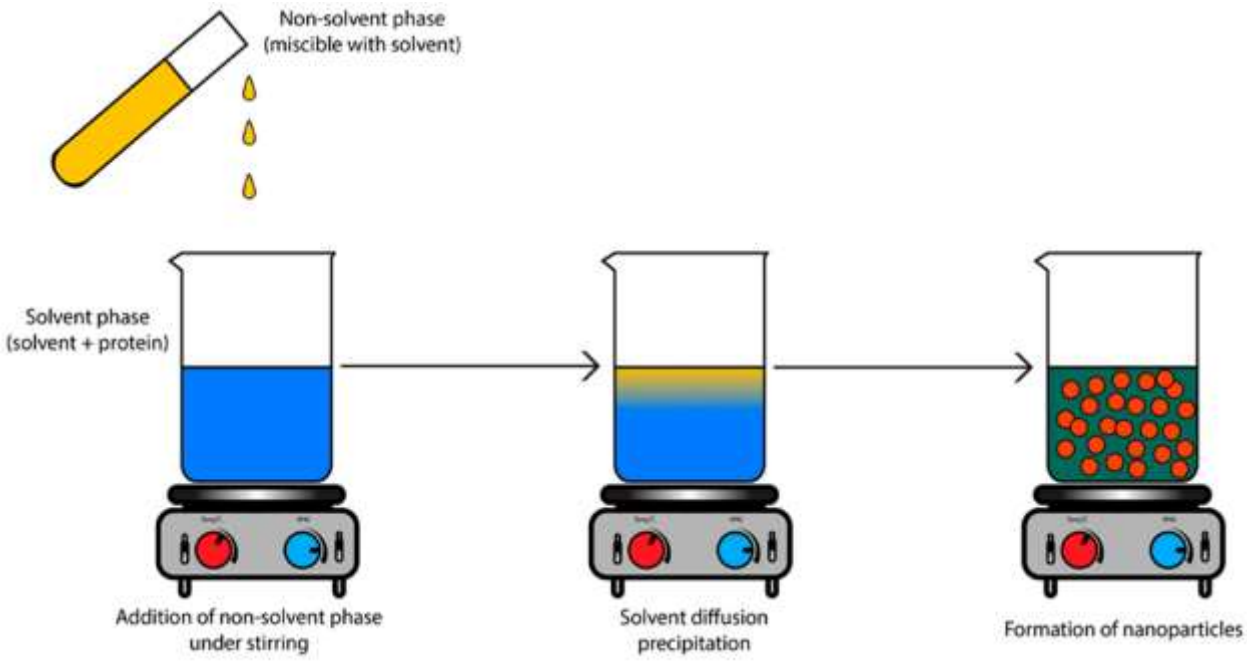

Figure 1.6. Protein-based nanoparticles prepared by nanoprecipitation method leading to submicron particles. The addition of the non-solvent phase leads to a state of supersaturation which allows the beginning of the nanoprecipitation process and the formation of nanoparticles. Reproduced from ref [6].

1.8. Research Aims

The following specific aims were designed to simplify and optimize the nanoprecipitation method for the preparation of cross-linked Cyt c-based NPs and exploit their therapeutic potential as a smart delivery system for folate-receptor targeted cancer therapy:

1.10.1. Specific Aim 1. To develop a simple and straightforward cross-linking approach using the non-solvent nanoprecipitation method to prepare redox-sensitive Cyt c-based NPs and evaluate the impact of the operating parameters on the particle size and the delivery properties.

It is reported that the capacity of small particles to navigate between the tumor interstitium after extravasation increased with decreasing size. For the in vivo application, it has been reported that spherical particles that are 100-200 nm in size have the highest potential for prolonged circulation because they are large enough to avoid uptake in the liver but small enough to prevent filtration to the spleen [48]. Protein nanoprecipitation is an easy and reproducible technique to prepare Cyt c NPs [117]. Their size, shape, and surface charge can be controlled to incorporate passive, active, and stimuli-responsive targeting. Therefore, this first aim is to optimize the protein nanoprecipitation method as a faster and more straightforward approach composed of a one-step. The simplified procedure involves non-solvent nanoprecipitation in the presence of the homo-bifunctional cross-linker DSP, which contains a thiol-cleavable bond. Optimization of the processing parameters involved in the new one-step cross-linking/nanoprecipitation method was evaluated. The NPs were characterized by dynamic light scattering (DLS), scanning electron microscopy (SEM), zeta potential (ZP), and encapsulation efficiency

(EE). We hypothesized that the increase in cross-linker concentration would increase size distribution due to more aggregation between NPs. In addition, we expected that the NP diameter decrease with an increase in injection rate, as reported in other studies. Moreover, a comparison of one-step vs. two-step cross-linking methods should demonstrate that the one-step method results in the smallest particle size because having more protein cross-linked in the core of the NP.

1.10.2. Specific Aim 2. To synthesize and characterize cross-linked Cyt c-based NPs that combine redox-responsive release and active targeting capabilities via the folate receptor for non-small cell lung cancer therapy (NSCLC).

Although the current first-line anticancer agents against NSCLC have been successful to some extent, their lack of tumor selectivity and systemic toxicity without discriminating healthy tissues produce unwanted and often severe and dangerous side effects. In this context, the folate receptor alpha (FR), which is overexpressed in 40% of solid tumors, including NSCLC, can be utilized for active tumor targeting to afford more effective cancer therapies. Recently, our research group overcame biocompatibility, and off-target limitations commonly seen in anticancer therapeutics by designing a Cyt c-based DDS coated with a biodegradable copolymer, poly(lactic-co-glycolic acid)-poly (ethylene glycol)-folate (PLGA-PEG-FA), which is 253 nm in size [4]. This DDS demonstrated a tumor-targeting capability and specific in vitro cytotoxicity towards cancer cells overexpressing folate receptors. However, the reported Cyt c-PLGA-PEG-FA NPs showed no cytotoxicity after an in vivo injection using a lung carcinoma immune-competent mouse model [4]. Herein we substantially simplify the system by employing another strategy for preventing protein dissolution in buffer and blood, which uses redox-

sensitive cross-linking. Applying the nanoprecipitation method with the best release profile proven in Specific Aim #1, we prepared Cyt c NPs using the two-step cross-linking approach. For this strategy, aqueous Cyt c was first precipitated with acetonitrile to form Cyt c NPs. Then, the synthesized Cyt c NPs was stabilized with the cross-linker dissolved in the non-solvent phase (acetonitrile). Finally, the NP surface was decorated with a hydrophilic folic acid–polyethylene glycol (FA-PEG) polymer for active targeting. The diameter, morphology, and surface charge of the NPs were studied using DLS, SEM, and zeta potential. The efficiency of the system was tested in vitro, using the Lewis lung carcinoma (LLC) cell line, and in vivo, using the LLC mouse model. It was hypothesized that Cyt c-PEG-FA NPs are more efficient as cytotoxic agents against cancer cells than Cyt c-PLGA-PEG-FA because of their higher payload and better redox-responsive release properties. Moreover, the reduction in diameter of Cyt c-PEG-FA NPs should be favorable for tumor accumulation and uptake in vivo using a syngeneic (immune-competent) LLC mouse model.

Chapter 2

Materials and method

2.1. Experimental procedures- Chapter 3

2.1.1. Materials

Cyt c from the equine heart (≥95% purity), acetonitrile, dithiobis(succinimidyl propionate) (DSP), and L-glutathione (reduced, ≥98.0% purity) were purchased from Sigma-Aldrich (St. Louis, MO). Ampilite^{TM} Colorimetric Caspase 3/7 Assay Kit was purchased from AAT Bioquest (Sunnyvale, CA).

2.1.2. Preparation of cross-linked Cyt c-DSP nanoparticles

2.1.2.1. One-step nanoprecipitation

Cross-linked Cyt c-DSP NPs were synthesized by the nanoprecipitation method [117] in the presence of the homo-bifunctional cross-linker. Briefly, 5 mg/mL of Cyt c dissolved in ultrapure water was solvent-precipitated with DSP dissolved in acetonitrile at a 1:4 (water/acetonitrile) volume ratio using an automated syringe pump. To study the effect of cross-linking concentration, different concentrations (0.2, 0.3, 0.5, 1.0, 1.5 mg/ml) of DSP were used at a constant rate of 125 ml/h. To study the effect on the nanoprecipitation rate, the automated syringe pump was adjusted at different rates (125, 200, and 300 ml/h), and the cross-linker was fixed to 0.5 mg/ml concentration. Then, the NPs suspension was left to react for 30 min at room temperature (RT). The NPs were subsequently centrifugated at 10000 rpm and washed thrice with ultrapure water. Then they were flash-frozen and freeze-dried.

2.1.2.2. Two-step nanoprecipitation

Cross-linked Cyt c-DSP NPs were synthesized by first obtaining protein NPs using a nanoprecipitation method and then stabilized with the homo-bifunctional cross-linker. Briefly, 5 mg/mL of Cyt c dissolved in ultrapure water was solvent-precipitated by adding acetonitrile at a 1:4 (water/acetonitrile) volume ratio at a constant rate of 125 ml/h using an automated syringe pump. The NPs suspension was left stirring for 5 min. Subsequently, the resulting Cyt c NPs suspension was covalently stabilized by directly adding 0.5 mg/ml of DSP cross-linker dissolved in acetonitrile to the resulting suspension and was allowed to react at RT for 30 min. The NPs were subsequently centrifugated at 10000 rpm and washed thrice with ultrapure water. Then they were flash-frozen and freeze-dried.

2.1.3. Determination of precipitation efficiency and actual protein loading

To calculate precipitation efficiency, an aliquot of 10 µl was collected right before nanoprecipitation to determine the initial amount of Cyt c. After nanoprecipitation, the NP suspension was centrifuged for 10 min at 10000 rpm at room temperature. The concentration of Cyt c in the aliquot and supernatants were determined by measuring the absorbance at 410 nm using a NanoDrop 2000c (Thermo Scientific, USA) [118]. Precipitation efficiency (EE) was calculated using the following equation:

$$EE\ (\%) = \frac{\text{initial amount of Cyt c} - \text{Cyt c in supernatant}}{\text{initial amount of Cyt c}} x100, \qquad (1)$$

The experiments were performed in triplicate, the results averaged, and the standard deviations calculated (SD).

2.1.4. Particle size, size distribution, and zeta potential measurements

Particle size, polydispersity index (PdI), and zeta potential of cross-linked Cyt c-DSP NPs were determined by dynamic light scattering (DLS) using a Zetasizer Nano ZS (Malvern Panalytical Ltd, Malvern, UK). The samples were dispersed in ultrapure water and subjected to ultrasonication at 240 W for 30 s before the measurements. NPs were transferred to capillary cells for zeta potential determination. The experiments were performed in triplicate, and the results were expressed as the mean ± SD.

2.1.5. Scanning electron microscopy

SEM micrographs of cross-linked Cyt c-DSP NPs were performed using a JEOL 6480LV scanning electron microscope at 20 kV. Lyophilized NPs were coated with gold for 10 seconds using an auto sputter coater (108 Auto/SE, Ted Paella Inc., USA).

2.1.6. In vitro release profile

For the determination of the *in vitro* Cyt c release profile, 0.5 mg/ml of cross-linked Cyt c-DSP NPs was suspended in PBS buffer (pH 7.4) with 10 mM of glutathione (GSH) simulating intracellular conditions [119]. The NPs were incubated at 37°C under constant stirring for various time intervals: 6, 12, 24, 48, and 72 h. At predetermined time points, NPs were centrifuged at 14000 rpm for 10 min, the supernatant was collected, and it was replaced with an equal volume of PBS-GSH buffer. The supernatant was used to determine the concentration of released Cyt c by UV-vis spectroscopy using a NanoDrop 2000c (Thermo Scientific, USA). The amount of released Cyt c was used to construct

cumulative release profiles. The experiments were performed in triplicate, the results averaged, and the standard deviations calculated.

2.1.7. Cell-free caspase 3/7 activity assay

Caspase activation by Cyt c was measured in Lewis Lung Carcinoma (LLC) cell ysate following the procedure previously reported in the literature [4]. Briefly, $5x10^6$ LLC cells were resuspended in 100 µl of lysis buffer, and cells were lysed with four freeze-thaw cycles using liquid nitrogen and a water bath at 37°C. Then, the cell lysate was centrifuged at 11,000 rpm for 20 min at 4°C, and the supernatant (lysate) was collected. For the caspase 3/7 cell-free reaction, the obtained lysate was mixed with 300 µg/ml of the cross-linked Cyt c NPs prepared by both nanoprecipitation methods using a volume ratio of 1:1 (lysate:NPs). The reaction was incubated at 37°C for 150 min. We used native Cyt c and untreated cells (lysate only) as a control experiment under the same conditions. Afterward, the Caspase 3/7 assay was performed following the manufacturer's protocol (Ampilite™ Colorimetric Caspase 3/7 Assay; AAT Bioquest, Sunnyvale, CA). In a 96 well plate, 100 µl of the active lysate was mixed with 100 µl of the Caspase 3/7 working reagent. Then, the plate was incubated at room temperature for 1 hour, and the absorbance was measured at 490 nm using a Synergy H1 (BioTek, Winooski, VT, USA). The mean ± SD of the cell-free caspase 3/7 activity was obtained from two independent experiments performed in triplicate. The results were analyzed statistically using the unpaired Student's t-test by GraphPad Prism (*** $p = 0.0007$, $n = 3$).

2.1.8. Statistical Analysis

Results are expressed as mean ± standard deviation (SD). Statistical probability was calculated using GraphPad software. Paired and unpaired *t*-tests or one-way ANOVA with Tukey's multiple comparison analysis were used to determine significance between groups. P values less than 0.05 were considered significant.

2.2. Experimental procedures- Chapter 4

2.2.1. Materials

Cyt c from the equine heart (≥95% purity), acetonitrile, dithiobis(succinimidyl propionate) (DSP), L-glutathione (reduced, ≥98.0% purity), and isomer I of fluorescein isothiocyanate (FITC) were purchased from Sigma-Aldrich (St. Louis, MO). Folate-poly(ethylene glycol)-succinimidyl ester (FA-PEG-NHS, M_W 3,400 Da) was purchased from Biochempeg Scientific Inc. (Watertown, MA). CellTiter 96 aqueous non-radioactive cell proliferation assay was purchased from Promega Corporation (Madison, WI). Ampilite™ Colorimetric Caspase 3/7 Assay Kit was purchased from AAT Bioquest (Sunnyvale, CA). DAPI (4,6-diamidino-2-phenylindole, NucBlue®), FM-464 membrane stain, propidium iodide (PI), and CellEvent™ Caspase-3/7 Green was obtained from Invitrogen (Eugene, OR). Near-infrared reactive dye IRDye® 680RD was available as a protein labeling kit (high molecular weight) from LI-COR Biosciences.

2.2.2. Synthesis of cross-linked Cyt c-PEG-FA nanoparticles

Cross-linked Cyt c-PEG-FA NPs were synthesized by first obtaining protein NPs using a nanoprecipitation method [4]. Briefly, 5 mg/mL of Cyt c dissolved in ultrapure water was solvent-precipitated by adding acetonitrile at a 1:4 (water/acetonitrile) volume ratio at a constant rate of 300 ml/h using an automated syringe pump. The NPs suspension was left stirring for 5 min. Subsequently, the resulting Cyt c NPs suspension was covalently stabilized by directly adding 0.2 mg/ml of the homo-bifunctional DSP cross-linker dissolved in acetonitrile to the resulting suspension. After 30 min under constant stirring at room temperature, 7 mg/ml of FA-PEG-NHS (MW 3,400 Da) polymer dissolved in a mixture of 3:1 acetonitrile/ultrapure water was added to the NPs suspension and was allowed to react at room temperature for 18 h. The NPs were subsequently centrifugated at 10000 rpm and washed thrice with ultrapure water. Then they were flash-frozen and freeze-dried.

2.2.3. Determination of precipitation efficiency and actual protein loading

To calculate precipitation efficiency and actual drug loading, an aliquot of 10 µl was collected right before nanoprecipitation to determine the initial amount of Cyt c. After nanoprecipitation, the NP suspension was centrifuged for 10 min at 10000 rpm at room temperature. The concentration of Cyt c in the aliquot and supernatants were determined by measuring the absorbance at 410 nm using a NanoDrop 2000c (Thermo Scientific, USA)[118]. The final amount of NP was obtained by weighing the final product.

Precipitation efficiency (EE) and actual protein loading (AL) were calculated using the following equations:

$$EE\ (\%) = \frac{\text{initial amount of Cyt c} - \text{Cyt c in supernatant}}{\text{initial amount of Cyt c}} x100, \quad (2)$$

$$AL\ (\%) = \frac{\text{mg of Cyt c in nanoparticles}}{\text{mg of nanoparticles}} x100, \quad (3)$$

The experiments were performed in triplicate, the results averaged, and the standard deviations calculated (SD).

2.1.4. Particle size, size distribution, and zeta potential measurements

Particle size, polydispersity index (PdI), and zeta potential of Cyt c- DSP NPs and cross-linked Cyt c-PEG-FA NPs were determined by DLS using a Zetasizer Nano ZS (Malvern Panalytical Ltd, Malvern, UK). The samples were dispersed in ultrapure water and subjected to ultrasonication at 240 W for 30 s before the measurements. NPs were transferred to capillary cells for zeta potential determination. The experiments were performed in triplicate, and the results were expressed as the mean ± SD.

2.2.5. Scanning electron microscopy (SEM)

SEM micrographs of cross-linked Cyt c-PEG-FA NPs were performed using a JEOL 6480LV scanning electron microscope at 20 kV. Lyophilized NPs were coated with gold for 10 seconds using an auto sputter coater (108 Auto/SE, Ted Paella Inc., USA).

2.2.6. In vitro release

For the determination of the *in vitro* Cyt c release profile, 0.5 mg/ml of cross-linked Cyt c-PEG-FA NPs was suspended in PBS buffer (pH 7.4) with glutathione (GSH) concentrations of 0, 0.001, and 10 mM simulating extra- and intracellular conditions [119]. The NPs were incubated at 37°C under constant stirring for various time intervals: 0.5 h, 2.5 h, 20 h, 30 h, and 46 h. At predetermined time points, NPs were centrifuged at 14000 rpm for 10 min, the supernatant was collected, and it was replaced with an equal volume of PBS-GSH buffer. The supernatant was used to determine the concentration of released Cyt c by UV-vis spectroscopy using a NanoDrop 2000c (Thermo Scientific, USA). Because FA can absorb at 410 nm, the wavelength used to measure the concentration of non-reduced Cyt c (0 mM and 0.001 mM GSH) was 530 nm, and reduced Cyt c (10 mM GSH) was 550 nm [4]. The amount of released Cyt c was used to construct cumulative release profiles. The experiments were performed in triplicate, the results averaged, and the standard deviations calculated.

2.2.7. Cell-free caspase 3/7 activity assay

Caspase activation by Cyt c was measured in Lewis Lung Carcinoma (LLC) cell lysate following the procedure previously reported in the literature [4]. Briefly, 5x106 LLC cells were resuspended in 100 µl of lysis buffer, and cells were lysed with four freeze-thaw cycles using liquid nitrogen and a water bath at 37°C. Then, the cell lysate was centrifuged at 11,000 rpm for 20 min at 4°C, and the supernatant (lysate) was collected. For the caspase 3/7 cell-free reaction, the obtained lysate was mixed with 300 µg/ml of

cross-linked Cyt c-PEG-FA NPs using a volume ratio of 1:1 (lysate:NPs). The reaction was incubated at 37°C for 150 min. We used native Cyt c and untreated cells (lysate only) as a control experiment under the same conditions. Afterward, the Caspase 3/7 assay was performed following the manufacturer's protocol (Ampilite^{TM} Colorimetric Caspase 3/7 Assay; AAT Bioquest, Sunnyvale, CA). In a 96 well plate, 100 µl of the active lysate was mixed with 100 µl of the Caspase 3/7 working reagent. Then, the plate was incubated at room temperature for 1 hour, and the absorbance was measured at 490 nm using a Synergy H1 (BioTek, Winooski, VT, USA). The mean ± SD of the cell-free caspase 3/7 activity was obtained from two independent experiments performed in triplicate. The results were analyzed statistically using the unpaired Student's t-test by GraphPad Prism 9.1.1 (****p <0.0001, n=6).

2.2.8. Cell viability assay

MTS cell viability assay (CellTiter 96 aqueous non-radioctive assay) from Promega (Madison, WI, USA) was used to measure the half-maximal inhibitory concentration (IC_{50}) value for the cross-linked Cyt c-PEG-FA NPs in LLC cancer cells. Lewis Lung Carcinoma (LLC) cells (10000 cells/well) were seeded in a 96-well plate and incubated with serial dilutions (300, 200, 100, 50, 25, and 12.5 µg/ml) of cross-linked Cyt c-PEG-FA NPs for 24 h at 37˚C. Controls, such as 300 µg/ml native Cyt c, FA-PEG-NHS, and folate-free Cyt c-DSP NPs, were also tested. As a control experiment, FR-negative mouse embryonic fibroblasts (NIH/3T3) cells and FR-positive human cervical carcinoma (HeLa) cells (10000 cells/well) were also incubated with 300 µg/ml of cross-linked Cyt c-PEG-FA NPs for 24 h. MTS assay was performed following instructions from the kit manufacturer, and the

absorbance was measured at 490 nm using a microplate reader (Tecan Infinite 200Pro, Meilen, Zurich). The IC_{50} value was calculated using GraphPad Prism from the dose-response curve; X=Log(X) against the normalized Y (values being 0% the smallest value in the data set and 100% the highest value data set). The normalized percent in cell viability was plotted against the following log concentrations of cross-linked Cyt c-PEG-FA NPs after 24 h: 1.097 µM, 1.398 µM, 1.699 µM, 2.00 µM, 2.301 µM, and 2.477 µM. Results were expressed as mean values of independent experiments performed in triplicate (n= 9) ± SD. To test the ability of folate to help reduce cancer cell viability, we compared folate-targeted Cyt c NPs and folate-free Cyt c NPs MTS results using an unpaired Student's t-test analysis (GraphPad Prism 9.1.1). A difference between folate-targeted Cyt c NPs and folate-free Cyt c NPs at 300 µg/ml was found, resulting in a statistically significant difference with a ****p-value of <0.0001.

2.2.9. In vitro cellular internalization and endosomal escape by confocal laser scanning microscopy (CLSM)

The cellular internalization and the ability to escape endosomal entrapment of the cross-linked Cyt c-PEG-FA NPs was observed by confocal laser scanning microscopy (CLSM). LLC and NIH/3T3 cells (10,000 cell/well) were seeded in chambered cover glass plates (4-wells). For these experiments, cross-linked Cyt c-PEG-FA NPs were modified with fluorescein isothiocyanate (FITC) via the amine group. Briefly, 25 µl FITC (1 mg/ml) was added to 1 ml of sample (3 mg/ml) dissolved in PBS (pH 7.4) buffer. The reaction was stirred overnight in the dark at 4°C, and then FITC-labeled NPs were lyophilized. Cell lines were incubated at 37 °C for 24 h with both: FITC-labeled NPs (100 µg/ml) and an

endosome marker (FM-464; 10 μg/ml). Afterwards, the medium was removed, and the cells were washed with PBS three times followed by fixation with 3.7% formaldehyde. DAPI was added to each well after fixation followed by three PBS washing cycles. We used glycerol to avoid photobleaching. Untreated cells were used as control. For cellular internalization and endosomal escape analysis, the chambered cover glass plates were examined under a Nikon Eclipse Ti-E inverted confocal scanning microscope (Nikon Instruments Inc., Melville, NY) using a 40x oil immersion objective and excitation at 488 nm. Quantification of the FITC fluorescence intensity of NPs in the red-stained cell membrane area was determined using the NIS-Element AR analysis program. The difference between the intensities of NPs treated cells and untreated cells ($p<0.05$) was used to subtract the green background autofluorescence. Unpaired T-test analysis by GraphPad Prism was used to compare independent data groups.

2.2.10. Study of cell death induction by CLSM

LLC cells and NIH/3T3 cells (10,000 cells/well) were seeded in a 4-well chambered cover glass plates. The cells were treated with 100 μg/ml of cross-liked Cyt c-PEG-FA NPs at 37 °C for 24 h. To detect apoptosis-dependent nuclear fragmentation, the cells were washed with PBS (1×) and incubated with PI (75 μM) for 5 min. Cells were fixed with 3.7% formaldehyde and then incubated with DAPI (2 drops), followed by three cycles of PBS washing. To avoid photobleaching of the fluorescent dyes, we added glycerol to each well. The chambered cover glass plates were examined under a Nikon Eclipse Ti-E inverted confocal scanning microscope (Nikon Instruments Inc., Melville, NY) using a 40x oil immersion objective. Untreated cells were subjected to DAPI/PI incubation as well to be used as control.

2.2.11. Study of the apoptotic induction mechanism by caspase 3/7 green detection

LLC cells (10,000 cells/well) were seeded in a 4-well chambered cover glass plates. The cells were incubated at 37 °C for 24 h with 100 µg/ml of cross-liked Cyt c-PEG-FA NPs. The activity of caspase 3/7 was determined with the CellEvent™ caspase 3/7 green reagent (Invitrogen) according to the manufacturer's instructions. The chambered cover lass plates were examined under a Nikon Eclipse Ti-E inverted confocal scanning microscope (Nikon Instruments Inc., Melville, NY) using a 40x oil immersion objective. Untreated cells were subjected to DAPI/CellEvent™ incubation as well and used as control. The mean green intensity of the confocal images was measured using the NIS-Element AR analysis program. Unpaired T-test analysis by GraphPad Prism between NPs treated cells and untreated cells was considered statistically significant within the 95% confidence interval ($p<0.05$).

2.2.12. Studies to detect NPs organ distribution

To test tumor targeting by NPs, a syngeneic mouse model of Lewis Lung carcinoma was used. In this model, LLC cells were first cultured in high-glucose Dulbecco's modified Eagle's medium (DMEM) supplemented with 10% fetal bovine serum (FBS) and 1% penicillin/streptomycin/amphotericin (PSA) to confluency. Cells were gently scraped off the plate, pelleted, and quantified. Mice were subcutaneously injected in the upper right dorsal area of their body with $1x10^7$ LLC cells to induce tumor growth in a 400 µL total volume composed of 200 µL ECM Growth factor reduced gel from Engelbreth-Holm-Swarm murine sarcoma (SIGMA), and 200 µL LLC cell suspension.

To determine targeted delivery into the tumor and other organs, 14-week-old C57BL6J male mice weighing 25g were used. Mice were injected with IRDye 680RD-labeled NPs 15 d after tumor implant. Before injection, mice were anesthetized with 1% isoflurane, and a tail vein injection of 0.15 mg of NPs was administered in a volume of 200 µL, following the protocol of Barcelo-Bovea *et al.* (2020) [4]. Five minutes after tail vein injection, mice were subsequently euthanized. Tumor and organs (brain, heart, lungs, spleen, kidneys, liver, and intestines) were quickly extracted and scanned for IR-labeled NP's distribution using the LI-COR Odyssey CLx infrared scanner. For the tumors, a 42 µm resolution and a high-quality setting were chosen in the Image Studio™. For the organs, a 337 µm resolution was used. All the tissue area was selected for quantification, and the IR signal was obtained using the Image Studio™ software. The percent increase in infrared signal from control mouse at 5 min after tail-vein injection was calculated following Barcelo-Bovea *et al.* (2020). All necessary approvals from the Institutional Animal Care and Use Committee (IACUC) were in place for the performed research: Assurance ID number: D16-00343, IACUC Protocol Universal Number: 048-2021-08-01-PHA-IBC.

2.2.13. Studies to determine NPs tumor decrease in mice

In view of the efficiency of NPs targeting the tumor tissue, we tested their efficiency decreasing tumors in mice. To do this, we used the Lewis Lung carcinoma mouse model as described above. NSCLC is a disease that mostly affects humans in their adulthood [120]. Considering this fact, we decided to use mice in their adulthood period as defined by Wang et al. (2020) [121]. Therefore, mice ranging from 36 to 60 weeks of age,

representing an age from adulthood to the reproductive senescence period, were selected for our studies. These mice were implanted cells to grow a tumor for a total of 12 days. Mice were injected intraperitoneally with 7mg/kg Cyt c nanoparticles of 169 nm at day 3, as an early-tumor stage intervention, and at day 8, as a late-stage intervention in tumor growth. Tumor volume was measured manually by caliper every 3 days using the length and width of the tumors:

$$Tumor\ volume = \frac{Tumor\ length * (Tumor\ weigth)^2}{2}, \quad (3)$$

The percentage of tumor growth from day 3 (when tumor is palpable and measurable by caliper), and day 12 (last day) was calculated using the following formula:

$$Tumor\ growth = \left(\frac{Volume\ at\ day\ 12 - Volume\ at\ day\ 3}{Volume\ at\ day\ 12}\right) * 100, \quad (4)$$

A total of n=6 mice were untreated and n=7 mice were treated with NP's. Unpaired t test with a Kolmogorov-Smirnov analysis by GraphPad Prism between NP-treated and untreated mice was considered statistically significant within the 95% confidence interval at p = 0.0385. Animal weight was also measured to monitor drug safety, as a sharp decrease in body weight (more than 15-20% during experiment) is considered unhealthy in tumor models [122]. No difference in mouse weight between groups was observed.

Chapter 3

Cytochrome c-based Nanoparticle Preparation via Nanoprecipitation Method: The Impact of Redox-Responsive Cross-Linking on Particle Size and Drug Delivery Properties

3.1. Summary

Many proteins are attractive substitutes for cytotoxic drugs due to their unique advantages as high selectivity and low toxicity [79]. For example, Cytochrome c (Cyt c) is an important mediator of apoptosis when released from the mitochondria to the cytoplasm. This process normally occurs in response to DNA damage, but in many cancer cells, it is most likely inhibited due to the inactivation of the upstream components of the p53 pathway [123]. The targeted delivery of Cyt c directly to the cytoplasm could selectively initiate apoptosis in most cancer cells. However, most proteins, including Cyt c, cannot cross lipid bilayer membranes [108]. Also, protein drugs have significant drawbacks, primarily related to their limited physical and chemical stability during storage and administration [124]. This makes it necessary to develop methods allowing for the intracellular delivery of sufficient amounts of Cyt c to induce apoptosis in the target cells.

For nanotechnology-enabled delivery of hydrophilic protein-based drugs, several nanocarrier systems have been used to protect the sensitive load and facilitate cellular uptake and crossing of biological barriers [114,117]. Recently our research group has been developing strategies for the intracellular delivery of Cyt c using the nanoprecipitation (solvent-displacement) method [4]. Production of Cyt c NPs by a non-solvent nanoprecipitation is a straightforward process. Nanoprecipitation is based on

reducing the quality of the solvent in which the main constituent of nanoparticles is dissolved. By mixing both phases, supersaturation of the protein occurs, followed by the formation of protein nuclei [6]. This technique is known to produce small-sized particles with a uniform distribution. Although we demonstrated that Cyt c delivered from a micellar-like NP system could potentially be an effective chemotherapeutic agent to treat cancer, it also recognized that the delivery system needs improvement to achieve better efficiency [4].

The need for attaining precisely controlled drug release has led to the establishment of various sustained release systems in recent years [125]. Cross-linking is an essential step for nanoparticle preparation, which influences the bio-availability of the drug and its release from the nanocarrier system [126]. It has been reported that controlled release of the drug from the DDS could maintain steadier drug levels in the bloodstream for more prolonged durations [5]. In addition, controlled drug release from NPs confers both temporal control and protection of the therapeutic cargo [127]. A thiol-cleavable cross-linker is an attractive candidate for intracellular drug release because the cytosol of cells is much more reducing than the extracellular space [64]. Consequently, the development of systems with a redox-sensitive behavior has been a significant area of focus in the development of smart drug delivery systems. Herein, we develop a protein-based NP that uses Cyt c as drug and carrier material with redox-responsive release properties. Since the NP consists of a water-soluble protein, cross-linking was essential to prevent the dissolution of the NP upon exposure to an aqueous environment (e.g., reconstitution buffer, blood).

Important factors to take into account when designing a nano-sized DDS are size, surface charge, shape, and hardness [128]. For in vivo applications, shape and size are critical determinants of nanoparticle uptake and circulation [129]. It has been found that DDS must accumulate through passive targeting (EPR effect) in the tumor site first to take advantage of active targeting strategies if incorporated into the system [53]. The optimal size range of 40-200 nm to ensure longer circulation time, increased accumulation within the tumor mass, and lower renal clearance [48]. Furthermore, the main physicochemical attributes of endocytosis-dependent cellular uptake of nanocarrier systems are reported to be the size and size distribution [130].

Then, this work aimed to report on the preparation of cross-linked Cyt c nanoparticles using an optimized non-solvent nanoprecipitation process. Special attention has been dedicated to a systematic study to understand the effect of the operating parameters of the nanoprecipitation method, such as cross-linker concentration, non-solvent/cross-linking injection rate, and cross-linking method variation (i.e., one-step and two-step) on the physicochemical and delivery properties of the nanoparticles. To the best of our knowledge, this is the first work investigating the impact of the cross-linking process on the preparation of Cyt c-based nanoparticles by the nanoprecipitation process.

3.2. Results

3.2.1. Effect of cross-linker (DSP) concentration

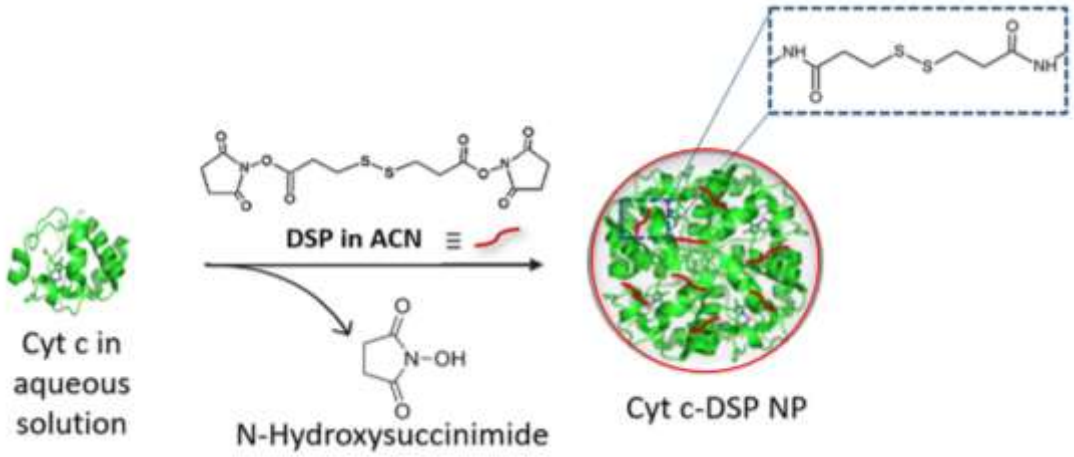

Figure 3.1. Synthesis route of cross-linked Cyt c NP by one-step nanoprecipitation.

To study the effect of the cross-linker concentration on nanoparticle characteristics formation, we used the one-step nanoprecipitation method described above in method *2.1.2.1* to achieve self-assembly of cross-linked Cyt c NPs. Briefly, Cyt c was solvent-precipitated from nanopure water by adding different concentrations (0.2, 0.3, 0.5, 1, 1.5 mg/mL) of DSP dissolved in acetonitrile (non-solvent) at a constant rate of 125 mL/h using an automated syringe (Figure 3.1.). It has been reported that the concentration of cross-linker affects the NP size [5,131-133]. The effect of cross-linking concentration on mean size, size distribution, zeta potential, and drug precipitation efficiency are shown in Table 3.1.

Table 3.1. Effect of cross-linker concentration on mean size, size distribution, zeta potential, and precipitation efficiency of cross-linked Cyt c NPs.

DSP concentration (mg/mL)	Diameter (nm)	Polydispersity Index (PDI)	Zeta Potential (mV)	Precipitation efficiency (%)
0.2	212 ± 1	0.04 ± 0.03	35.9 ± 0.4	80 ± 3
0.3	258 ± 8	0.11 ± 0.01	16.3 ± 2.5	80 ± 2
0.5	262 ± 8	0.13 ± 0.04	4.5 ± 0.8	95 ± 3
1.0	315 ± 50	0.32 ± 0.04	-2.0 ± 0.3	92 ± 1
1.5	434 ± 34	0.34 ± 0.09	-4.7 ± 0.6	97 ± 2

Table data shown are the mean ± SD of experiments performed in triplicate (n = 3).

Figure 3.2.a showed that the diameter of nanoparticles increased with an increase in cross-linker concentration for all NPs. Increasing the cross-linker amount from 0.2 to 0.5 mg/mL, the mean NP diameter increases from 212 to 262 nm with a polydispersity index (PDI) ≤ 0.1. The successive increase in cross-linker concentration from 1.0 to 1.5 mg/mL led to a significant increase in nanoparticle size from 315 to 434 nm (** $p = 0.003$) with higher size distribution (PDI ≥ 0.3) for both NP formulations. When comparing the NPs diameters, a significant difference among means was observed using ordinary one-way ANOVA with Tukey's multiple comparison analysis ($p < 0.05$). No significant differences were observed between the diameters of the NPs synthesized at cross-linker concentrations from 0.2 mg/ml to 0.5 mg/ml. Precipitation efficiency for all cross-linker concentrations used ranged from 80% to 97%. Statical analysis by ordinary one-way

ANOVA multiple comparison analysis demonstrated a significant difference among means of precipitation efficiencies (**** $p < 0.0001$).

The effect of the cross-linker concentration on the zeta potential value was also evaluated (Figure 3.2.b). An opposite semi-linear behavior was also observed in ZP values, as in the case of particle size. It was found that the zeta potential values decreased by increased cross-linker concentration. Zeta potential results showed that NPs prepared at 0.2 mg/mL of DSP concentration produces a higher zeta potential value (ZP = +35.9 ± 0.416 mV) than those obtained by using a greater DSP concentration of 1.5 mg/mL (ZP = -4.57 ± 0.238 mV). Thus, we selected a cross-linker concentration of 0.5 mg/mL for further experiments since it had the highest precipitation efficiency (95%) and the best particle size (262 nm) with narrow size distribution.

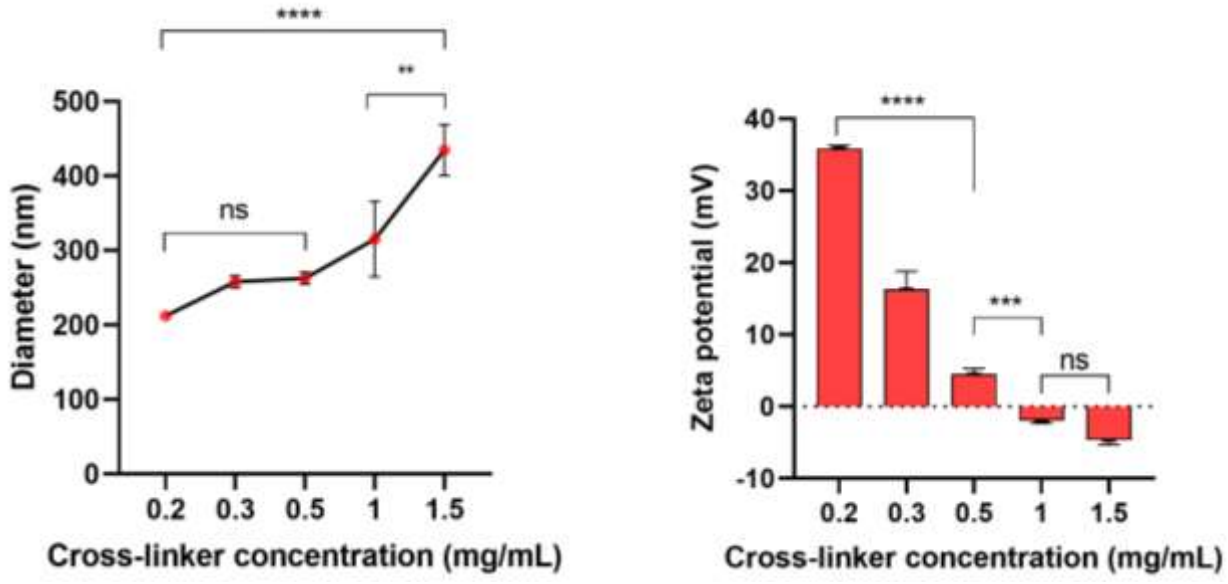

(a) **(b)**

Figure 3.2. Effect of cross-linker concentration (DSP) on mean diameter and zeta potential values of cross-linked Cyt c NPs. Data shown are expressed as the mean ± SD of experiments performed in triplicate (n = 3). Statical analysis by ordinary one-way ANOVA with Tukey's multiple comparison analysis demonstrated a significant difference in the mean sizes and zeta potential values of Cyt c NPs cross-linked by different concentrations. The asterisks indicate significant differences: ** p =0.003 *** p = 0.0005, and **** p < 0.0001. No significant (*ns*) differences were observed in mean diameters from 0.2 mg/mL to 0.5 mg/mL and zeta potential values between 1 mg/mL and 1.5 mg/mL of cross-linker concentrations.

The effect of cross-linking concentration on the morphological characterization of cross-linked Cyt c NPs was examined by scanning electron microscopy (SEM). SEM images (Figure 3.3.) showed that all lyophilized cross-linked Cyt c NPs synthesized at

different cross-linker concentrations were spherical in shape and generally uniform in size.

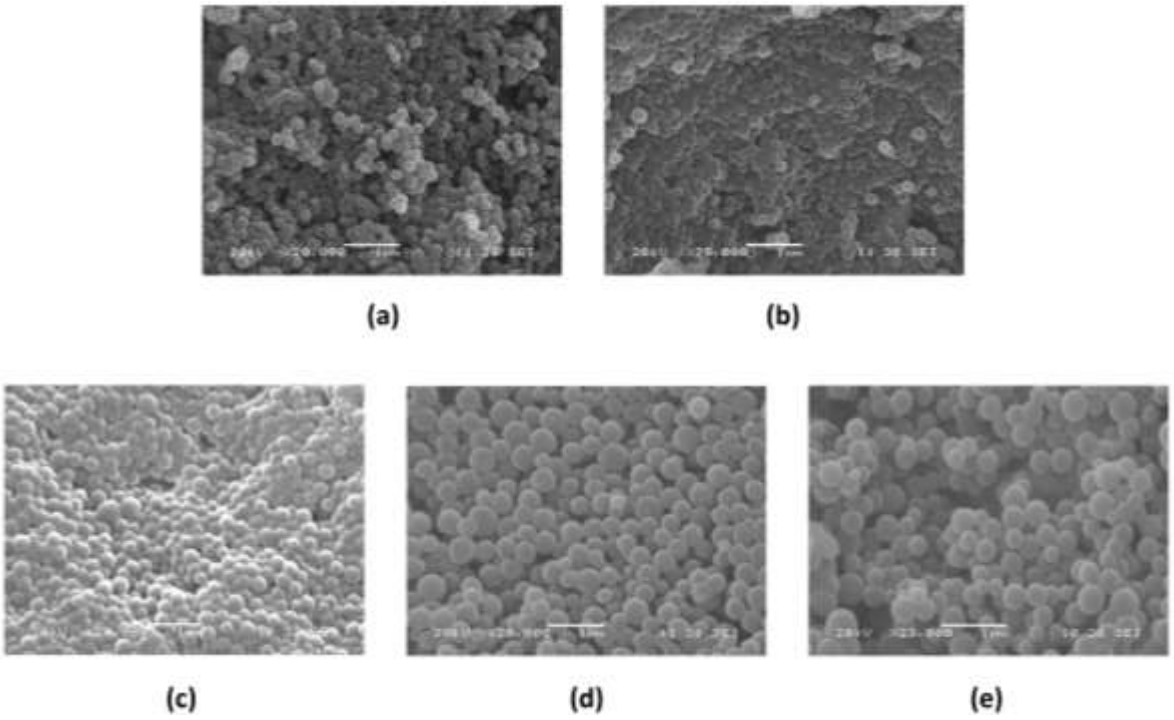

Figure 3.3. Effect of cross-linking concentration on morphological characterization of nanoparticles. SEM images of Cyt c NPs cross-liked with different concentration of DSP: (a) 0.2 mg/mL, (b) 0.3 mg/mL, (c) 0.5 mg/mL, (d) 1.0 mg/mL, and (e) 1.5 mg/mL. Scale bar = 1 µm.

3.2.3. Effect of non-solvent/cross-linking injection rate

To evaluate the effect of the non-solvent/cross-linking injection rate by one-step nanoprecipitation method on NP size and colloidal properties, different flow rates (125, 200, and 300 mL/h) of the non-solvent (cross-linker) agent were tested. All other parameters such as Cyt c concentration (10 mg/mL), cross-linker concentration (0.5 mg/mL DSP), and solvent:non-solvent ratio (1:4) were kept constant. The mean diameter,

zeta potential, and PDI values of the prepared cross-linked Cyt c NPs were determined by DLS. The non-solvent/cross-linking injection rate significantly impacts NP diameter ranging from 262 nm for the slower flow rate of 125 mL/h to 179 nm for the fastest flow rate of 300 mL/h, as shown in Table 3.2.

Table 3.2. Effect of non-solvent/cross-linking injection rate on mean size, size distribution, zeta potential, and precipitation efficiency of cross-linked Cyt c NPs.

Nanoprecipitation Rate (mL/h)	Diameter (nm)	Polydispersity Index (PDI)	Zeta potential (mV)	Precipitation Efficiency (%)
125	262 ± 8	0.13 ± 0.04	4.5 ± 0.8	95 ± 3
200	226 ± 2	0.06 ± 0.02	8.9 ± 1.4	97 ± 1
300	179 ± 4	0.04 ± 0.01	9.4 ± 3.2	95 ± 1

Table data shows the mean ± SD of each experiment performed in triplicate (*n* = 3).

Figure 3.4.a showed that the mean sizes of the prepared NPs were decreased by increasing the non-solvent/cross-linking injection rate. The polydispersity index of the three prepared NPs was less than 0.1 resulting in narrow size distributions. The smallest cross-linked Cyt c NP (179 nm) was prepared at 300 mL/h of non-solvent/cross-linking injection rate. As for zeta potential, by increasing the rate of cross-linking injection, it was observed that the values increased from 4.5 mV to 9.4 mV (Figure 3.4.b).

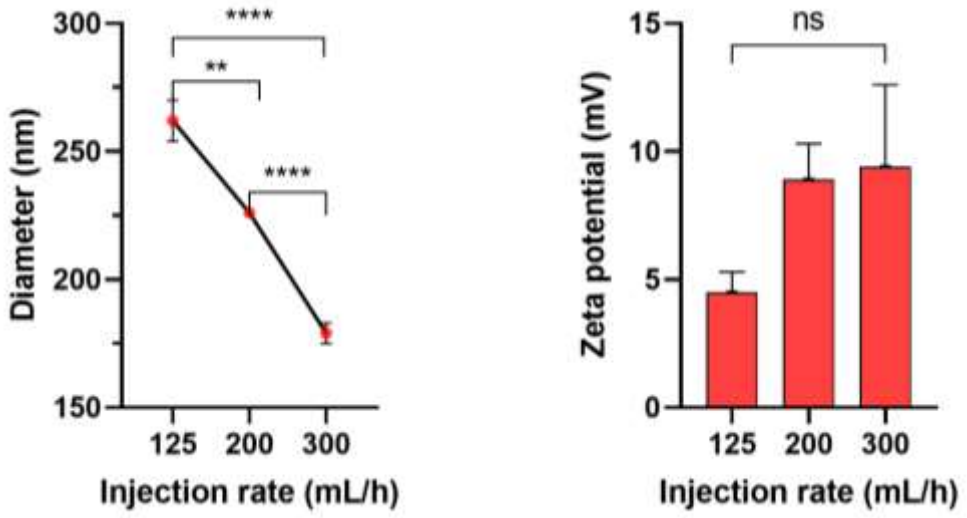

(a) **(b)**

Figure 3.4. Effect of non-solvent/cross-linking injection rate on (a) mean size and (a) zeta potential values of cross-linked Cyt c NPs. Data are the mean ± SD of experiments performed in triplicate (n = 3). Statical analysis by ordinary one-way ANOVA multiple comparison analysis demonstrated a significant difference between cross-linking injection rates on the mean size of NPs. The asterisks (*) indicate significant differences: ** p = 0.002, and **** $p < 0.0001$. No significant (ns) differences in zeta potential values between NPs prepared at different injection rates were observed.

In addition, SEM images of the cross-linked Cyt c nanoparticles at different cross-linking precipitation rates are shown in Figure 3.5. Optical examination by SEM showed spherical NPs with narrow size distribution for all cross-linked Cyt c NPs. The precipitation efficiency was above 95% for the three prepared NPs.

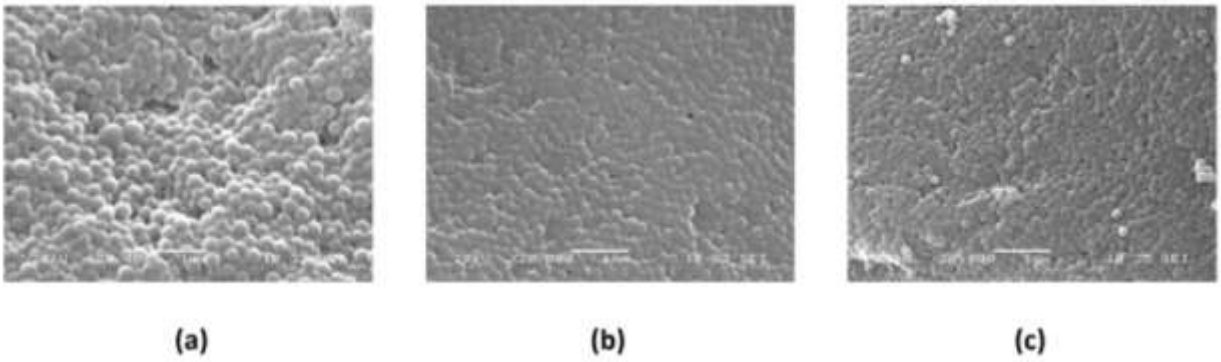

Figure 3.5. Effect of cross-linking injection rate on the morphological characterization of NPs. SEM images of Cyt c NPs cross-linked at different flow rate: (a) 125 mL/h, (b) 200 mL/h, and (c) 300 mL/h. Scale bar = 1 µm.

3.2.4. Effect of cross-linking method variation

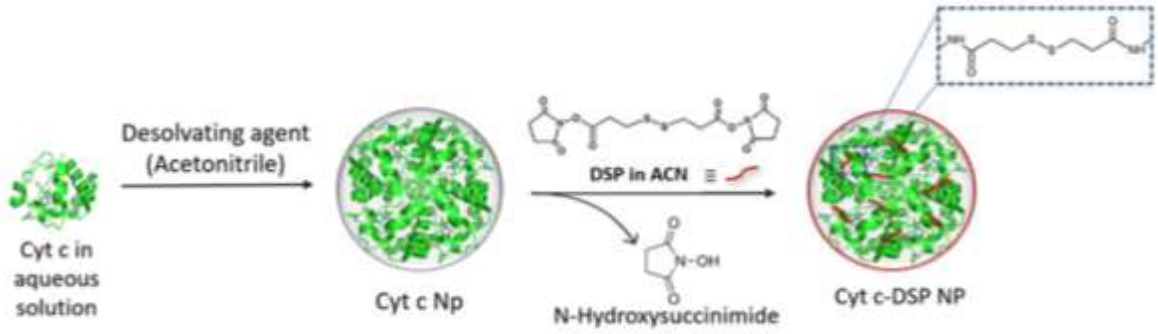

Figure 3.6. Synthesis route of cross-linked Cyt c NP by two-step nanoprecipitation.

Cyt c nanoparticles cross-linked with DSP were prepared using the nanoprecipitation (solvent-displacement) technique described above in method 2.1.2. We developed two cross-linking strategies: one-step and two-step approaches to evaluate the effect of varying cross-linking methods on NP size and drug delivery properties. For this purpose, all of the other parameters such as aqueous Cyt c (10 mg/mL), cross-linker

concentration (0.5 mg/mL DSP), solvent:non-solvent ratio (1:4), and nanoprecipitation injection rate (300 mL/h) were kept constant. In the first approach, aqueous Cyt c (solvent phase) was precipitated by direct addiction of the cross-linker dissolved in acetonitrile (non-solvent phase) in one-step synthesis. This strategy allows the NP core and shell to be formed together [134], stabilizing the NP structure by the cross-linker and reducing the time of the synthesis procedure. For the second strategy, aqueous Cyt c was first precipitated with acetonitrile to form Cyt c NPs (Figure 3.6.). Then, the synthesized Cyt c NPs was stabilized with the cross-linker dissolved in the non-solvent phase (acetonitrile). In the two-step strategy, the core is synthesized first, and then the shell layer is formed around the synthesized core surface [134].

Table 3.3. The effect of cross-linking method variation on the mean size and zeta potential values of cross-linked Cyt c nanoparticles.

Nanoprecipitation method	Diameter (nm)	Polydispersity Index (PDI)	Zeta potential (mV)	Precipitation Efficiency (%)
One-Step [a]	179 ± 4	0.04 ± 0.01	9.4 ± 3.2	95 ± 2
Two-Step [b]	189 ± 2	0.06 ± 0.02	18.6 ± 1.2	97 ± 1

[a,b] Table data show the mean ± SD of experiments performed in triplicate (n = 3).

The results of mean diameter, size distribution, zeta potential, and precipitation efficiency are shown in Table 3.3. The cross-linked Cyt c nanoparticles prepared by the one-step method had an average particle diameter of 179 nm with a very narrow size distribution (polydispersity index ≤ 0.05) and a positive zeta potential (+9.4 mV) (Figure 3.7.a). In contrast, Cyt c nanoparticles cross-linked by the two-step method had a mean

diameter of 189 nm with a narrow distribution (PDI ≤ 0.1) (Figure 3.7.b). For this formulation, the value of zeta potential was found to be +18.6 mV. It indicates that the synthesized Cyt c nanoparticles cross-linked by a one-step method could be expected to be more stable for a long time [5]. The precipitation efficiency was high for both cross-linking methods ranging from 95% for the two-step method to 97% for the one-step method.

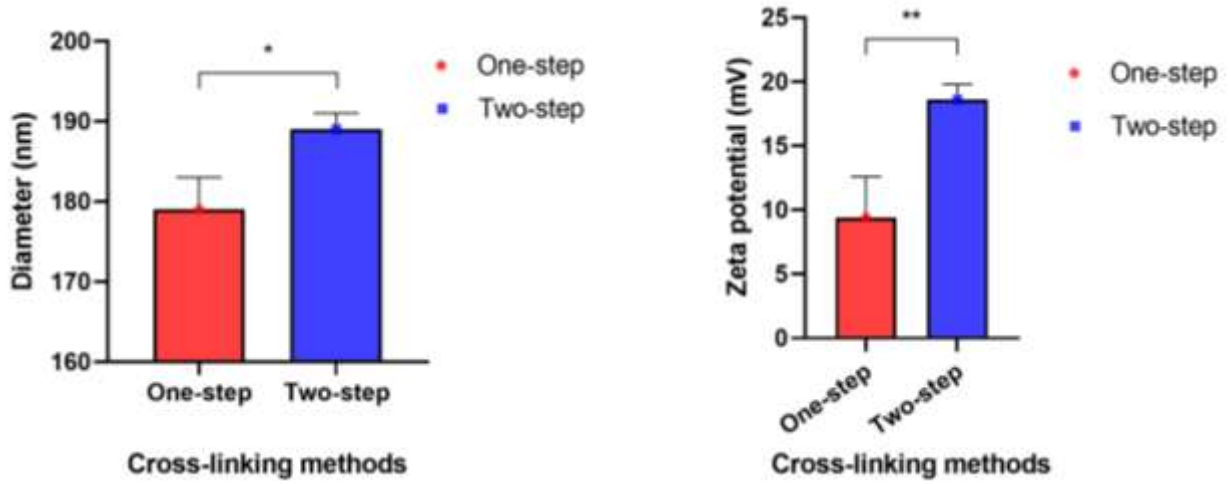

(a) **(b)**

Figure 3.7. The effect of cross-linking method variation on the (a) mean diameter and (b) zeta potential values of cross-linked Cyt c nanoparticles. Data shown are the mean ± SD of experiments performed in triplicate (n =3). The asterisks (*) indicate significant differences: * p = 0.02 and ** p = 0.01, assessed by two-tailed unpaired t-test analysis.

The morphological characteristics of NPs prepared by one-step and two-step cross-linking methods were examined by SEM. As shown in Figure 3.8., independent of the cross-linking approach, cross-linked Cyt c NPs were spherical and well homogeneous

in size distribution. Moreover, the average size of nanoparticles from SEM micrographs is relative to those obtained from dynamic light scattering measurements.

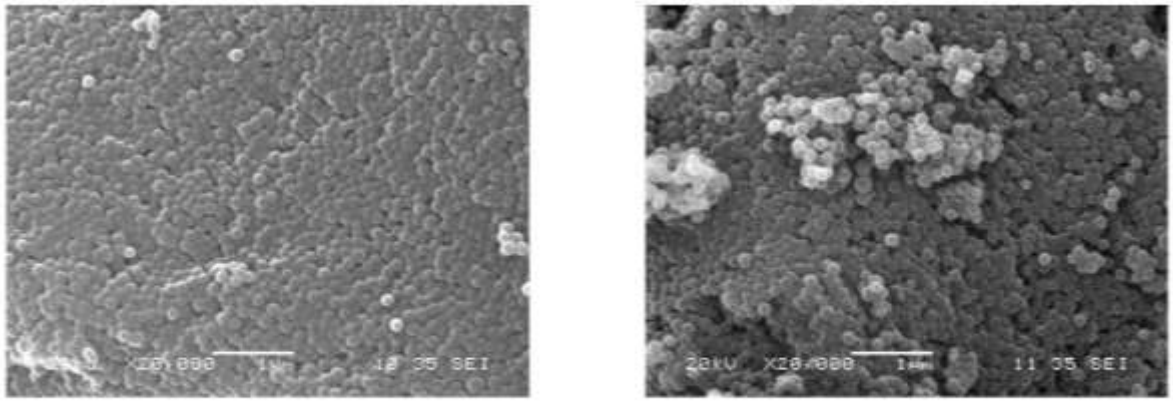

(a) (b)

Figure 3.8. SEM micrographs of the Cyt c NPs cross-linked by (a) one-step and (b) two-step nanoprecipitation methods. Cross-linker concentration (0.5 mg/mL DSP) and injection rate (300 mL/h) were maintained constant during nanoparticle formation. Scale bar = 1 µm.

To investigate the cumulative release profile of the cross-linked Cyt c NPs prepared by different cross-linking methods, we used 10 mM glutathione (GSH) to simulate intracellular conditions [119]. The cumulative Cyt c release profiles are shown in Figure 3.9. Both nanoparticles prepared by one-step and two-step cross-linking methods exhibited a burst release of Cyt c within 24 h of approximately 40% and 71%, respectively. The remaining Cyt c was released from both NPs in the same manner with a slower rate reaching up to 43% with the one-step method and 74% with the two-step cross-linking method within 72 hours.

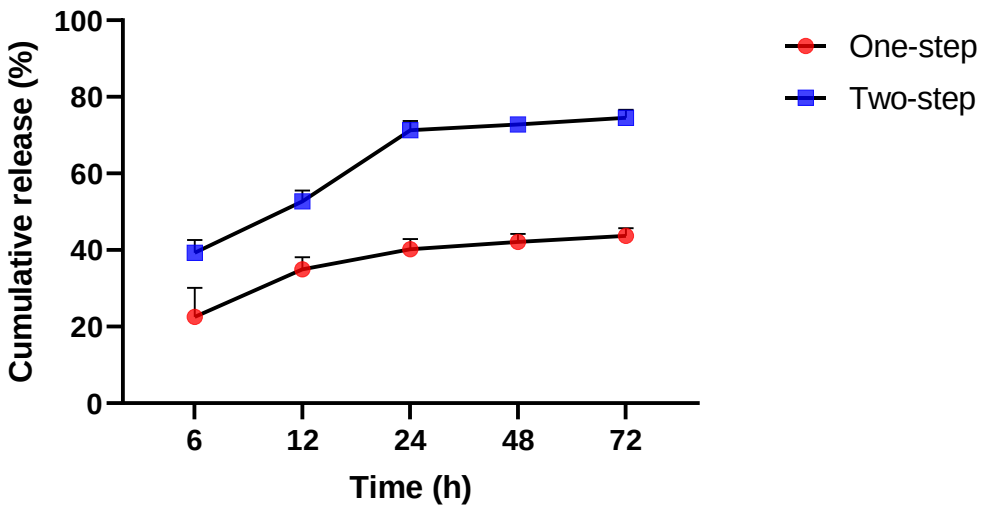

Figure 3.9. Cumulative in vitro release profile of Cyt c from cross-linked Cyt c NPs synthesized by one-step (red circle) and two-step (blue square) methods. NPs were dissolved in PBS buffer with 10 mM GSH at 37°C to simulate the intracellularly (reducing) physiological condition. Data are the mean ± SD of experiments performed in triplicate (*n*= 3). Statistical analysis by two-tailed paired t-test analysis demonstrated a significant difference between one-step and two-step cross-linking methods, ** $p < 0.05$.

We determined the potential of Cyt c to still interact with Apaf-1 and induce apoptosis after chemical cross-linking with different methods. For this purpose, in vitro cell-free caspase 3/7 activity assays were conducted in a cell-free system, and native Cyt c was used as a positive control. As shown in Figure 3.10., the addition of cross-linked Cyt c NPs prepared by both cross-linking methods to fresh cytosol produced caspase 3/7 activation. Compared to the untreated cells, activation of caspase 3/7 was statistically significantly higher in cells treated with NPs-prepared with both methods (****p* < 0.05). Cyt c NPs cross-linked by the one-step method had 69 ± 14 % of their caspase activation activity with no significant difference compared to native Cyt c. In contrast, Cyt c NPs

cross-linked by the two-step method activate caspase to 88 ± 13 % with no significant difference compared to native Cyt c. Therefore, since our NPs retained all of their enzyme activity, we demonstrated that the cross-linking methods used for the preparation of the NPs do not produce any adverse impact on the capability of the protein to induce apoptosis [135].

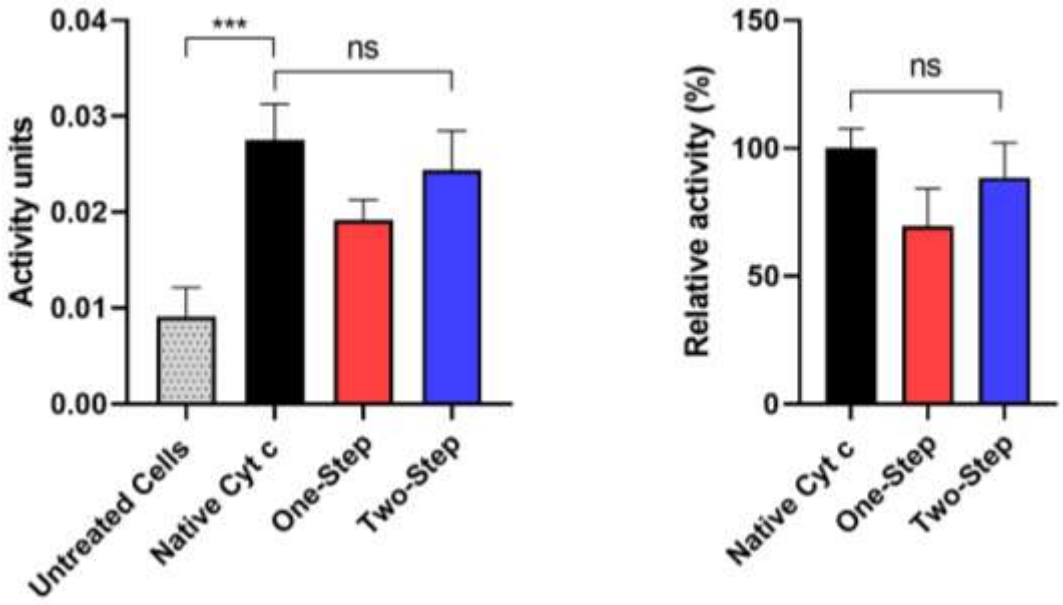

(a) **(b)**

Figure 3.10. Activation of caspase 3/7 using a cell-free caspase assay. (a) Compared to untreated cells (control), cross-linked Cyt c NPs synthesized by one-step and two-step methods activated caspase 3/7 to a similar extent to the activity provided by native Cyt c protein. (b) Relative caspase 3/7 activation of Cyt c NPs cross-linked by one-step and two-step methods compared with the relative activation by native Cyt c. When comparing the relative caspase activity of NPs obtained from one-step and two-step methods, no statistically significant (ns) difference was found using ordinary one-way ANOVA and

multiple comparison Tukey's test (95% confidence interval). Data are the mean ± SD of experiments performed in triplicate (n= 3); (*** p = 0.0007).

3.3. Discussion

Protein therapeutics have gained momentum in recent years and have become a pillar in treating many diseases, including cancer [104]. Protein drugs are attractive substitutes for cytotoxic drugs because they are highly specific, tunable, and less toxic than conventional small drug molecules [136]. Because of their importance, protein-based nanoparticle systems are already found in the market, such as albumin-bound paclitaxel NPs (Abraxane™) [137]. However, despite the success of early protein drugs, numerous challenges have reduced their efficacy in the clinical setting, such as physical and chemical stability during storage and after administration, limited therapeutic index, and inefficient delivery [80]. Cyt c, a pro-apoptotic protein, could potentially be used to target and specifically destroy cancer cells if it is delivered into the cytoplasm. Previous studies found that the nanoprecipitation method was useful for preparing Cyt c-based NPs [117,138]. Herein, we developed a Cyt c-based NP that uses the protein as a drug and carrier material with redox-responsive release properties.

It is well-known that the physicochemical characteristics of nanoparticles, including size, shape, and stability, influence the functional properties and effectiveness of drug delivery [139]. Also, it has been reported that the size, size distribution, surface charge, and delivery properties of nanoparticles are highly influenced by the nanoprecipitation operation conditions [6,140]. Therefore, we evaluated the impact of the cross-linking

process on the physicochemical and functional properties of Cyt c nanoparticles prepared by the nanoprecipitation method.

For the current study, we developed a simple and straightforward method to prepare cross-linked protein-based nanoparticles based on an optimized one-step nanoprecipitation procedure with controllable and appropriated particle size and size distribution for drug delivery applications. In this method, aqueous Cyt c was precipitated by direct addiction of the cross-linker dissolved in the non-solvent phase (acetonitrile) in a single-step approach. This new simplified strategy allows the NP core and shell to be formed together [134], stabilizing the NP structure by the cross-linker and reducing the time of the procedure. However, it has been reported that the cross-linker concentration affects the size of the produced nanoparticle [5,131-133]. Therefore, we evaluated the effect of DSP concentration on Cyt c NP characteristics formation. The results showed that NP diameter increased with an increase in cross-linker concentration for all cross-linking concentrations. The optimum amount of DSP needed for effective cross-linking of the Cyt c nanoparticles was 0.2 mg/mL. This amount of DSP yielded particles with the smallest average size of 212.4 nm and a very narrow size distribution (PDI < 0.1). Amounts of cross-linker higher than 1.5 mg/mL yielded larger particle size and broader size distribution (PDI ≥ 0.3). This behavior can be explained because increased cross-linker concentration could facilitate agglomeration, forming larger NPs [141]. In addition, the results showed that zeta potential decreased with an increase in cross-linking concentration. Thus, the zeta potential decrease serves as a control for successful surface cross-linking by DSP [142]. The zeta potential is also related to particle stability. Samples with zeta potentials higher than 30 mV and −30 mV are considered stable [143].

Therefore, Cyt c nanoparticles cross-linked with 0.2 mg/mL DSP possessed the highest colloidal stability with a zeta potential value of +35.9 mV. These values represent the magnitude of the electrostatic forces around the NP, which can repulse or attract neighboring particles and produce flocculation by NP aggregation or a stable suspension. The small size and narrow distribution of the NPs could indicate that the DSP reacted with amino groups on the same particle rather than linking two particles together [144]. This might be due to the zeta potential of the particles, which prevents them from coming close together. On the contrary, larger NPs with higher distribution and lower zeta potential could indicate aggregation through the random intermolecular association of some other molecules, resulting in different-sized particles [145]. SEM images showed that all prepared nanoparticles were a spherical shape, generally uniform in size, and well dispersed. The precipitation efficiency for all cross-linker concentrations was relatively high, ranging between 80 to 97%. Therefore, for further studies, we selected a cross-linker concentration of 0.5 mg/mL since it had the best size distribution and maximum encapsulation efficiency (95%) when compared statistically (**** p <0.0001).

Variations in particle size and zeta potential values were also studied as a function of the non-solvent/cross-linking injection rate, keeping the cross-linker concentration constant. The results showed that the cross-linked Cyt c particle size decreased significantly by increasing the non-solvent/cross-linking flow rate from 125 to 300 mL/h. The smallest NP was prepared at 300 mL/h. The classic theory of nucleation can explain the size reduction [116]. As it is well known, the non-solvent precipitation process is divided into four phases, including generation of supersaturation, nucleation, growth, and coagulation. It is also known that the supersaturation conditions could affect the size of

final nanoparticles [146]. The high and rapid supersaturation will increase the nucleation rate, which induces the formation of a more number of nuclei in the initial stage of the nucleation process, giving rise to fast particle growth and smaller nanoparticles [116,146]. In addition, the degree of supersaturation is governed by the addition rate of the non-solvent phase (cross-linker) [6]. Therefore, when the non-solvent/cross-linking injection rate increases, the supersaturation rate and degree of nucleation increase, and smaller nanoparticles can be obtained [116]. As for zeta potential, the non-solvent/cross-linking injection rate does not significantly affect its value. Particles from all formulations have zeta potential values between 4.5 and 9.4 mV. These values could indicate the good colloidal stability of particles since the increase of positive zeta potential value leads to less attraction between particles and, consequently, less aggregation [147]. SEM images showed cross-linked Cyt c spherical-shaped nanoparticles for all non-solvent/cross-linking injection rates. Also, the precipitation efficiency is above 95% for all amounts of cross-linker, leading to stabilizing the nanosuspensions.

For further investigation, we compared the one-step cross-linking/nanoprecipitation method studied above with the previously reported procedure, a two-step approach, to evaluate the effect of varying the cross-linking process on particle size and delivery properties [148,149]. In the second strategy, aqueous Cyt c was first precipitated with acetonitrile to form Cyt c NPs. Then, the synthesized Cyt c NPs was stabilized with the cross-linker dissolved in the non-solvent phase (acetonitrile). In the two-step method, the core is synthesized first, and then the shell layer is formed around the synthesized core surface [134].

For Cyt c NPs cross-linked with the one-step method, the mean size was smaller (179 ± 4 nm) than the two-step method (189 ± 2 nm) (*p = 0.02). This variation in NP size could be explained by the fact that the nanoparticles synthesized by the one-step method built a structure denser and more cohesive, leading to the convective loss of water during the cross-linking process [150]. The narrow size distribution for both methods could indicate that the DSP reacted with amino groups on the same particle rather than by linking two particles together [144]. As for zeta potential, NPs synthesized by the two-step method showed a more positive zeta potential than the one-step method. That could be because the one-step method allows the NP core and shell to be formed together [134], cross-linking more amines and reducing the positive charge in the protein. The zeta potential is commonly related to particle stability. Thus, cross-linked Cyt c NPs synthesized with the two-step nanoprecipitation method possessed the highest colloidal stability and could be expected to be more stable for a long time upon exposure to an aqueous environment. The precipitation efficiency for both methods practically was 97%. The SEM micrographs showed that apart from the small sizes and PDI, Cyt c nanoparticles cross-linked by both methods had a smooth structure without wrinkle or concave on the surface.

The in vitro Cyt c release from cross-linked NPs demonstrated a controlled release profile for both methods. The two-step nanoprecipitation method demonstrated more release properties with 71% of Cyt c released in the initial 24 h compared with the 40% of the one-step method. In vitro drug release of NPs prepared by nanoprecipitation generally consists of two phases [76]. The first phase consists of “burst release”, followed by the second phase of “prolonged release”. The first phase is due to the release of drug

substance, which is adsorbed on the NPs surface or dispersed near the surface [76]. The second phase is due to the release of drugs in the core compartment [151]. Thus, these behaviors can be attributed to the fact that the NPs synthesized by the one-step method have more cross-linked proteins in the core, reducing the “burst release”, which could cause a more slow and prolonged release of the protein drug.

Finally, cross-linking is essential for nanoparticle preparation but can affect biodegradability and drug release from the carrier system [140]. Because the binding of Cyt c to apoptosis protease activation factor-1 (Apaf-1) is a critical activation step in the execution phase of apoptosis, we evaluated the capability of Cyt c to activate caspases activity [135]. Our result demonstrated that cross-linked Cyt c NPs retained all their enzyme activity through a cell-free caspase 3/7 activation assay, meaning that the integrity of Cyt c after both NP formulation procedures was not compromised. No significant differences were observed between the one-step and two-step nanoprecipitation methods. Therefore, in this work, we demonstrated that both nanoprecipitation methods (i.e., one-step and two-step) could be used to synthesize protein-based NPs with an appropriate size, narrow size distribution, high precipitation efficiency, high colloidal stability, controlled release properties, and conserving the bioactivity of the protein drug.

Future work to improve the designed system includes the addition of a targeting mechanism to allow cell internalization and targeted cell uptake in vitro and in vivo. Additional surface modifications, such as polyethylene glycol (PEG) polymer, can also be incorporated to enhance circulation times in vivo. Moreover, further studies with other protein drugs are needed to determine if the one-step nanoprecipitation method can be

used to prepare protein-based nanoparticles. Finally, our system can be used to co-deliver other cytotoxic drug combinations and provides a model for future personalized medicine applications.

3.4. Conclusion

Nanosized delivery systems hold promise in improving protein delivery to target tumors. A convenient method to accomplish nanosized protein-based nanoparticles is by nanoprecipitation. The current study established a simple and straightforward nanoprecipitation method for preparing “smart” protein-based nanoparticles with an appropriated particle size (<200 nm) and narrow size distribution for redox-sensitive drug delivery applications. Optimization of the processing parameters involved in the new one-step cross-linking/nanoprecipitation method was evaluated. We found that the concentration of the crosslinker solution in the one-step nanoprecipitation method affects the physicochemical properties of nanoparticles, increasing the particle size with an increase in DSP concentration. In addition, the diameter of Cyt c NPs decreases as the cross-linking/nanoprecipitation rate increases. For further evaluation, we selected a DSP concentration of 0.5 mg/mL and a non-solvent flow rate of 300 mL/h as optimum conditions to study the effect of varying the cross-linking method to a two-step nanoprecipitation. Our results showed that the Cyt c-based nanoparticles could be cross-linked with both nanoprecipitation methods, in which the one-step method demonstrated to obtain the smallest particle size of 179 ± 4 nm with a very narrow distribution. However, the two-step method demonstrated a more efficient drug release profile. Finally, the activity of encapsulated Cyt c is mainly conserved after cross-linking process using both nanoprecipitation methods. Therefore, it can be concluded that the non-solvent

nanoprecipitation method using a one-step or two-step cross-linking approach presents an excellent opportunity for the smart delivery of Cyt c as a therapeutic protein for cancer treatment.

Chapter 4

Folate-Decorated Cross-Linked Cytochrome C Nanoparticles for Active Targeting of Non-Small Cell Lung Carcinoma (NSCLC)

4.1. Summary

Lung cancer is the leading cause of worldwide cancer deaths. Non-small cell lung carcinoma (NSCLC) is the most common type of lung cancer, accounting for 85% of the reported cases, and is associated with poor prognosis with a five-year survival rate of only 15% [7,152]. Although the current first-line anticancer agents (e.g., Cisplatin and Taxol®) for NSCLC have been successful to some extent, their main drawbacks are non-specific targeting, high-dose requirements, poor bioavailability, development of multiple drug resistance, and adverse side effects [97,153,154]. For example, NSCLC patients treated with cisplatin often suffer severe nephrotoxicity [155]. In principle, these effects arise from the chemotherapeutic agents' lack of tumor selectivity and systemic toxicity without discriminating healthy tissues, producing unwanted and often severe and dangerous side effects.

All chemotherapeutic drugs, regardless of their specific target or mechanism of action, produce the same cytotoxic end effect in sensitive cells: apoptotic cell death. However, the apoptotic DNA damage response requires the involvement of the p53 tumor suppressor pathway, which is mutated/inactivated in ~50% of human cancers [156] and approximately 70% of lung adenocarcinoma cases [157]. Such oncogenic mutations that disrupt the apoptosis pathway contribute to tumor initiation, progression, and metastasis [158]. For example, Taxol® causes damage leading to p53 tumor suppressor-dependent apoptosis and often results in the development of resistance, leading to therapy failure

and relapse [97]. Such limitations of the conventional chemical drugs have spurred efforts to identify more effective chemotherapeutic agents that can be tolerable in higher doses and act independently of the p53 pathway [159].

As an innovative alternative, many protein species exhibit potent cytotoxic activities that can be exploited to develop new anti-tumor drugs [160]. On this basis, Cytochrome C (Cyt c) fulfills this requirement because it is non-toxic in the cytoplasm and acts downstream in the apoptosis cascade, thus evading many steps with potential mutations. During Cyt c-mediated apoptosis, the apoptosome formation (Apaf-1/Cyt c complex), which cleaves procaspase-9 to active caspase 9, is a critical event responsible for activating effector caspases 3 and 7 that mediate apoptosis [161,162]. Indeed, using a drug delivery system to transport Cyt c into the cytoplasm of cancer cells could help overcome any failure in activating the intrinsic or 'mitochondrial' apoptotic signaling pathway preventing Cyt c release [102,159,163]. Hence, Cyt c has drawn the attention of groups in the field due to its potential to be developed into a highly effective and selective anticancer drug [123]. However, since Cyt c is a cell membrane-impermeable protein, it must be linked to an uptake process.

Folic acid is a vitamin B, necessary for cellular proliferation, DNA synthesis, and modification [55]. The folate receptor alpha (FR) is a well-known tumor marker that is overexpressed in 40% of human cancers, and it is rarely expressed or inaccessible in most normal cells [59]. Studies have found that levels of FR expression are associated with tumor stage and survival, specifically in lung adenocarcinomas [57,58]. This overexpression in tumors promotes folic acid (FA) ligand-drug conjugates to binding and

subsequent uptake via receptor-mediated endocytosis [60]. Hence, FA has been extensively used as a ligand to improve tumor therapy uptake and target cancerous cells.

One of the most influential hallmarks of cancer cells is their ability to sustain proliferative and pro-angiogenic signaling, leading to the leaky vasculature accompanied by insufficient lymphatic drainage in tumors (EPR effect), driving to accumulation of nano-sized delivery systems in solid tumors [164]. The EPR effect alone increases the tumor specificity of NPs by 20-30% over critical normal organs [53]. The polyethylene glycol (PEG) polymer has been used to modify nanoparticles (NPs) and overcome their low stability, immunogenicity, and short blood circulation half-life [165]. Combining the passive EPR-mediated targeting with an additional tumor-abundant ligand such as FA not only amplifies the specificity of therapeutic NPs but also facilitates their cellular uptake. For the in vivo application, it has been reported that shape and size are critical for nanoparticle uptake and circulation [166,167]. Spherical particles that are 100-200 nm in size have the highest potential for prolonged circulation because they are large enough to avoid uptake in the liver (particles over 300 nm accumulate in the liver) but small enough to prevent filtration to the spleen (as the spleen has fenestrations that do not exceed 200-500 nm) [48]. Typically, nanoparticles are trapped by mechanical filtration in the spleen sinusoids, followed by removal from circulation by cells of the reticuloendothelial system in the liver [24].

To date, various nano vehicles have been explored to facilitate intracellular delivery of Cyt c for therapeutic purposes with different degrees of success [44,114]. Recently, our research group overcame biocompatibility and off-target limitations commonly seen in anticancer therapeutics by designing a Cyt c-based drug delivery

system (DDS) coated with a biodegradable polymer PLGA-PEG-FA that is in size of 253 nm [4]. This DDS showed no sign of cytotoxicity after in vivo injection using a lung carcinoma immune-competent mouse model [4].

Herein we substantially simplify the system by employing another strategy preventing protein dissolution in buffer and blood, using redox-sensitive cross-linking. Cyt c NPs were prepared by solvent precipitation. Protein nanoprecipitation is an easy and reproducible technique to prepare Cyt c NPs. Their size, shape, and surface charge can be controlled to incorporate passive, active, and stimuli-responsive targeting [168]. Next, the Cyt c-based NPs were stabilized by homo-bifunctional reversible cross-linking using dithiobis(succinimidyl propionate) (DSP). This cross-linker contains a disulfide bond that is reduced under intra-cellular conditions, thus affording the dissolution of the NPs in the cytoplasm of target cells. To achieve receptor-mediated internalization by FR-overexpressing cancer cells, we conjugated folate-poly(ethylene glycol) (FA-PEG) to the surface of the NPs. Our data demonstrate a substantial improvement over our previous Cyt c delivery system in vitro, using the Lewis Lung Carcinoma (LLC) cell line, and in vivo, using a syngeneic (immune-competent) lung carcinoma mouse model. The LLC mouse model is practical in vivo approach to study if targeted NP therapies reach their target in the presence of a functional immune system [169].

4.2. Results

4.2.1. Synthesis and characterization of cross-linked Cyt c-PEG-FA nanoparticles

The diameter of cross-linked Cyt c NPs was 164 ± 5 nm, and Cyt c-PEG-FA NPs was 169 ± 9 nm (Table 4.1.). The NPs generated here were smaller compared to the core-shell Cyt c delivery systems we used previously. The decrease in the zeta potential of the cross-linked Cyt c-PEG-FA NPs (17.7 ± 1.7 mV) compared with the Cyt c-DSP NPs (27.5 ± 3.9 mV) confirmed the successful attachment of the FA-PEG-NHS targeting polymer to the amino groups of Cyt c, leading to a reduction in the number of positive charges on the NP surface.

Table 4.1. Size, polydispersity index, zeta potential, and precipitation efficiency of different NPs prepared by the nanoprecipitation method.

NPs	Diameter (nm)	Polydispersity Index (PDI)	Zeta potential (mV)	Precipitation Efficiency (%)	Actual Loading (%)
Cyt c-DSP NPs	164 ± 5	0.06 ± 0.01	27.5 ± 3.9	96 ± 2	80 ± 3
Cross-linked Cyt c-PEG-FA NPs	169 ± 9	0.09 ± 0.01	17.7 ± 1.7	97 ± 3	74 ± 6

Table data show the averages of three batches of NPs prepared and the respective standard deviations.

Scanning electron microscopy (SEM) was performed to examine the shape of the NPs (Figure 4.1. b,c). The SEM images of lyophilized cross-linked Cyt c NPs and cross-linked Cyt c-PEG-FA NPs showed a spherical shape with a narrow size distribution.

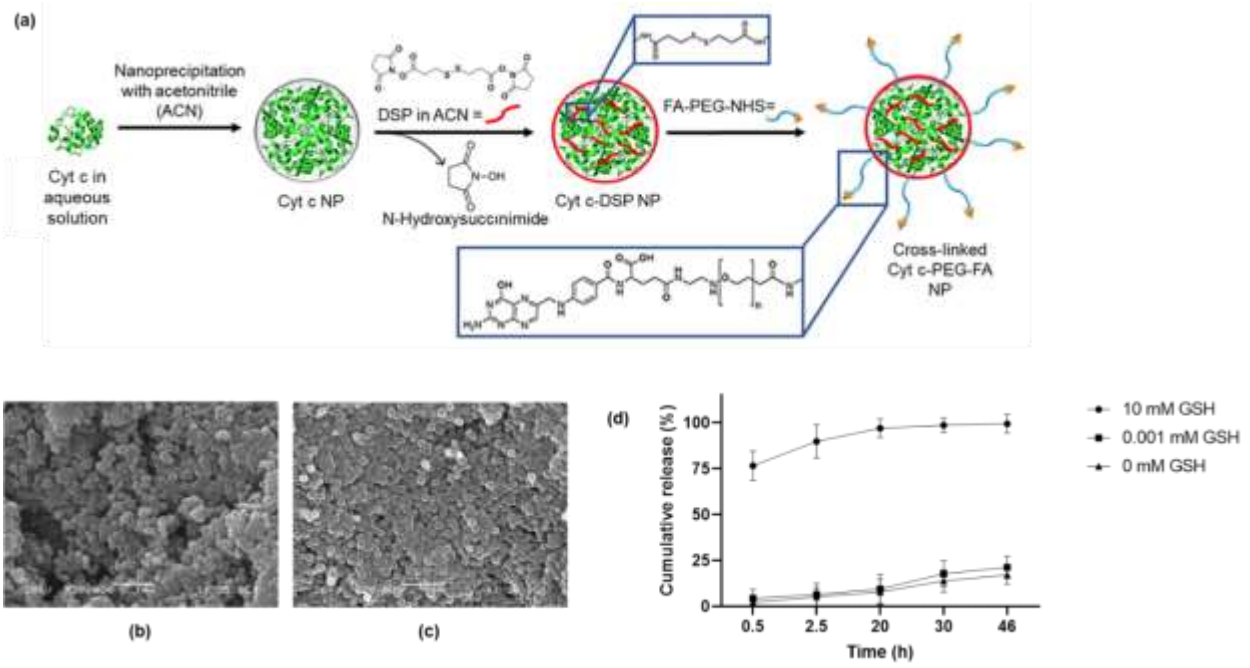

Figure 4.1. (a) Synthesis route of cross-linked Cyt c-PEG-FA NPs. SEM micrographs of (b) cross-linked Cyt c NPs and (c) cross-linked Cyt c-PEG-FA NPs. (d) Cumulative in vitro release profile of Cyt c from cross-linked Cyt c-PEG-FA NPs at 37 °C. NPs were dissolved in PBS buffer with zero GSH (triangles), 0.001 mM GSH (squares), and 10 mM GSH (circles) to simulate extracellular (non-reducing) and intracellular (reducing) physiological conditions. Data are the mean ± SD of experiments performed in triplicate. Statistical analysis by ordinary one-way ANOVA multiple comparison analysis demonstrated a significant difference between the intracellular and extracellular conditions when compared with the control, $p < 0.0001$.

4.2.2. In vitro redox-responsive release

To investigate the cumulative release profile of the cross-linked Cyt c-PEG-FA NPs, we used 10 mM glutathione (GSH) to simulate intracellular conditions, 0.001 mM GSH to simulate extracellular conditions and 0 mM GSH as control [170]. The cumulative Cyt c release profile is shown in Figure 1d. The cross-linked Cyt c-PEG-FA NPs exhibited an efficient release profile under reducing conditions (10 mM GSH); most Cyt c was released in the first 0.5 hours as a "burst release". In contrast, we found that only about 17% and 21% of Cyt c were released using no- or 0.001- mM GSH, respectively, and this release was slower than 10 mM GSH.

4.2.3. Cell-free caspase 3 and 7 assay

We determined the potential of Cyt c to still interact with Apaf-1 and induce apoptosis after the NP formulation. For this purpose, *in vitro* cell-free caspase 3/7 activity assays were conducted in a cell-free system (LLC lysate), and native Cyt c was used as a positive control. As shown in Figure 4.2., the addition of cross-linked Cyt c-PEG-FA NPs to fresh cytosol produces caspase 3/7 activation. Compared to the untreated cells, activation of caspase 3/7 was statistically significantly higher in cells treated with the cross-linked Cyt c-PEG-FA NPs at a p-value of <0.05 (Figure 4.2.a). Cyt c-PEG-FA NPs had 94 ± 8 % of their caspase activation activity with no significant difference compared to native Cyt c (Figure 4.2.b). Therefore, since our NPs retained all of their enzyme activity, we demonstrated that the conjugation of the Cyt c NPs does not produce any adverse impact on the capability of the protein to induce apoptosis.

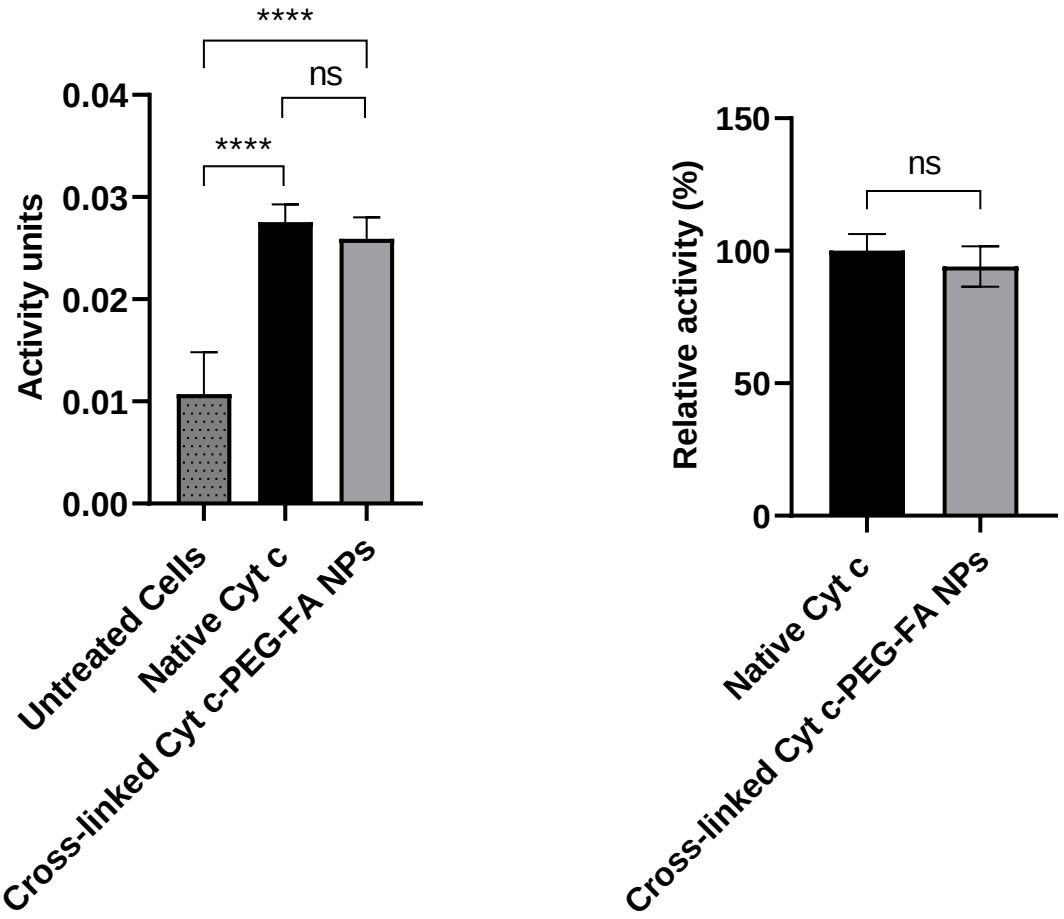

(a) **(b)**

Figure 4.2. Activation of caspase 3/7 using a cell-free caspase assay. (a) Compared to untreated cells (control), cross-linked Cyt c-PEG-FA NPs activated caspase 3/7 to a significantly greater extent, similar to the activity provided by the native Cyt c protein. (b) Caspase 3/7 activation of cross-linked Cyt c-PEG-FA NPs compared with the caspase 3/7 activation by native Cyt c. LLC lysate treated with cross-linked Cyt c-PEG-FA NPs was able to activate the caspase 3/7 significantly, similar to that afforded by native Cyt c. The relative caspase activity offered by cross-linked Cyt c-PEG-FA NPs was not significantly different compared to the native Cyt c protein. **** Indicates a significant

difference ($p < 0.0001$) in an unpaired t-test analysis with $n = 6$. Error bars represent the calculated SD.

4.2.4. Cell viability assays

The cytotoxicity evaluation of cross-linked Cyt c-PEG-FA NPs was performed using an MTS assay. A dose-response graph was constructed upon incubation of FR-positive LLC cells at different concentrations (300, 200, 100, 50, 25, and 12.5 µg/ml) of cross-linked Cyt c-PEG-FA NPs for 24 h. As shown in Figure 4.3., cross-linked Cyt c-PEG-FA NPs induced a significant reduction in LLC cell viability in a dose-dependent manner after 24 h of incubation compared to untreated cells. The calculated IC_{50} value of the cross-linked Cyt c-PEG-FA NPs was 47.5 µg/ml (R^2 =0.9681). Additionally, cell viability decreased at increasing concentrations of our NPs. These results demonstrated a clear correlation between the dose concentration of the NPs and its cytotoxic effect. As controls, LLC cells were incubated with native Cyt c, FA-PEG, and Cyt c-DSP NPs (folate-free, cross-linker alone) at the highest NP concentration (300 µg/ml) as in the corresponding experiment for 24 h. No significant cytotoxicity was observed after 24 h with either control compound. For native Cyt c control, it was expected not to significantly affect cell viability since Cyt c is a cell membrane-impermeable protein. As hypothesized, under the same conditions, folate-conjugated Cyt c NPs significantly reduced the cell viability of folate receptor-expressing LLC cells, compared to the folate-free Cyt c NPs (****$p < 0.0001$, $n=9$). These results validated that folate-conjugation is required for our NPs to address targetability and induce cytotoxic potential.

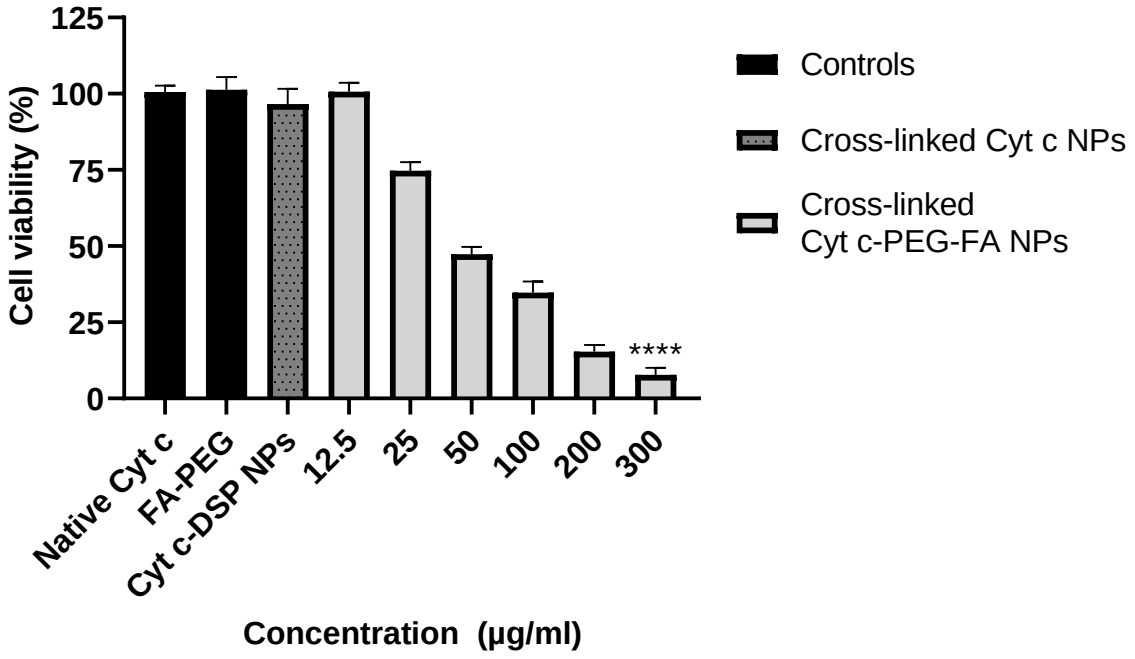

Figure 4.3. MTS cell viability assay of LLC cells after 24 h of incubation with folate-containing cross-linked Cyt c-PEG-FA NPs in a concentration-dependent manner. The percent of cell viability for the Cyt c-PEG-FA NPs is shown in gray columns, at increasing concentrations from 12.5 to 300 µg/ml. This dose-response curve was used to determine the IC_{50} value of the cross-linked Cyt c-PEG-FA NPs. As controls, we used the native Cyt c (protein alone, no NPs; first black column), PEG-FA (Folate-poly(ethylene glycol)-succinimidyl ester alone; second black column), and Cyt c-DSP NPs (Cyt-c with the homo-bifunctional cross-linker DSP, without folate; gray dotted column). All controls were added at a concentration of (300 µg/ml). Cytotoxicity of the folate-free formulation and the folate-bearing NPs at the highest concentration were compared by unpaired t-test analysis (****, $p< 0.0001$, $n= 9$). Data shown are expressed as the mean ± SD.

The FR is overexpressed in most cancer cells and has been widely used as a model for addressing the targetability of many therapeutic agents. To evaluate the selective cytotoxic effect of cross-linked Cyt c-PEG-FA NPs for FR-positive cancer cells, we made a comparative cell viability study with both FR-positive cells (human cervical carcinoma HeLa cell line) and FR-negative cells (mouse embryo fibroblasts NIH-3T3 cell line) [171,172]. As seen in Figure 4.4., cross-linked Cyt c-PEG-FA NPs significantly reduced cell viability in FR-positive cell lines (LLC and HeLa cells) without statistically significant difference ($p < 0.05$, $n=9$). Furthermore, the viability of the NIH/3T3 cells was not significantly affected after 24 h incubation with the folate-conjugated NPs. These cells have an undetectable level of FR on the cell surface. These results confirm that our FR-targeted DDS had a significant cytotoxic effect on cancer cells overexpressing FR and not on normal cells.

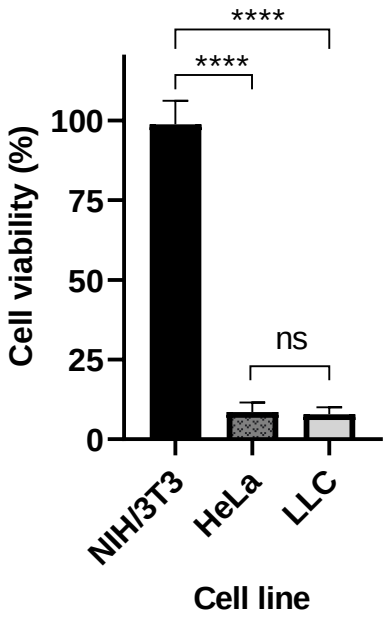

Figure 4.4. Comparison of the cytotoxicity of cross-linked Cyt c-PEG-FA NPs in cancerous and non-cancerous cell lines. Cell viability MTS assay after 24 h of NPs

treatment at 100 µg/ml using FR-positive cells (LLC and HeLa cells) and FR-negative cells (NIH/3T3 cells). The mean ± SD was obtained from three independent experiments performed in triplicate. The results were analyzed statistically using an unpaired t-test (****, $p < 0.0001$, n=9).

4.2.5. Study of apoptotic mechanism of cell death induction by CLSM

To confirm if cell death was caused by apoptosis, we qualitatively evaluated the occurrence of nuclear segmentation, chromatin condensation, and PI presence in the cell nuclei after treatment with NPs. LLC cells were treated with cross-linked Cyt c-PEG-FA NPs adjusted to a drug concentration of 100 µg/ml. After 24 h of incubation, the colocalization of DAPI and PI was determined by CLSM. In apoptotic cells, both dyes, PI (red) and DAPI (blue), localized to the nucleus due to the presence of pores in the cell membrane. The nuclei of the permeable LLC apoptotic cells are seen as a bright purple spot in the confocal images due to colocalization of PI and DAPI (Figure 4.5.). PI internalization is representative of highly condensed and fragmented chromatin in apoptotic cells. Thus, the red fluorescence of PI observed in the nucleus of LLC cells with cross-linked Cyt c-PEG-FA NPs confirmed that apoptosis cell death is occurring. In contrast, untreated LLC cells presented no indication of apoptosis, as can be observed by the lack of PI internalization due to the absence of red fluorescence in the confocal images. To evaluate the selectivity of our folate-decorated NPs, we compared the apoptotic cell death of FR-negative NIH/3T3 cells under the same conditions. Confocal images showed a lack of intense PI red fluorescence in the nuclei of NIH/3T3 cells treated

with cross-linked Cyt c-PEG-FA NPs, whereas an enhanced red fluorescence in LLC cells was observed. These results were consistent with the intracellular assay and *in vitro* cell viability results described above, indicating that cross-linked Cyt c-PEG-FA NPs had a significant cytotoxic effect on cancer cells overexpressing FR and not on normal cells.

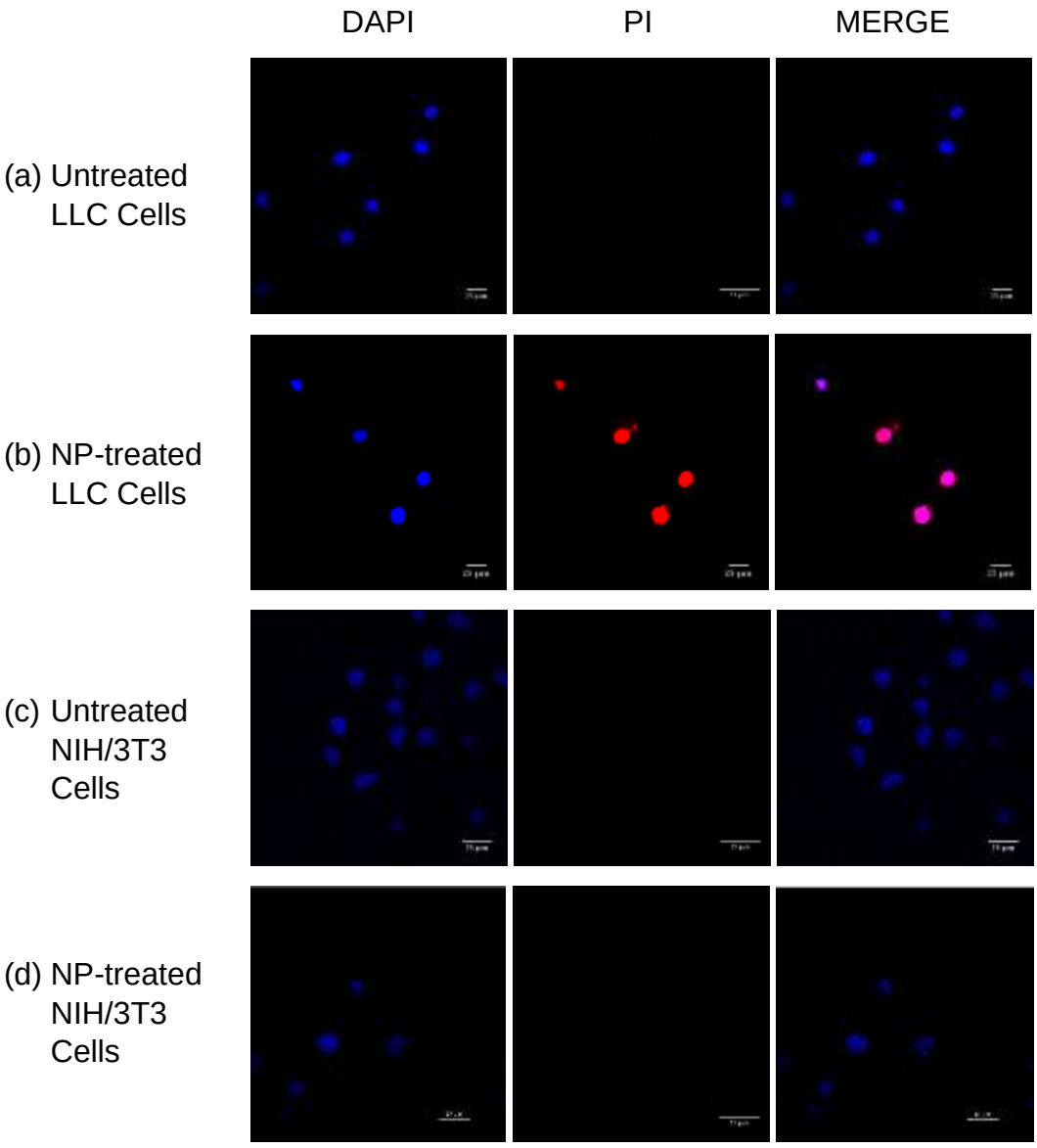

Figure 4.5. Study of DAPI and propidium iodide (PI) colocalization for the detection of apoptotic cells after 24 h of incubation with cross-linked Cyt c-PEG-FA NPs. (b)

Selective induction of apoptosis was observed in LLC cells incubated with NPs. (c) No cellular apoptosis was observed in NIH/3T3 cells when incubated with NPs. (a, d) Untreated LLC and NIH/3T3 cells were used as controls, respectively.

4.2.6. Caspase 3/7 activity

Cyt c-mediated apoptosis of a cell involves the activation of caspase 3/7. Exposure of LLC cells to NPs for 24 h presented a green fluorescence signal induced by the generated caspase 3/7 activity, while the untreated control cells showed a significantly lower fluorescence signal, as observed by confocal imaging (Figure 4.6.a). Quantitative analysis of these images (in 488 nm Ex. channel shown in green) revealed a significant difference (**p=0.003) in non-treated and NP-treated LLC cells (Figure 4.6.b). These results were consistent with the cell-free caspase assay results described on Figure 2, indicating that the cross-linked Cyt c-PEG-FA NPs can substantially increase apoptosis cell death by cellular events and molecular pathways of caspase regulation.

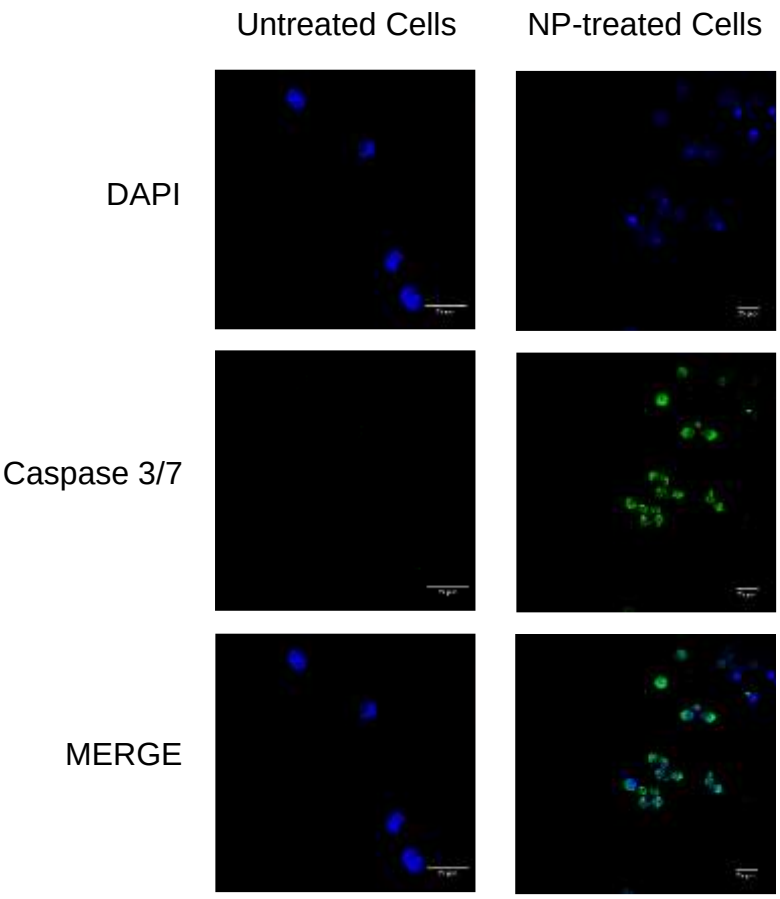

(a)

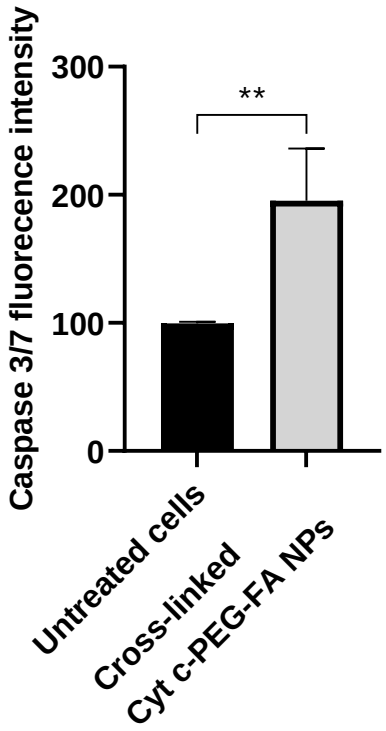

(b)

Figure 4.6. Caspase 3/7 activation in LLC cells after 24 h of incubation with 100 µg/ml of cross-linked Cyt c-PEG-FA NPs. The caspase 3/7 activity was assayed by CellEvent™ caspase 3/7 fluorescent green detection reagent and measured by CLSM. (a) The left panel shows untreated LLC cells used as a negative control to establish the green autofluorescence background, and the right panel shows LLC cells treated with the NPs. Scale bar = 25 µm. (b) Quantitative analysis of green fluorescence (488 nm Ex.) in untreated versus NP-treated cells. The results are expressed as mean ± SD and were significantly different (**, p= 0.003, unpaired t-test analysis, n =3).

4.2.7. Cellular internalization of cross-linked Cyt c-PEG-FA NPs

To investigate the FR-mediated endocytosis mechanism and endosomal escape capability of the cross-linked Cyt c-PEG-FA NPs, FR-positive LLC cells were incubated with FITC-labeled cross-linked Cyt c-PEG-FA NPs and the endosome marker FM-464 for 24 h. Fluorescence intensity of FITC-labeled NPs in LLC cells was observed by Z-stack confocal laser scanning microscopy (CLSM). The confocal Z-stack images obtained from the endosome marker channel showed red fluorescence, while the images of nuclei stained by the DAPI showed blue fluorescence. The green fluorescence observed in the confocal Z-stack images is due to the internalization of the FITC-labeled cross-linked Cyt c-PEG-FA NPs (Figure 4.7.). Yellow fluorescence is due to the colocalization of the two dyes and shows NP entrapment in endosomes [173]. Confocal Z-stack images reveal that FITC-labeled NPs are found in the cytoplasm after 24 h. Furthermore, some of the FITC-labeled NPs were still entrapped in endosomes (yellow spots) in agreement with the expected uptake by endocytosis. These results confirmed the potential of the cross-linked Cyt c-PEG-FA NPs for tumor-targeted drug delivery.

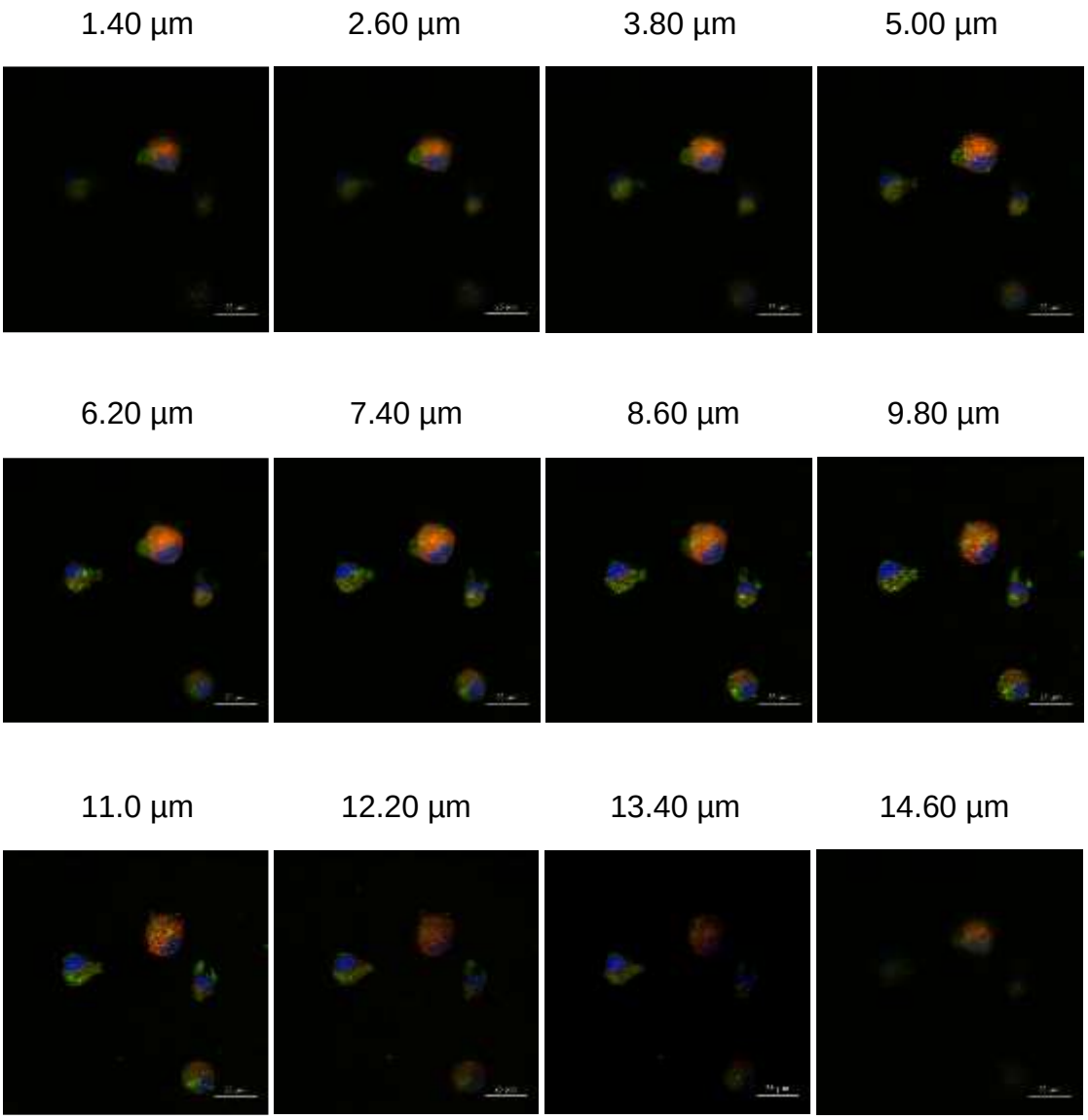

Figure 4.7. Endosomal colocalization of Cyt c-PEG-FA NPs in LLC cells using Z-stack confocal imaging. LLC cells were incubated with FITC-labeled NPs (green fluorescence) at 100 µg/ml concentration and FM-464 endosome marker (red fluorescence) for 24 h. The cell nuclei were stained with DAPI shown in blue. The yellow color indicates the localization of the NPs in the endosomes [1]. Scale bar = 25µm.

The internalization of cross-linked Cyt c-PEG-FA NPs by non-cancer NIH/3T3 cells was also tested to confirm the specificity of our NPs to cells overexpressing folate receptors by confocal microscopy. For this purpose, FR-positive cells (LLC and Hela cells) were compared with the folate-negative NIH/3T3 cell line. Consistent with the NP uptake experiment described above, a significant amount of green fluorescence from FITC-labeled NPs was located in the cytoplasm of the FR-positive cell lines (LLC and HeLa cells), and colocalization with FM-464 (yellow spots) indicates NPs also being present in endosomes (Figure 4.8.). These results indicate that the FITC-labeled NPs escaped from endosomes of the FR-positive cancer cells within 24 h of endocytosis. However, in FR-negative NIH/3T3 cells, NPs remained mainly accumulated extracellularly, and only weak yellow spots were observed in the micrographs, indicating no overlap between FITC-labeled NPs and endosome markers. These results confirm that the level of folate receptors on the cell surface affected the drug internalization. Because of the undetectable level of FR at the normal NIH/3T3 cell surface, the intracellular uptake of the cross-linked Cyt c-PEG-FA NPs decreased, and the intracellular drug release was reduced, which resulted in minimal uptake.

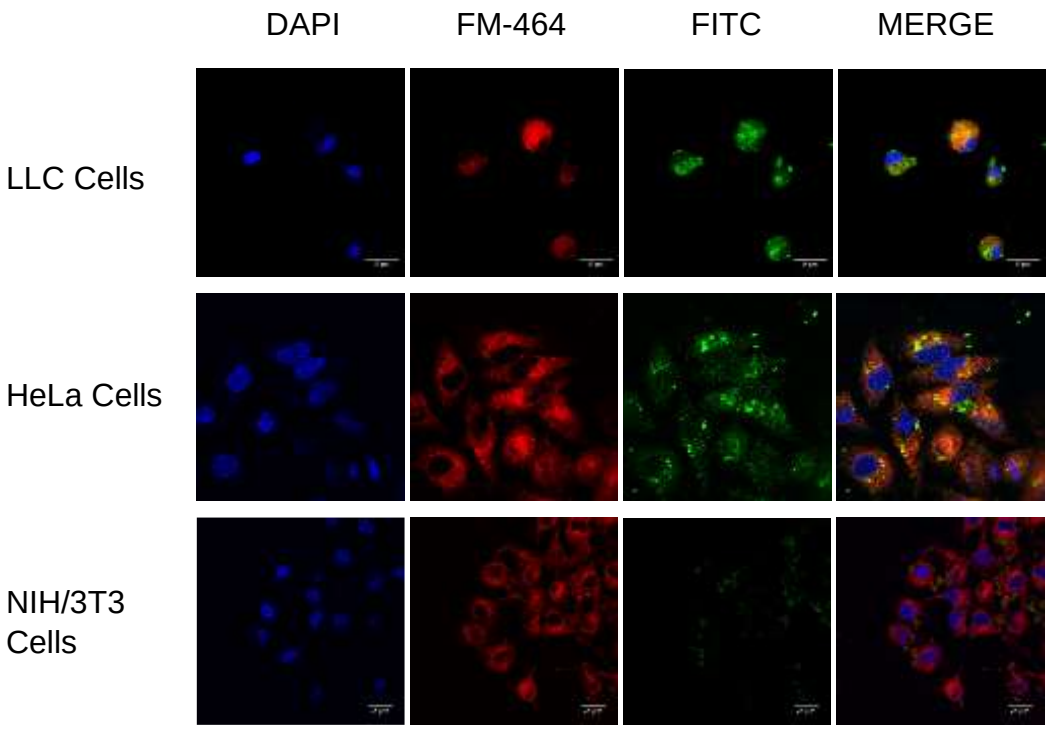

Figure 4.8. Internalization of FITC-labeled cross-linked Cyt c-PEG-FA NPs by FR-positive cancer LLC and HeLa cells and FR-negative non-cancer NIH/3T3 cells. Confocal images of both cells treated with FITC-labeled cross-linked Cyt c-PEG-FA NPs and endosome marker (FM-464) after a 24 h incubation. The yellow color in the merged images indicates the localization of the NPs in the endosomes [1]. Nuclear stain DAPI is shown in blue. Scale bar = 25 μm.

4.2.8. Biodistribution of cross-linked Cyt c-PEG-FA NPs in tumor-bearing mice

For *in vivo* tracking of the NPs distribution, C57BL6J male mice (14-week-old) bearing Lewis lung carcinoma were tail-vein injected with 0.15 mg of NPs labeled with the fluorescent IRDye 680RD (IR-labeled NPs). After 5 min post-injection, tumors, and organs (brain, heart, lungs, spleen, kidneys, liver, and intestines) were quickly extracted and scanned using the LI-COR Odyssey CLx infrared scanner. High-resolution images

showed an enhanced fluorescence signal (64%) from the tumor region of mice injected with IR-labeled NP compared to mice injected with PBS, which was used as a negative control to subtract the fluorescence signal from tumor autofluorescence (Figure 4.9.). Quantitative analysis of fluorescence images of the other tissues, including spleen (98%), heart (66%), and intestines (293%), showed organ deposition of a considerable amount of NPs, whereas fluorescence in the liver (24%) and brain (25%) was minimally detectable. The fluorescence signal recovered from the tumors and organs was presented as a %IR signal of NP-injected tissue over control tissue. Therefore, our results demonstrated successful tumor accumulation of the cross-linked Cyt c-PEG-FA NPs.

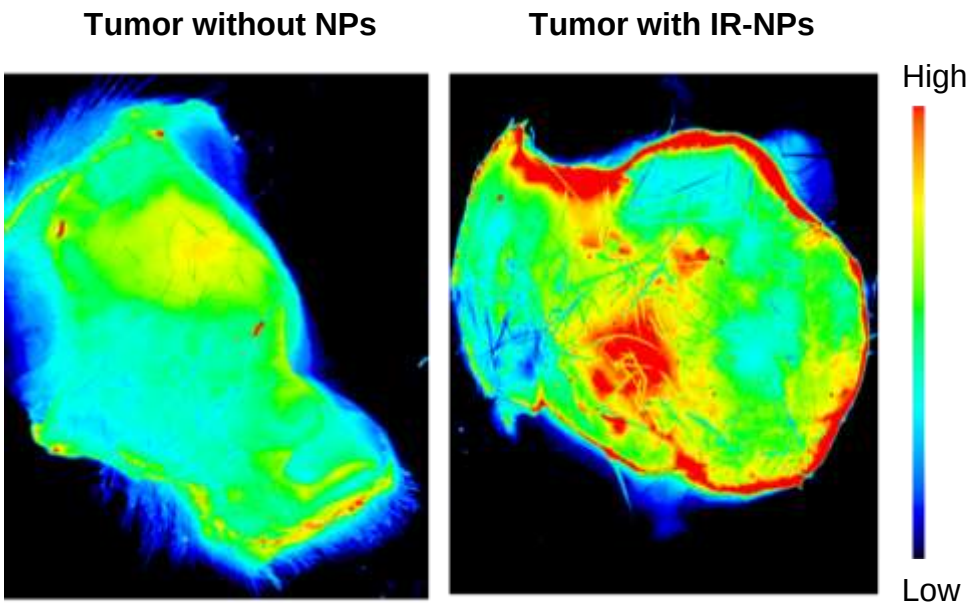

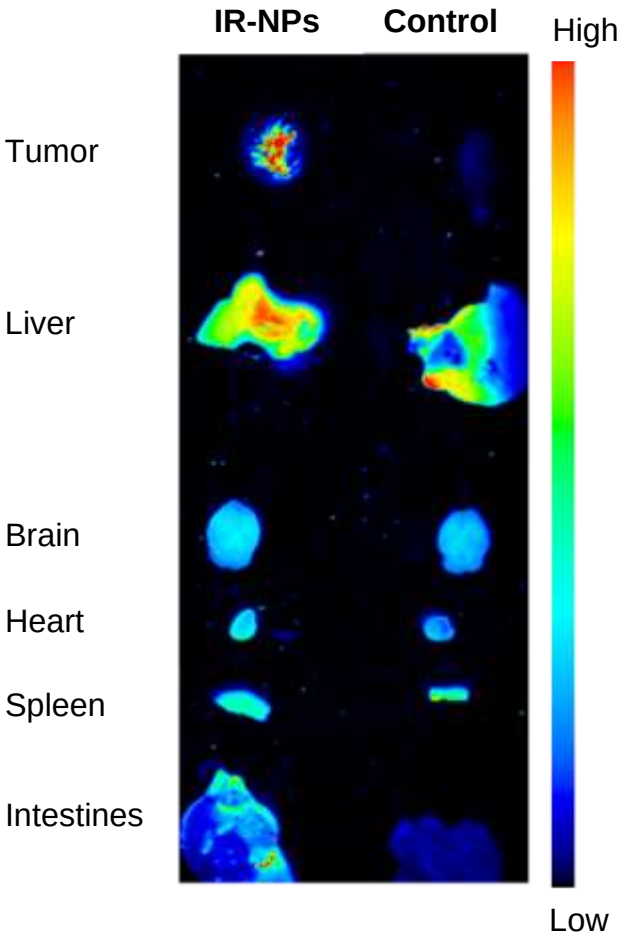

Organs	% IR signal of from IR-control tissue
Tumor	64
Liver	24
Brain	25
Heart	66
Spleen	98
Intestines	293

Figure 4.9. Infrared (IR) signal of organs and tumors after injection of IR-labeled-NPs. Upper panel: A high-resolution image of the ventral side of tumors shows what appears to be NPs in the NP-injected mouse tumor but not in the control mouse. Lower left panel: Five min after tail vein injection of IR-labeled nanoparticles or no nanoparticles into LLC tumor-bearing mice, tumors, and organs were excised and scanned for IR signal at 680 nm (high intensity in red and low in blue) using an infrared scanner (LI-COR). Lower right panel: Percentage of IR signal in the organs of an IR-NP-injected mouse after 5 min compared to control.

4.2.9. Induction of Lewis Lung Carcinoma in Mice to Assess NP Efficacy on Tumor Growth

C57BL/6J mice were implanted with LLC cells to grow a tumor for a total of 12 days. For NP treatment, mice were injected intraperitoneally with 7 mg/kg of cross-linked Cyt c-PEG-FA NPs (169 nm) at day 3 as an early-tumor stage intervention, and at day 8, as a late-stage intervention in tumor growth. Figure 4.10 shows a representative image of the regime used. Tumor volume was measured manually by caliper every 3 days using the length and width of tumors, and the weight was also monitored as a general health measurement. Using an unpaired T-test with a Kolmogorov-Smirnov post-test between the NP-treated and untreated mice showed a significant decrease in tumor size in NP-treated mice ($p= 0.0385$, Figure 4.11.a).

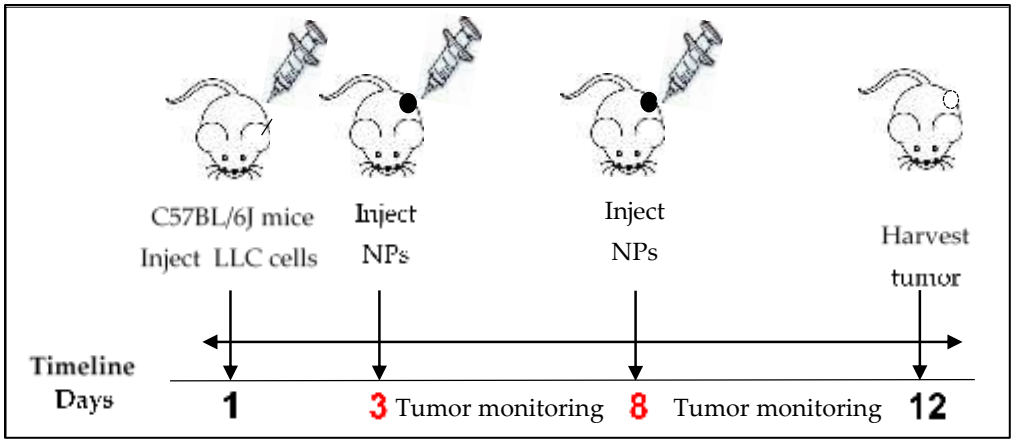

Figure 4.10. Treatment regime in C57BL/6J mice. Male mice (36-60 weeks) were divided into two groups and treated with: 90% PEG 400/10% ethanol vehicle (i.p.) or 7 mg/kg NPs dissolved in vehicle (i.p.) at days 3 and 8 after tumor implant. Tumor monitoring was performed manually by caliper measurement at days 3, 6, 9, and 12, and weight was monitored as a general health measurement in our mouse model.

Our results showed no significant difference in mouse weight between groups (Figure 4.11.b). This underscores the safety and suitability of the cross-linked Cyt c-PEG-FA NPs as a DDS for FR-overexpressing tumor therapy. These results were consistent with the in vitro therapeutic efficiency and the in vivo tumor accumulation of the cross-linked Cyt c-PEG-FA NPs.

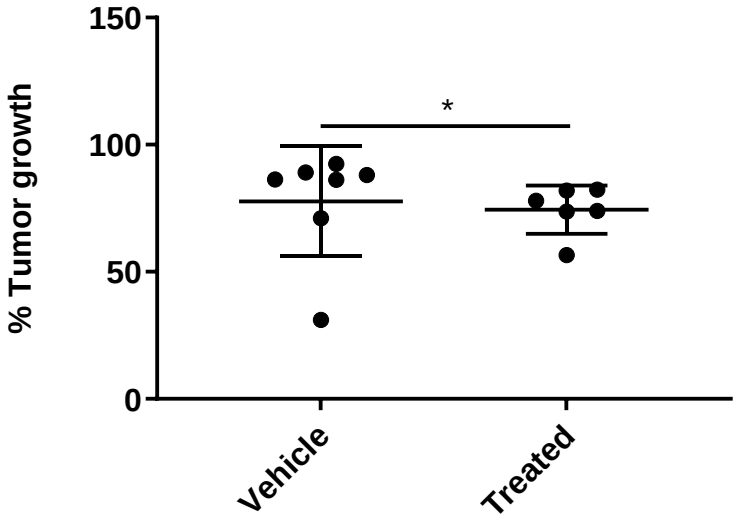

(a)

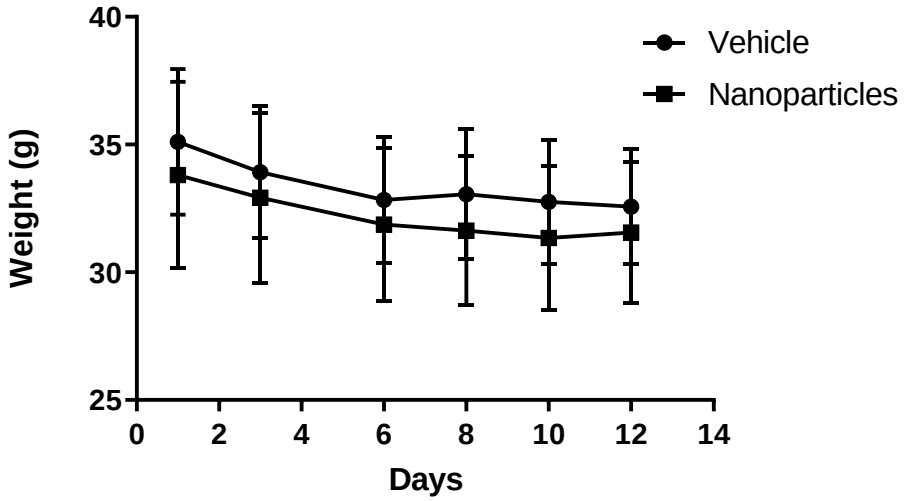

(b)

Figure 4.11. Percentage of tumor growth and mouse weight in NP-treated and untreated mice. (a) Tumor growth monitoring was performed in male mice manually by caliper measurement. (b) Weight was monitored using a rodent balance. T-test and Kolmogorov-Smirnov post-test on percent tumor growth showed *p= 0.0385,

while animal weight was not significantly different between both groups. Vehicle (n=6) and NP-treated (n=7).

4.3. Discussions

Considering the many advantages of protein-based NPs to facilitate their clinical applications and the exemplary success of anticancer NP- based-drug formulations such as Abraxane®, our results show proof-of-concept that cross-linked Cyt c-PEG-FA NPs have the potential to improve tumor-targeting and anti-tumor effects in drug delivery. Our fast infrared NP detection system could be used as a tumor diagnostic agent for folate overexpressing cancers, and further development of the system could have theragnostic potential [174]. Previously, Cyt c NPs stabilized by the hydrophobic polymer poly (lactic-co-glycolic) acid (PLGA) demonstrated that these NPs are an efficient method to induce cell death in lung carcinoma cell culture and bind to the tumor site in the LLC murine model [4]. Recently, we overcame dose limitations previously seen in the PLGA-based NPs for Cyt c by designing smaller Cyt c-based NPs coated with a low molecular weight polymer, FA-PEG. In the current study, Cyt c NPs were stabilized using a thiol-cleavable homo-bifunctional cross-linker that incorporates a triggered release mechanism mediated by the reducing environment inside the cancer cells, without the need for PLGA. This NP formulation showed improved cytotoxicity and biocompatibility compared to previously reported [26]. Besides having an optimal and reduced NP size (~169 nm, compared to the previous system of ~254 nm), this new generation of NPs is more straightforward and economic to prepare, which this is a critical step to develop accesible anticancer drugs. Reviews on NPs have concluded that after many studies on the size, shapes, and surface modifications of NPs, a suitable size for NPs targeting tumors is 100-200 nm. These

particles display increased tumor penetration because they are large enough to avoid being cleared by the kidneys or through vascular extravasation (which eliminates particles of 10-100 nm) [175,176], and they are still large enough to prevent filtration by the kidneys and spleen (300-500 nm) [24]. Our presented NPs size of 169 nm should also improve their tumor passive entry and accumulation due to the enhanced permeability and retention effect (EPR) caused by the unstable tumor vascularization, which leads to a better drug efficacy within the tumor microenvironment [48].

Studies have shown that increasing the flow rate of solvent and non-solvent during the nanoprecipitation process can cause a considerable reduction in the particle size in nanosuspension [177]. Therefore, in these studies, the nanoprecipitation method was optimized by increasing the flow rate of the solvent-displacement process two-fold, resulting in a diameter of 169 nm, a 30% reduction compared to the previous system, and having a positive NP surface charge (+17 mV). For this system, our strategy was to modify the surface of the Cyt c NP with both a redox-responsive homo-bifunctional cross-linker (DSP) and a lower molecular weight polymer (FA-PEG) making it a potential candidate for intravenous (i.v.) administration [48,153]. Whereas the cross-linker shell stabilizes the core of the Cyt c-based NP, the polymer renders in the surface for FR-overexpressing tumor-targeting. The SEM images of the cross-linked Cyt c-PEG-FA NPs showed a spherical shape with narrow size distribution and confirmed the nanometer range of the NP size determined by DLS. Previous limitations of protein delivery systems, including low protein loading and poor protein stability, also improved with the cross-linker.

The DSP is a cell membrane-permeable cross-linker with a disulfide bond that can be reduced in the intracellular environment, preventing the disintegration of the NP in an

aqueous environment [178]. Our *in vitro* drug release results showed an excellent release of around 90% of Cyt c in 2.5 h under reducing intracellular conditions, and exhibited excellent stability under extracellular physiological conditions. However, protein structures can respond to changes in their chemical and physical environment in the NP formulation process [179]. Cyt c as an anticancer drug depends on the mitochondrial apoptosis pathway, which is responsible for the activation of the executioner caspases 3/7 that are known to target various protein substrates leading to cell disassembly and DNA fragmentation [180]. We demonstrated that the cross-linked Cyt c-PEG-FA NPs retained all its enzyme activity (94 ± 8%) through a cell-free caspase 3/7 activation assay, meaning that the integrity of Cyt c after the NP-formulation procedure was not compromised. This result is significant because many of the Cyt c surface lysine residues are known to be involved in the Apaf-1 interaction, essential for the mitochondrial apoptosis pathway [135]. Therefore, we demonstrated that our delivery system displays high stability at physiological conditions and smart-release behavior in a reductive intracellular environment, retaining all their protein bioactivity to interact with the Apaf-1 and activate the apoptosis pathway.

Conventional chemotherapy limitations arise from the lack of specificity and systemic toxicity without discrimination of healthy tissues. Therefore, a cell viability study was conducted to investigate the cytotoxic potential of the cross-linked Cyt c-PEG-FA NPs in lung carcinoma cancer cells. We used the Lewis lung carcinoma (LLC) cell line as the lung carcinoma model because it expresses high levels of FRs, is highly tumorigenic, and is primarily used to evaluate the efficacy of chemotherapeutic agents *in vivo* [181]. For example, the LLC mouse model was a successful *in vivo* preclinical prototype to

assess the drug called Navelbine® before human testing in clinical trials [182]. FR is a well-known tumor marker that binds FA-drug conjugates with high affinity and carries them into the cells via receptor-mediated endocytosis [56]. Compared with normal cells, approximately 40% of human cancer overexpress FR on their surface, but in normal tissue, FR concentration is low [183]. Our *in vitro* cell viability studies demonstrated that the cross-linked Cyt c-PEG-FA NPs are significantly more cytotoxic towards FR-overexpressing cancer cell lines, including human HeLa cancer cells, whereas no significant or minimal cytotoxicity was observed in the non-cancerous NIH/3T3 cell line. In addition, HeLa cell death induced by the NPs demonstrated the translational application of our system to human FR-overexpressing cancers. Thus, the selective cytotoxic efficacy of the cross-linked Cyt c-PEG-FA NPs in FR receptor-overexpressing cancer cells over a FR-negative non-cancer cell line was confirmed.

The cellular apoptotic process induced by Cyt c is one of two apoptotic mechanisms, named 'intrinsic', 'mitochondrial' or 'stress-induced'. In this intrinsic pathway, a sequential protein activation process leads to the release of Cyt c from the mitochondria, which in turn activates caspases 9, 3, 7, that mediate the mechanisms of organized cellular death [184]. Among these processes, we can observe apoptotic cells display characteristic nuclear segmentation and chromatin condensation [185]. For visualization of apoptosis, DAPI and PI colocalization studies have been used to detect apoptotic cells [186]. Our results showed colocalization of DAPI and PI occurred in LLC cells, indicating ongoing late apoptosis, whereas NIH/3T3 cells showed no indication for dye colocalization. These results demonstrated that the cross-linked Cyt c-PEG-FA NPs

induce selective cell death in FR-overexpressing cancer cells without affecting healthy cells, thus confirming the selectivity to cancer cells.

To expand the molecular and cellular mechanism underlying the early apoptotic induction of the NP treatment in LLC cells, we examined fluorescent caspase 3/7 activation in cell culture using confocal microscopy and a cell-free assay. Both methodologies confirmed that the Cyt c protein carried by our targeted-PEGylated NPs effectively initiated tumor cell apoptosis in cancer cells.

Because our NPs are smaller than 500 nm and have an FA ligand attached to their surface, these could be internalized through receptor-mediated clathrin-enabled endocytosis [74]. This internalization mechanism is initiated after a specific ligand-encased nanomaterial binds to a receptor on the surface of the cell membrane. After 24 h of LLC cell incubation with our FITC-labeled cross-linked Cyt c-PEG-FA NPs, the amphiphilic dye FM 464 was used as our endosome marker to confirm the uptake of our NPs in FR-positive cells. Our z-stack confocal microscopy results showed colocalization of FM 464 with our fluorescently-labeled NPs showing a successful uptake.

Further confocal micrograph studies showed significantly higher intracellular uptake of PEG-FA NPs by FR-positive cancer cells (HeLa cells ad LLC) over FR-negative cells (NIH/3T3), indicating that the internalization of these NPs is specific and mediated via an FR-receptor and clathrin-mediated endocytosis mechanism. The internalized FITC-labeled NPs were identified inside the cytoplasm and surrounding the nucleus in the FR-overexpressing cell lines. Overall, our endocytosis results suggest that our NPs have an appropriate size, shape, adequate surface charge, and coating to be efficiently internalized to cancerous cells and could have potential as anticancer nanocarriers [187].

Our *in vivo* studies demonstrate tumor targeting by showing that at 5 min after intravenous injection, the NPs are visible within the tumor. At this early time point, most NPs are still present within organs such as the intestines, spleen, heart, brain, and liver. From our experience with similar NPs, these are later metabolized after 6 h [4]. Nevertheless, further toxicological analyses of the organs at different time points after NP treatment need to be performed to confirm the elimination of this drug.

Our studies determined that the cross-linked Cyt c-PEG-FA NPs were able to reach the tumor, and we further tested the safety and tumor decrease effectivity of these NPs *in vivo*. Results showed that after two doses of NPs at 7 mg/kg in 12 days, compared with the vehicle group (control), mice showed no significant differences in weight; looked groomed, changes in locomotion were not detected, and they showed no evident signs of toxicity throughout the treatment period. These results suggest that the NPs are safe and have low toxicity, which could make their use for future clinical translation possible. Besides their safety, our NPs also significantly decreased the percentage of tumor growth consistently by at least 5%. Future improvement of these NPs formulation, dosage, and combined therapy could increase the treatment's outcome, but it shows promising results as the first *in vivo* proof-of-concept trial. Other FR-targeted DDS loaded with well-known anticancer drugs have shown positive results, decreasing tumor growth *in vivo* [188,189] and reducing their toxic effects by nanoencapsulation. Our approach serves as a platform for the creation of drug delivery systems utilizing different apoptotic-inducing proteins or pharmaceutical proteins for other therapeutic applications.

4.4. Conclusions

In the present work, we report the development of a cross-linked Cyt c-PEG-FA NP drug delivery system that has been designed for FR-mediated targeting and the intracellular redox-sensitive release of the apoptotic protein Cyt c. Our results indicate that our NPs had a significant tumor-growth suppressive effect on cancer cells with FR overexpression *in vitro* and *in vivo*. The *in vitro* results demonstrate that our NPs were adequately sized for tumor targeting, selectively internalized in FR overexpressing cancer cells, and able to induce apoptosis, activating a caspase 3/7 mechanism without affecting normal cells. Indeed, our results strongly suggest that the size of NP plays an important role in the cytotoxic effect compared with our previous Cyt c-based delivery system stabilized by PLGA. Our *in vivo* studies using an immune-competent mouse model of lung carcinoma demonstrated tumor targeting by showing that at 5 min after intravenous injection, the NPs are visible within the tumor. In the same mouse model, our NPs effectively suppressed tumor growth, most probably through the apoptotic activation of caspase 3/7 of tumor cells, without notable side effects. Therefore, these results showcase the potential of our cross-linked Cyt c-based NPs for targeted anticancer therapeutics, avoiding problems associated with many of the common cytotoxic anticancer agents such as unspecific targeting of healthy cells and drug resistance.

5. References

1. Li, W.; Chen, C.; Ye, C.; Wei, T.; Zhao, Y.; Lao, F.; Chen, Z.; Meng, H.; Gao, Y.; Yuan, H. The translocation of fullerenic nanoparticles into lysosome via the pathway of clathrin-mediated endocytosis. *Nanotechnology* **2008**, *19*, 145102, doi:10.1088/0957-4484/19/14/145102

2. Carter, P.J. Introduction to current and future protein therapeutics: a protein engineering perspective. *Experimental cell research* **2011**, *317*, 1261-1269.

3. MaHam, A.; Tang, Z.; Wu, H.; Wang, J.; Lin, Y. Protein-based nanomedicine platforms for drug delivery. *Small* **2009**, *5*, 1706-1721.

4. Barcelo-Bovea, V.; Dominguez-Martinez, I.; Joaquin-Ovalle, F.; Amador, L.A.; Castro-Rivera, E.; Medina-Álvarez, K.; McGoron, A.; Griebenow, K.; Ferrer-Acosta, Y. Optimization and Characterization of Protein Nanoparticles for the Targeted and Smart Delivery of Cytochrome c to Non-Small Cell Lung Carcinoma. *Cancers* **2020**, *12*, 1215, doi:https://doi.org/10.3390/cancers12051215.

5. Chopra, M.; Kaur, P.; Bernela, M.; Thakur, R. Synthesis and optimization of streptomycin loaded chitosan-alginate nanoparticles. *Int. J. Sci. Technol. Res* **2012**, *1*, 31-34.

6. Tarhini, M.; Benlyamani, I.; Hamdani, S.; Agusti, G.; Fessi, H.; Greige-Gerges, H.; Bentaher, A.; Elaissari, A. Protein-based nanoparticle preparation via nanoprecipitation method. *Materials* **2018**, *11*, 394.

7. Siegel, R.L.; Miller, K.D.; Fuchs, H.E.; Jemal, A. Cancer statistics, 2021. *CA: a cancer journal for clinicians* **2021**, *71*, 7-33.

8. Yuan, M.; Huang, L.-L.; Chen, J.-H.; Wu, J.; Xu, Q. The emerging treatment landscape of targeted therapy in non-small-cell lung cancer. *Signal transduction and targeted therapy* **2019**, *4*, 1-14.
9. Halliday, P.R.; Blakely, C.M.; Bivona, T.G. Emerging targeted therapies for the treatment of non-small cell lung cancer. *Current oncology reports* **2019**, *21*, 1-12.
10. Bulbul, A.; Husain, H. First-Line Treatment in EGFR mutant non-small cell lung cancer: is there a best option? *Frontiers in oncology* **2018**, *8*, 94.
11. Gajra, A.; Marr, A.S.; Ganti, A.K. Management of patients with lung cancer and poor performance status. *Journal of the National Comprehensive Cancer Network* **2014**, *12*, 1015-1025.
12. Ramalingam, S.; Belani, C. Systemic chemotherapy for advanced non-small cell lung cancer: recent advances and future directions. *The oncologist* **2008**, *13*, 5-13.
13. Hanna, N.; Johnson, D.; Temin, S.; Baker Jr, S.; Brahmer, J.; Ellis, P.M.; Giaccone, G.; Hesketh, P.J.; Jaiyesimi, I.; Leighl, N.B. Systemic therapy for stage IV non–small-cell lung cancer: American Society of Clinical Oncology clinical practice guideline update. *Journal of Clinical Oncology* **2017**.
14. Kelly, K.; Crowley, J.; Bunn Jr, P.A.; Presant, C.A.; Grevstad, P.K.; Moinpour, C.M.; Ramsey, S.D.; Wozniak, A.J.; Weiss, G.R.; Moore, D.F. Randomized phase III trial of paclitaxel plus carboplatin versus vinorelbine plus cisplatin in the treatment of patients with advanced non–small-cell lung cancer: a Southwest Oncology Group trial. *Journal of Clinical Oncology* **2001**, *19*, 3210-3218.

15. Schiller, J.H.; Harrington, D.; Belani, C.P.; Langer, C.; Sandler, A.; Krook, J.; Zhu, J.; Johnson, D.H. Comparison of four chemotherapy regimens for advanced non–small-cell lung cancer. *New England Journal of Medicine* **2002**, *346*, 92-98.

16. Scagliotti, G.V.; De Marinis, F.; Rinaldi, M.; Crino, L.; Gridelli, C.; Ricci, S.; Matano, E.; Boni, C.; Marangolo, M.; Failla, G. Phase III randomized trial comparing three platinum-based doublets in advanced non-small-cell lung cancer. *Journal of clinical oncology* **2002**, *20*, 4285-4291.

17. Shi, Y.K.; Wang, L.; Han, B.H.e.; Li, W.; Yu, P.; Liu, Y.P.; Ding, C.M.; Song, X.; Ma, Z.Y.; Ren, X.L. First-line icotinib versus cisplatin/pemetrexed plus pemetrexed maintenance therapy for patients with advancedEGFR mutation-positive lung adenocarcinoma (CONVINCE): a phase 3, open-label, randomized study. *Annals of Oncology* **2017**, *28*, 2443-2450.

18. Gridelli, C.; Ardizzoni, A.; Le Chevalier, T.; Manegold, C.; Perrone, F.; Thatcher, N.; Van Zandwijk, N.; Di Maio, M.; Martelli, O.; De Marinis, F. Treatment of advanced non-small-cell lung cancer patients with ECOG performance status 2: results of an European Experts Panel. *Annals of oncology* **2004**, *15*, 419-426.

19. Lemjabbar-Alaoui, H.; Hassan, O.U.I.; Yang, Y.-W.; Buchanan, P. Lung cancer: Biology and treatment options. *Biochimica et Biophysica Acta (BBA)-Reviews on Cancer* **2015**, *1856*, 189-210.

20. Karra, N.; Benita, S. The ligand nanoparticle conjugation approach for targeted cancer therapy. *Current drug metabolism* **2012**, *13*, 22-41.

21. Bae, K.H.; Chung, H.J.; Park, T.G. Nanomaterials for cancer therapy and imaging. *Molecules and cells* **2011**, *31*, 295-302.

22. Dua, K.; Shukla, S.D.; de Jesus Andreoli Pinto, T.; Hansbro, P.M. Nanotechnology: Advancing the translational respiratory research. *Interventional Medicine and Applied Science* **2017**, *9*, 39-41.
23. Allen, T.M.; Cullis, P.R. Drug delivery systems: entering the mainstream. *Science* **2004**, *303*, 1818-1822.
24. Kang, H.; Rho, S.; Stiles, W.R.; Hu, S.; Baek, Y.; Hwang, D.W.; Kashiwagi, S.; Kim, M.S.; Choi, H.S. Size-dependent EPR effect of polymeric nanoparticles on tumor targeting. *Advanced healthcare materials* **2020**, *9*, 1901223.
25. Jain, R.K.; Stylianopoulos, T. Delivering nanomedicine to solid tumors. *Nature reviews Clinical oncology* **2010**, *7*, 653-664.
26. Su, Z.; Dong, S.; Zhao, S.-C.; Liu, K.; Tan, Y.; Jiang, X.; Assaraf, Y.G.; Qin, B.; Chen, Z.-S.; Zou, C. Novel nanomedicines to overcome cancer multidrug resistance. *Drug Resistance Updates* **2021**, *58*, 100777.
27. Alexis, F.; Pridgen, E.M.; Langer, R.; Farokhzad, O.C. Nanoparticle technologies for cancer therapy. *Drug delivery* **2010**, 55-86.
28. Khalid, M.; El-Sawy, H.S. Polymeric nanoparticles: Promising platform for drug delivery. *International journal of pharmaceutics* **2017**, *528*, 675-691.
29. Chauhan, A.S. Dendrimers for drug delivery. *Molecules* **2018**, *23*, 938.
30. Hanafy, N.A.N.; El-Kemary, M.; Leporatti, S. Micelles structure development as a strategy to improve smart cancer therapy. *Cancers* **2018**, *10*, 238.
31. Zhang, X.-y.; Zhang, P.-y. Polymersomes in nanomedicine-A review. *Current Nanoscience* **2017**, *13*, 124-129.

32. Seidi, F.; Jenjob, R.; Crespy, D. Designing smart polymer conjugates for controlled release of payloads. *Chemical reviews* **2018**, *118*, 3965-4036.

33. Shah, S.; Dhawan, V.; Holm, R.; Nagarsenker, M.S.; Perrie, Y. Liposomes: Advancements and innovation in the manufacturing process. *Advanced Drug Delivery Reviews* **2020**.

34. Bayda, S.; Hadla, M.; Palazzolo, S.; Riello, P.; Corona, G.; Toffoli, G.; Rizzolio, F. Inorganic nanoparticles for cancer therapy: a transition from lab to clinic. *Current medicinal chemistry* **2018**, *25*, 4269-4303.

35. Jain, A.; Singh, S.K.; Arya, S.K.; Kundu, S.C.; Kapoor, S. Protein nanoparticles: promising platforms for drug delivery applications. *ACS Biomaterials Science & Engineering* **2018**, *4*, 3939-3961.

36. Cao, Z.; Liu, J. Bacteria and bacterial derivatives as drug carriers for cancer therapy. *Journal of Controlled Release* **2020**, *326*, 396-407.

37. Pugazhendhi, A.; Edison, T.N.J.I.; Karuppusamy, I.; Kathirvel, B. Inorganic nanoparticles: a potential cancer therapy for human welfare. *International journal of pharmaceutics* **2018**, *539*, 104-111.

38. Albanese, A.; Tang, P.S.; Chan, W.C.W. The effect of nanoparticle size, shape, and surface chemistry on biological systems. *Annual review of biomedical engineering* **2012**, *14*, 1-16.

39. García-Fernández, C.; Fornaguera, C.; Borrós, S. Nanomedicine in non-small cell lung cancer: From conventional treatments to immunotherapy. *Cancers* **2020**, *12*, 1609.

40. Liu, J.; Dang, H.; Wang, X.W. The significance of intertumor and intratumor heterogeneity in liver cancer. *Experimental & molecular medicine* **2018**, *50*, e416-e416.

41. Lugano, R.; Ramachandran, M.; Dimberg, A. Tumor angiogenesis: causes, consequences, challenges and opportunities. *Cellular and Molecular Life Sciences* **2020**, *77*, 1745-1770.

42. Wakaskar, R.R. Passive and active targeting in tumor microenvironment. *Int J Drug Dev Res* **2017**, *9*, 37-41.

43. Duncan, R. The dawning era of polymer therapeutics. *Nature reviews Drug discovery* **2003**, *2*, 347-360.

44. Santra, S.; Kaittanis, C.; Perez, J.M. Cytochrome C encapsulating theranostic nanoparticles: a novel bifunctional system for targeted delivery of therapeutic membrane-impermeable proteins to tumors and imaging of cancer therapy. *Molecular pharmaceutics* **2010**, *7*, 1209-1222, doi:https://doi.org/10.1021/mp100043h.

45. Perrault, S.D.; Walkey, C.; Jennings, T.; Fischer, H.C.; Chan, W.C.W. Mediating tumor targeting efficiency of nanoparticles through design. *Nano letters* **2009**, *9*, 1909-1915.

46. Torchilin, V. Tumor delivery of macromolecular drugs based on the EPR effect. *Advanced drug delivery reviews* **2011**, *63*, 131-135.

47. Alexis, F.; Pridgen, E.; Molnar, L.K.; Farokhzad, O.C. Factors affecting the clearance and biodistribution of polymeric nanoparticles. *Molecular pharmaceutics* **2008**, *5*, 505-515.

48. Petros, R.A.; DeSimone, J.M. Strategies in the design of nanoparticles for therapeutic applications. *Nature reviews Drug discovery* **2010**, *9*, 615-627, doi:https://doi.org/10.1038/nrd2591.

49. Owens Iii, D.E.; Peppas, N.A. Opsonization, biodistribution, and pharmacokinetics of polymeric nanoparticles. *International journal of pharmaceutics* **2006**, *307*, 93-102.

50. Zhang, G.; Yang, Z.; Lu, W.; Zhang, R.; Huang, Q.; Tian, M.; Li, L.; Liang, D.; Li, C. Influence of anchoring ligands and particle size on the colloidal stability and in vivo biodistribution of polyethylene glycol-coated gold nanoparticles in tumor-xenografted mice. *Biomaterials* **2009**, *30*, 1928-1936.

51. Gref, R.; Lück, M.; Quellec, P.; Marchand, M.; Dellacherie, E.; Harnisch, S.; Blunk, T.; Müller, R.H. 'Stealth'corona-core nanoparticles surface modified by polyethylene glycol (PEG): influences of the corona (PEG chain length and surface density) and of the core composition on phagocytic uptake and plasma protein adsorption. *Colloids and Surfaces B: Biointerfaces* **2000**, *18*, 301-313.

52. Van Schooneveld, M.M.; Vucic, E.; Koole, R.; Zhou, Y.; Stocks, J.; Cormode, D.P.; Tang, C.Y.; Gordon, R.E.; Nicolay, K.; Meijerink, A. Improved biocompatibility and pharmacokinetics of silica nanoparticles by means of a lipid coating: a multimodality investigation. *Nano letters* **2008**, *8*, 2517-2525.

53. Kobayashi, H.; Watanabe, R.; Choyke, P.L. Improving conventional enhanced permeability and retention (EPR) effects; what is the appropriate target? *Theranostics* **2013**, *4*, 81-89, doi:10.7150/thno.7193.

54. Farran, B.; Pavitra, E.; Kasa, P.; Peela, S.; Raju, G.S.R.; Nagaraju, G.P. Folate-targeted immunotherapies: passive and active strategies for cancer. *Cytokine & growth factor reviews* **2019**, *45*, 45-52.

55. Crider, K.S.; Yang, T.P.; Berry, R.J.; Bailey, L.B. Folate and DNA methylation: a review of molecular mechanisms and the evidence for folate's role. *Advances in nutrition* **2012**, *3*, 21-38, doi:https://doi.org/10.3945/an.111.000992.

56. Low, P.S.; Henne, W.A.; Doorneweerd, D.D. Discovery and development of folic-acid-based receptor targeting for imaging and therapy of cancer and inflammatory diseases. *Accounts of chemical research* **2008**, *41*, 120-129, doi:https://doi.org/10.1021/ar7000815.

57. O'Shannessy, D.J.; Yu, G.; Smale, R.; Fu, Y.-S.; Singhal, S.; Thiel, R.P.; Somers, E.B.; Vachani, A. Folate receptor alpha expression in lung cancer: diagnostic and prognostic significance. *Oncotarget* **2012**, *3*, 414, doi:https://doi.org/10.18632/oncotarget.489.

58. Iwakiri, S.; Sonobe, M.; Nagai, S.; Hirata, T.; Wada, H.; Miyahara, R. Expression status of folate receptor α is significantly correlated with prognosis in non-small-cell lung cancers. *Annals of surgical oncology* **2008**, *15*, 889-899, doi:https://doi.org/10.1245/s10434-007-9755-3.

59. Scaranti, M.; Cojocaru, E.; Banerjee, S.; Banerji, U. Exploiting the folate receptor α in oncology. *Nature Reviews Clinical Oncology* **2020**, *17*, 349-359, doi:https://doi.org/10.1038/s41571-020-0339-5.

60. Shi, H.; Guo, J.; Li, C.; Wang, Z. A current review of folate receptor alpha as a potential tumor target in non-small-cell lung cancer. *Drug design, development and therapy* **2015**, *9*, 4989, doi:https://doi.org/10.2147/DDDT.S90670.

61. Pawar, P.V.; Domb, A.J.; Kumar, N. Systemic targeting systems-EPR effect, ligand targeting systems. In *Focal Controlled Drug Delivery*; Springer: 2014; pp. 61-91.

62. Uthaman, S.; Huh, K.M.; Park, I.-K. Tumor microenvironment-responsive nanoparticles for cancer theragnostic applications. *Biomaterials research* **2018**, *22*, 22.

63. Thamphiwatana, S.; Fu, V.; Zhu, J.; Lu, D.; Gao, W.; Zhang, L. Nanoparticle-stabilized liposomes for pH-responsive gastric drug delivery. *Langmuir* **2013**, *29*, 12228-12233.

64. Raza, A.; Hayat, U.; Rasheed, T.; Bilal, M.; Iqbal, H.M.N. Redox-responsive nano-carriers as tumor-targeted drug delivery systems. *European journal of medicinal chemistry* **2018**, *157*, 705-715.

65. Franco, R.; Cidlowski, J.A. Apoptosis and glutathione: beyond an antioxidant. *Cell Death & Differentiation* **2009**, *16*, 1303-1314.

66. Moghaddam, S.P.H.; Yazdimamaghani, M.; Ghandehari, H. Glutathione-sensitive hollow mesoporous silica nanoparticles for controlled drug delivery. *Journal of controlled release* **2018**, *282*, 62-75.

67. Cheng, R.; Feng, F.; Meng, F.; Deng, C.; Feijen, J.; Zhong, Z. Glutathione-responsive nano-vehicles as a promising platform for targeted intracellular drug and gene delivery. *Journal of controlled release* **2011**, *152*, 2-12.

68. García-Giménez, J.L.; Markovic, J.; Dasí, F.; Queval, G.; Schnaubelt, D.; Foyer, C.H.; Pallardó, F.V. Nuclear glutathione. *Biochimica et Biophysica Acta (BBA)-General Subjects* **2013**, *1830*, 3304-3316.

69. Lee, H.J.; Bae, Y. Cross-linked nanoassemblies from poly (ethylene glycol)-poly (aspartate) block copolymers as stable supramolecular templates for particulate drug delivery. *Biomacromolecules* **2011**, *12*, 2686-2696.

70. Fang, J.; Nakamura, H.; Maeda, H. The EPR effect: Unique features of tumor blood vessels for drug delivery, factors involved, and limitations and augmentation of the effect. *Advanced Drug Delivery Reviews* **2011**, *63*, 136-151, doi:https://doi.org/10.1016/j.addr.2010.04.009.

71. Mattson, G.; Conklin, E.; Desai, S.; Nielander, G.; Savage, M.D.; Morgensen, S. A practical approach to crosslinking. *Molecular biology reports* **1993**, *17*, 167-183.

72. Hermanson, G.T. *Bioconjugate techniques*; Academic press: 2013.

73. Karimi, M.; Ghasemi, A.; Zangabad, P.S.; Rahighi, R.; Basri, S.M.M.; Mirshekari, H.; Amiri, M.; Pishabad, Z.S.; Aslani, A.; Bozorgomid, M. Smart micro/nanoparticles in stimulus-responsive drug/gene delivery systems. *Chemical Society Reviews* **2016**, *45*, 1457-1501.

74. Lohcharoenkal, W.; Wang, L.; Chen, Y.C.; Rojanasakul, Y. Protein nanoparticles as drug delivery carriers for cancer therapy. *BioMed research international* **2014**, *2014*.

75. Seaberg, J.; Flynn, N.; Cai, A.; Ramsey, J.D. Effect of redox-responsive DTSSP crosslinking on poly (l-lysine)-grafted-poly (ethylene glycol) nanoparticles for delivery of proteins. *Biotechnology and Bioengineering* **2020**, *117*, 2504-2515.

76. Tarhini, M.; Greige-Gerges, H.; Elaissari, A. Protein-based nanoparticles: From preparation to encapsulation of active molecules. *International journal of pharmaceutics* **2017**, *522*, 172-197.

77. Sanchez-Garcia, L.; Martín, L.; Mangues, R.; Ferrer-Miralles, N.; Vázquez, E.; Villaverde, A. Recombinant pharmaceuticals from microbial cells: a 2015 update. *Microbial cell factories* **2016**, *15*, 1-7.

78. Walsh, G. Biopharmaceutical benchmarks 2018. *Nature biotechnology* **2018**, *36*, 1136-1145.

79. Leader, B.; Baca, Q.J.; Golan, D.E. Protein therapeutics: a summary and pharmacological classification. *Nature reviews Drug discovery* **2008**, *7*, 21-39.

80. Dimitrov, D.S. Therapeutic proteins. *Therapeutic Proteins* **2012**, 1-26.

81. Ferrara, N.; Hillan, K.J.; Gerber, H.-P.; Novotny, W. Discovery and development of bevacizumab, an anti-VEGF antibody for treating cancer. *Nature reviews Drug discovery* **2004**, *3*, 391-400.

82. Saltz, L.B.; Meropol, N.J.; Loehrer Sr, P.J.; Needle, M.N.; Kopit, J.; Mayer, R.J. Phase II trial of cetuximab in patients with refractory colorectal cancer that expresses the epidermal growth factor receptor. *Journal of clinical oncology* **2004**, *22*, 1201-1208.

83. Wainberg, Z.; Hecht, J.R. A phase III randomized, open-label, controlled trial of chemotherapy and bevacizumab with or without panitumumab in the first-line

treatment of patients with metastatic colorectal cancer. *Clinical colorectal cancer* **2006**, *5*, 363-367.

84. Keating, M.J.; Flinn, I.; Jain, V.; Binet, J.-L.; Hillmen, P.; Byrd, J.; Albitar, M.; Brettman, L.; Santabarbara, P.; Wacker, B. Therapeutic role of alemtuzumab (Campath-1H) in patients who have failed fludarabine: results of a large international study. *Blood, The Journal of the American Society of Hematology* **2002**, *99*, 3554-3561.

85. Keating, M.J.; O'Brien, S.; Albitar, M.; Lerner, S.; Plunkett, W.; Giles, F.; Andreeff, M.; Cortes, J.; Faderl, S.; Thomas, D. Early results of a chemoimmunotherapy regimen of fludarabine, cyclophosphamide, and rituximab as initial therapy for chronic lymphocytic leukemia. *Journal of clinical oncology* **2005**, *23*, 4079-4088.

86. Vogel, C.L.; Cobleigh, M.A.; Tripathy, D.; Gutheil, J.C.; Harris, L.N.; Fehrenbacher, L.; Slamon, D.J.; Murphy, M.; Novotny, W.F.; Burchmore, M. Efficacy and safety of trastuzumab as a single agent in first-line treatment of HER2-overexpressing metastatic breast cancer. *Journal of clinical oncology* **2002**, *20*, 719-726.

87. Scott, A.M.; Wolchok, J.D.; Old, L.J. Antibody therapy of cancer. *Nature reviews cancer* **2012**, *12*, 278-287.

88. Shlyakhovenko, V.O. Ribonucleases. Possible new approach in cancer therapy. *Experimental oncology* **2016**, 2-8.

89. Tse, E.; Rabbitts, T.H. Intracellular antibody-caspase-mediated cell killing: an approach for application in cancer therapy. *Proceedings of the National Academy of Sciences* **2000**, *97*, 12266-12271.

90. Morales-Cruz, M.; Figueroa, C.M.; González-Robles, T.; Delgado, Y.; Molina, A.; Méndez, J.; Morales, M.; Griebenow, K. Activation of caspase-dependent apoptosis by intracellular delivery of cytochrome c-based nanoparticles. *Journal of nanobiotechnology* **2014**, *12*, 1-11.

91. Yamabe, K.; Shimizu, S.; Ito, T.; Yoshioka, Y.; Nomura, M.; Narita, M.; Saito, I.; Kanegae, Y.; Matsuda, H. Cancer gene therapy using a pro-apoptotic gene, caspase-3. *Gene therapy* **1999**, *6*, 1952-1959.

92. Delinois, L.J.; León-Vélez, D.; Vázquez-Medina, A.; Vélez-Cabrera, A.; Marrero-Sánchez, A.; Nieves-Escobar, C.; Alfonso-Cano, D.; Caraballo-Rodríguez, D.; Rodriguez-Ortiz, J.; Acosta-Mercado, J. Cytochrome c: Using Biological Insight toward Engineering an Optimized Anticancer Biodrug. *Inorganics* **2021**, *9*, 83.

93. Hawkins, M.J.; Soon-Shiong, P.; Desai, N. Protein nanoparticles as drug carriers in clinical medicine. *Advanced drug delivery reviews* **2008**, *60*, 876-885.

94. Ozaki, T.; Nakagawara, A. Role of p53 in cell death and human cancers. *Cancers* **2011**, *3*, 994-1013.

95. Ahrendt, S.A.; Hu, Y.; Buta, M.; McDermott, M.P.; Benoit, N.; Yang, S.C.; Wu, L.; Sidransky, D. p53 mutations and survival in stage I non-small-cell lung cancer: results of a prospective study. *Journal of the National Cancer Institute* **2003**, *95*, 961-970.

96. Ryan, K.M.; Phillips, A.C.; Vousden, K.H. Regulation and function of the p53 tumor suppressor protein. *Current opinion in cell biology* **2001**, *13*, 332-337, doi:https://doi.org/10.1016/S0955-0674(00)00216-7.

97. Park, J.H.; Park, S.A.; Lee, Y.J.; Park, H.W.; Oh, S.M. PBK attenuates paclitaxel-induced autophagic cell death by suppressing p53 in H460 non-small-cell lung cancer cells. *FEBS Open bio* **2020**, *10*, 937-950.

98. Desilet, N.; Campbell, T.N.; Choy, F.Y.M. p53-based anti-cancer therapies: an empty promise? *Current issues in molecular biology* **2010**, *12*, 143-146.

99. Margoliash, E. Primary structure and evolution of cytochrome c. *Proceedings of the National Academy of Sciences of the United States of America* **1963**, *50*, 672.

100. Ow, Y.-L.P.; Green, D.R.; Hao, Z.; Mak, T.W. Cytochrome c: functions beyond respiration. *Nature reviews Molecular cell biology* **2008**, *9*, 532-542.

101. Raina, M.; Ibba, M. tRNAs as regulators of biological processes. *Frontiers in genetics* **2014**, *5*, 171.

102. Méndez, J.; Morales Cruz, M.; Delgado, Y.; Figueroa, C.M.; Orellano, E.A.; Morales, M.; Monteagudo, A.; Griebenow, K. Delivery of Chemically Glycosylated Cytochrome c Immobilized in Mesoporous Silica Nanoparticles Induces Apoptosis in HeLa Cancer Cells. *Molecular Pharmaceutics* **2014**, *11*, 102-111, doi:10.1021/mp400400j.

103. Kim, S.K.; Foote, M.B.; Huang, L. The targeted intracellular delivery of cytochrome C protein to tumors using lipid-apolipoprotein nanoparticles. *Biomaterials* **2012**, *33*, 3959-3966.

104. Kintzing, J.R.; Interrante, M.V.F.; Cochran, J.R. Emerging strategies for developing next-generation protein therapeutics for cancer treatment. *Trends in pharmacological sciences* **2016**, *37*, 993-1008.

105. Bajracharya, R.; Song, J.G.; Back, S.Y.; Han, H.-K. Recent advancements in non-invasive formulations for protein drug delivery. *Computational and structural biotechnology journal* **2019**, *17*, 1290-1308.

106. Gu, Z.; Biswas, A.; Zhao, M.; Tang, Y. Tailoring nanocarriers for intracellular protein delivery. *Chemical Society Reviews* **2011**, *40*, 3638-3655.

107. Kam, N.W.S.; Dai, H. Carbon nanotubes as intracellular protein transporters: generality and biological functionality. *Journal of the American Chemical Society* **2005**, *127*, 6021-6026.

108. Slowing, I.I.; Trewyn, B.G.; Lin, V.S.Y. Mesoporous silica nanoparticles for intracellular delivery of membrane-impermeable proteins. *Journal of the American Chemical Society* **2007**, *129*, 8845-8849.

109. Yang, X.; Zhao, C.; Ju, E.; Ren, J.; Qu, X. Contrasting modulation of enzyme activity exhibited by graphene oxide and reduced graphene. *Chemical Communications* **2013**, *49*, 8611-8613.

110. Koo, A.N.; Min, K.H.; Lee, H.J.; Jegal, J.H.; Lee, J.W.; Lee, S.C. Calcium carbonate mineralized nanoparticles as an intracellular transporter of cytochrome c for cancer therapy. *Chemistry–An Asian Journal* **2015**, *10*, 2380-2387.

111. Dutta, K.; Hu, D.; Zhao, B.; Ribbe, A.E.; Zhuang, J.; Thayumanavan, S. Templated self-assembly of a covalent polymer network for intracellular protein

delivery and traceless release. *Journal of the American Chemical Society* **2017**, *139*, 5676-5679.

112. Li, S.; Zhang, J.; Deng, C.; Meng, F.; Yu, L.; Zhong, Z. Redox-sensitive and intrinsically fluorescent photoclick hyaluronic acid nanogels for traceable and targeted delivery of cytochrome c to breast tumor in mice. *ACS applied materials & interfaces* **2016**, *8*, 21155-21162.

113. Saxena, M.; Delgado, Y.; Sharma, R.K.; Sharma, S.; Guzmán, S.L.P.D.L.; Tinoco, A.D.; Griebenow, K. Inducing cell death in vitro in cancer cells by targeted delivery of cytochrome c via a transferrin conjugate. *PLoS One* **2018**, *13*, e0195542.

114. Morales-Cruz, M.; Cruz-Montañez, A.; Figueroa, C.M.; González-Robles, T.; Davila, J.; Inyushin, M.; Loza-Rosas, S.A.; Molina, A.M.; Muñoz-Perez, L.; Kucheryavykh, L.Y. Combining stimulus-triggered release and active targeting strategies improves cytotoxicity of cytochrome c nanoparticles in tumor cells. *Molecular pharmaceutics* **2016**, *13*, 2844-2854, doi:https://doi.org/10.1021/acs.molpharmaceut.6b00461.

115. Miladi, K.; Ibraheem, D.; Iqbal, M.; Sfar, S.; Fessi, H.; Elaissari, A. Particles from preformed polymers as carriers for drug delivery. *EXCLI journal* **2014**, *13*, 28.

116. Joye, I.J.; McClements, D.J. Production of nanoparticles by anti-solvent precipitation for use in food systems. *Trends in Food Science & Technology* **2013**, *34*, 109-123.

117. Morales-Cruz, M.; Flores-Fernández, G.M.; Morales-Cruz, M.; Orellano, E.A.; Rodriguez-Martinez, J.A.; Ruiz, M.; Griebenow, K. Two-step nanoprecipitation for

the production of protein-loaded PLGA nanospheres. *Results in pharma sciences* **2012**, *2*, 79-85.

118. Caesar, C.E.B.; Esbjörner, E.K.; Lincoln, P.; Nordén, B. Assigning membrane binding geometry of cytochrome c by polarized light spectroscopy. *Biophysical journal* **2009**, *96*, 3399-3411, doi:https://doi.org/10.1016/j.bpj.2009.01.025.

119. Gaucher, C.; Boudier, A.; Bonetti, J.; Clarot, I.; Leroy, P.; Parent, M. Glutathione: antioxidant properties dedicated to nanotechnologies. *Antioxidants* **2018**, *7*, 62, doi:https://doi.org/10.3390/antiox7050062.

120. Morgensztern, D.; Ng, S.H.; Gao, F.; Govindan, R. Trends in stage distribution for patients with non-small cell lung cancer: a National Cancer Database survey. *Journal of thoracic oncology* **2010**, *5*, 29-33, doi:https://doi.org/10.1097/JTO.0b013e3181c5920c.

121. Wang, S.; Lai, X.; Deng, Y.; Song, Y. Correlation between mouse age and human age in anti-tumor research: Significance and method establishment. *Life sciences* **2020**, *242*, 117242, doi:https://doi.org/10.1016/j.lfs.2019.117242.

122. Talbot, S.R.; Biernot, S.; Bleich, A.; van Dijk, R.M.; Ernst, L.; Häger, C.; Helgers, S.O.A.; Koegel, B.; Koska, I.; Kuhla, A. Defining body-weight reduction as a humane endpoint: a critical appraisal. *Laboratory animals* **2020**, *54*, 99-110, doi:https://doi.org/10.1177/0023677219883319.

123. Yadav, N.; Gogada, R.; O'Malley, J.; Gundampati, R.K.; Jayanthi, S.; Hashmi, S.; Lella, R.; Zhang, D.; Wang, J.; Kumar, R. Molecular insights on cytochrome c and nucleotide regulation of apoptosome function and its implication in cancer.

Biochimica et Biophysica Acta (BBA)-Molecular Cell Research **2020**, *1867*, 118573, doi:https://doi.org/10.1016/j.bbamcr.2019.118573.

124. Brown, L.R. Commercial challenges of protein drug delivery. *Expert opinion on drug delivery* **2005**, *2*, 29-42.

125. Mehtani, D.; Seth, A.; Sharma, P.; Maheshwari, N.; Kapoor, D.; Shrivastava, S.K.; Tekade, R.K. Biomaterials for sustained and controlled delivery of small drug molecules. In *Biomaterials and bionanotechnology*; Elsevier: 2019; pp. 89-152.

126. Amighi, F.; Emam-Djomeh, Z.; Labbafi-Mazraeh-Shahi, M. Effect of different cross-linking agents on the preparation of bovine serum albumin nanoparticles. *Journal of the Iranian Chemical Society* **2020**, *17*, 1223-1235.

127. Raja, M.M.; Lim, P.Q.; Wong, Y.S.; Xiong, G.M.; Zhang, Y.; Venkatraman, S.; Huang, Y. Polymeric nanomaterials: methods of preparation and characterization. In *Nanocarriers for drug delivery*; Elsevier: 2019; pp. 557-653.

128. Blanco, E.; Shen, H.; Ferrari, M. Principles of nanoparticle design for overcoming biological barriers to drug delivery. *Nature biotechnology* **2015**, *33*, 941-951.

129. Geng, Y.A.N.; Dalhaimer, P.; Cai, S.; Tsai, R.; Tewari, M.; Minko, T.; Discher, D.E. Shape effects of filaments versus spherical particles in flow and drug delivery. *Nature nanotechnology* **2007**, *2*, 249-255.

130. Danaei, M.; Dehghankhold, M.; Ataei, S.; Hasanzadeh Davarani, F.; Javanmard, R.; Dokhani, A.; Khorasani, S.; Mozafari, M.R. Impact of particle size and polydispersity index on the clinical applications of lipidic nanocarrier systems. *Pharmaceutics* **2018**, *10*, 57.

131. Saikia, C.; Das, M.K.; Ramteke, A.; Maji, T.K. Effect of crosslinker on drug delivery properties of curcumin loaded starch coated iron oxide nanoparticles. *International journal of biological macromolecules* **2016**, *93*, 1121-1132.

132. Liu, W.F.; Guo, Z.X.; Yu, J. Preparation of crosslinked composite nanoparticles. *Journal of applied polymer science* **2005**, *97*, 1538-1544.

133. Koebe, M.; Drechsler, M.; Weber, J.; Yuan, J. Crosslinked poly (ionic liquid) nanoparticles: inner structure, size, and morphology. *Macromolecular rapid communications* **2012**, *33*, 646-651.

134. Khatami, M.; Alijani, H.Q.; Sharifi, I. Biosynthesis of bimetallic and core–shell nanoparticles: their biomedical applications–a review. *IET nanobiotechnology* **2018**, *12*, 879-887.

135. Yu, T.; Wang, X.; Purring-Koch, C.; Wei, Y.; McLendon, G.L. A mutational epitope for cytochrome C binding to the apoptosis protease activation factor-1. *Journal of Biological Chemistry* **2001**, *276*, 13034-13038, doi:https://doi.org/10.1074/jbc.M009773200

136. Rondon, A.; Mahri, S.; Morales-Yanez, F.; Dumoulin, M.; Vanbever, R. Protein Engineering Strategies for Improved Pharmacokinetics. *Advanced Functional Materials* **2021**, *31*, 2101633.

137. Langer, K.; Balthasar, S.; Vogel, V.; Dinauer, N.; Von Briesen, H.; Schubert, D. Optimization of the preparation process for human serum albumin (HSA) nanoparticles. *International journal of pharmaceutics* **2003**, *257*, 169-180.

138. Kucheryavykh, Y.V.; Davila, J.; Ortiz-Rivera, J.; Inyushin, M.; Almodovar, L.; Mayol, M.; Morales-Cruz, M.; Cruz-Montañez, A.; Barcelo-Bovea, V.; Griebenow, K. Targeted delivery of nanoparticulate Cytochrome C into glioma cells through the proton-coupled folate transporter. *Biomolecules* **2019**, *9*, 154.

139. Gatoo, M.A.; Naseem, S.; Arfat, M.Y.; Mahmood Dar, A.; Qasim, K.; Zubair, S. Physicochemical Properties of Nanomaterials: Implication in Associated Toxic Manifestations. *BioMed Research International* **2014**, *2014*, 498420, doi:10.1155/2014/498420.

140. Khan, S.A.; Schneider, M. Nanoprecipitation versus two step desolvation technique for the preparation of gelatin nanoparticles. 2013; pp. 76-81.

141. Shen, C.; Pan, Y.; Wu, D.; Liu, Y.; Ma, C.; Li, F.; Ma, H.; Zhang, Y. A crosslinking-induced precipitation process for the simultaneous removal of poly (vinyl alcohol) and reactive dye: the importance of covalent bond forming and magnesium coagulation. *Chemical Engineering Journal* **2019**, *374*, 904-913.

142. Fröhlich, T.; Edinger, D.; Russ, V.; Wagner, E. Stabilization of polyplexes via polymer crosslinking for efficient siRNA delivery. *European Journal of Pharmaceutical Sciences* **2012**, *47*, 914-920, doi:https://doi.org/10.1016/j.ejps.2012.09.006.

143. Joseph, E.; Singhvi, G. Multifunctional nanocrystals for cancer therapy: a potential nanocarrier. *Nanomaterials for drug delivery and therapy* **2019**, 91-116.

144. Abrams, D.; Huang, Y.; McQuarrie, S.; Roa, W.; Chen, H.; Löbenberg, R.; Azarmi, S.; Miller, G.G.; Finlay, W.H. Optimization of a two-step desolvation

method for preparing gelatin nanoparticles and cell uptake studies in 143B osteosarcoma cancer cells. **2006**.

145. Taheri Qazvini, N.; Zinatloo, S. Synthesis and characterization of gelatin nanoparticles using CDI/NHS as a non-toxic cross-linking system. *Journal of Materials Science: Materials in Medicine* **2011**, *22*, 63-69.

146. D'Addio, S.M.; Prud'homme, R.K. Controlling drug nanoparticle formation by rapid precipitation. *Advanced drug delivery reviews* **2011**, *63*, 417-426.

147. Jahanshahi, M.; Babaei, Z. Protein nanoparticle: a unique system as drug delivery vehicles. *African journal of Biotechnology* **2008**, *7*.

148. Baseer, A.; Koenneke, A.; Zapp, J.; Khan, S.A.; Schneider, M. Design and Characterization of Surface-Crosslinked Gelatin Nanoparticles for the Delivery of Hydrophilic Macromolecular Drugs. *Macromolecular Chemistry and Physics* **2019**, *220*, 1900260.

149. Figueroa, C.M.; Suárez, B.N.; Molina, A.M.; Fernández, J.C.; Torres, Z.; Griebenow, K. Smart release nano-formulation of cytochrome C and hyaluronic acid induces apoptosis in cancer cells. *Journal of nanomedicine & nanotechnology* **2017**, *8*.

150. de Oliveira Cardoso, V.M.; Evangelista, R.C.; Gremião, M.P.D.; Cury, B.S.F. Insights into the impact of cross-linking processes on physicochemical characteristics and mucoadhesive potential of gellan gum/retrograded starch microparticles as a platform for colonic drug release. *Journal of Drug Delivery Science and Technology* **2020**, *55*, 101445.

151. Wang, Y.; Tan, Y. Enhanced drug loading capacity of 10-hydroxycamptothecin-loaded nanoparticles prepared by two-step nanoprecipitation method. *Journal of Drug Delivery Science and Technology* **2016**, *36*, 183-191.

152. Zappa, C.; Mousa, S.A. Non-small cell lung cancer: current treatment and future advances. *Transl Lung Cancer Res* **2016**, *5*, 288-300, doi:10.21037/tlcr.2016.06.07.

153. Senapati, S.; Mahanta, A.K.; Kumar, S.; Maiti, P. Controlled drug delivery vehicles for cancer treatment and their performance. *Signal transduction and targeted therapy* **2018**, *3*, 1-19, doi:https://doi.org/10.1038/s41392-017-0004-3.

154. Duarte, M.L.; de Moraes, E.; Pontes, E.; Schluckebier, L.; de Moraes, J.L.; Hainaut, P.; Ferreira, C.G. Role of p53 in the induction of cyclooxygenase-2 by cisplatin or paclitaxel in non-small cell lung cancer cell lines. *Cancer letters* **2009**, *279*, 57-64.

155. Fregoni, M.M.; Nelli, F.; Riccardi, F.; di Isernia, G.; Costanzo, R.; Rocco, G.; Daniele, G.; Signoriello, S.; Piccirillo, M.C.; Gallo, C. Cisplatin-Based First-Line Treatment of Elderly Patients With Advanced Non–Small-Cell Lung Cancer: Joint Analysis of MILES-3 and MILES-4 Phase III Trials. **2018**, doi:10.1200/JCO.2017.76.8390.

156. Aubrey, B.J.; Kelly, G.L.; Janic, A.; Herold, M.J.; Strasser, A. How does p53 induce apoptosis and how does this relate to p53-mediated tumour suppression? *Cell Death & Differentiation* **2018**, *25*, 104-113, doi:https://doi.org/10.1038/cdd.2017.169.

157. Greulich, H. The genomics of lung adenocarcinoma: opportunities for targeted therapies. *Genes & cancer* **2010**, *1*, 1200-1210, doi:https://doi.org/10.1177/1947601911407324.

158. Vazquez, A.; Bond, E.E.; Levine, A.J.; Bond, G.L. The genetics of the p53 pathway, apoptosis and cancer therapy. *Nature reviews Drug discovery* **2008**, *7*, 979-987, doi:https://doi.org/10.1038/nrd2656.

159. Baig, S.; Seevasant, I.; Mohamad, J.; Mukheem, A.; Huri, H.Z.; Kamarul, T. Potential of apoptotic pathway-targeted cancer therapeutic research: Where do we stand? *Cell death & disease* **2016**, *7*, e2058-e2058, doi:https://doi.org/10.1038/cddis.2015.275.

160. Serna, N.; Sánchez-García, L.; Unzueta, U.; Díaz, R.; Vázquez, E.; Mangues, R.; Villaverde, A. Protein-based therapeutic killing for cancer therapies. *Trends in biotechnology* **2018**, *36*, 318-335.

161. Yamada, Y.; Harashima, H. Mitochondrial drug delivery systems for macromolecule and their therapeutic application to mitochondrial diseases. *Adv Drug Deliv Rev* **2008**, *60*, 1439-1462, doi:10.1016/j.addr.2008.04.016.

162. Yadav, N.; Gogada, R.; O'Malley, J.; Gundampati, R.K.; Jayanthi, S.; Hashmi, S.; Lella, R.; Zhang, D.; Wang, J.; Kumar, R.; et al. Molecular insights on cytochrome c and nucleotide regulation of apoptosome function and its implication in cancer. *Biochim Biophys Acta Mol Cell Res* **2020**, *1867*, 118573, doi:10.1016/j.bbamcr.2019.118573.

163. Alkhuriji, A.F.; Alsaiari, S.G.; Alomar, S.Y.; Alnafjan, A.A.; Alobaid, H.; El-Khadragy, M.F. Effect of mesenchymal stem cells on cytochrome-c release and

inflammation in colon cancer induced by 1, 2-dimethylhydrazine in Wistar albino rats. *Bioscience Reports* **2021**, *41*, BSR20204356, doi:https://doi.org/10.1042/BSR20204356.

164. Hanahan, D.; Weinberg, R.A. The hallmarks of cancer. *cell* **2000**, *100*, 57-70, doi:https://doi.org/10.1016/S0092-8674(00)81683-9.

165. Suk, J.S.; Xu, Q.; Kim, N.; Hanes, J.; Ensign, L.M. PEGylation as a strategy for improving nanoparticle-based drug and gene delivery. *Advanced drug delivery reviews* **2016**, *99*, 28-51, doi:https://doi.org/10.1016/j.addr.2015.09.012.

166. Geng, Y., Dalhaimer, P., Cai, S., Tsai, R., Tewari, M., Minko, T., & Discher, D. E. . Shape effects of filaments versus spherical particles in flow and drug delivery. *Nature nanotechnology* **2007**, *2*, 249-255, doi:https://doi.org/10.1038/nnano.2007.70

167. Alves, I.D.; Jiao, C.Y.; Aubry, S.; Aussedat, B.; Burlina, F.; Chassaing, G.; Sagan, S. Cell biology meets biophysics to unveil the different mechanisms of penetratin internalization in cells. *Biochimica et biophysica acta* **2010**, *1798*, 2231-2239, doi:10.1016/j.bbamem.2010.02.009.

168. Biswas, S.; Torchilin, V.P. Nanopreparations for organelle-specific delivery in cancer. *Advanced drug delivery reviews* **2014**, *66*, 26-41, doi:https://doi.org/10.1016/j.addr.2013.11.004.

169. Kellar, A.; Egan, C.; Morris, D. Preclinical murine models for lung cancer: clinical trial applications. *BioMed research international* **2015**, *2015*, doi:https://doi.org/10.1155/2015/621324.

170. Lushchak, V.I. Glutathione homeostasis and functions: potential targets for medical interventions. *Journal of amino acids* **2012**, *2012*, doi:10.1155/2012/736837.

171. A Elkhodiry, M.; A Husseini, G.; Velluto, D. Targeting the folate receptor: effects of conjugating folic acid to DOX loaded polymeric micelles. *Anti-Cancer Agents in Medicinal Chemistry (Formerly Current Medicinal Chemistry-Anti-Cancer Agents)* **2016**, *16*, 1275-1280, doi:https://doi.org/10.2174/1871520616666160219161600.

172. Fernández, M.; Javaid, F.; Chudasama, V. Advances in targeting the folate receptor in the treatment/imaging of cancers. *Chemical science* **2018**, *9*, 790-810, doi:10.1039/C7SC04004K.

173. Ghosh, P.; Yang, X.; Arvizo, R.; Zhu, Z.-J.; Agasti, S.S.; Mo, Z.; Rotello, V.M. Intracellular delivery of a membrane-impermeable enzyme in active form using functionalized gold nanoparticles. *Journal of the American Chemical Society* **2010**, *132*, 2642-2645, doi:https://doi.org/10.1021/ja907887z.

174. Gonda, A.; Zhao, N.; Shah, J.V.; Calvelli, H.R.; Kantamneni, H.; Francis, N.L.; Ganapathy, V. Engineering tumor-targeting nanoparticles as vehicles for precision nanomedicine. *Med one* **2019**, *4*, doi:10.20900/mo.20190021.

175. Sindhwani, S.; Syed, A.M.; Ngai, J.; Kingston, B.R.; Maiorino, L.; Rothschild, J.; MacMillan, P.; Zhang, Y.; Rajesh, N.U.; Hoang, T.; et al. The entry of nanoparticles into solid tumours. *Nat Mater* **2020**, *19*, 566-575, doi:10.1038/s41563-019-0566-2.

176. Longmire, M.R.; Ogawa, M.; Choyke, P.L.; Kobayashi, H. Biologically optimized nanosized molecules and particles: more than just size. *Bioconjug Chem* **2011**, *22*, 993-1000, doi:10.1021/bc200111p.

177. Aghajani, M.H.; Pashazadeh, A.M.; Mostafavi, S.H.; Abbasi, S.; Hajibagheri-Fard, M.-J.; Assadi, M.; Aghajani, M. Size Control in the Nanoprecipitation Process of Stable Iodine (127 I) Using Microchannel Reactor—Optimization by Artificial Neural Networks. *Aaps Pharmscitech* **2015**, *16*, 1059-1068, doi:https://doi.org/10.1208/s12249-015-0293-1.

178. Molina, A.M.; Morales-Cruz, M.; Benítez, M.; Berríos, K.; Figueroa, C.M.; Griebenow, K. Redox-sensitive cross-linking enhances albumin nanoparticle function as delivery system for photodynamic cancer therapy. *Journal of nanomedicine & nanotechnology* **2016**, *6*, doi:10.4172/2157-7439.1000294.

179. Müller, F.n.; Graziadei, A.; Rappsilber, J. Quantitative photo-crosslinking mass spectrometry revealing protein structure response to environmental changes. *Analytical chemistry* **2019**, *91*, 9041-9048, doi:https://doi.org/10.1021/acs.analchem.9b01339.

180. Parrish, A.B.; Freel, C.D.; Kornbluth, S. Cellular mechanisms controlling caspase activation and function. *Cold Spring Harbor perspectives in biology* **2013**, *5*, a008672, doi:10.1101/cshperspect.a008672.

181. Sakai, Y.; Sasahira, T.; Ohmori, H.; Yoshida, K.; Kuniyasu, H. Conjugated linoleic acid reduced metastasized LL2 tumors in mouse peritoneum. *Virchows Archiv* **2006**, *449*, 341-347, doi:https://doi.org/10.1007/s00428-006-0249-7.

182. Papageorgiou, A.; Stravoravdi, P.; Sahpazidou, D.; Natsis, K.; Chrysogelou, E.; Toliou, T. Effect of navelbine on inhibition of tumor growth, cellular differentiation and estrogen receptor status on Lewis lung carcinoma. *Chemotherapy* **2000**, *46*, 188-194, doi:https://doi.org/10.1159/000007277.

183. Peng, X.-H.; Majumdar5F, D.; Shin, D.M. Applications of Nanotechnology in Imaging and Therapy of Cancer. In *Current Advances in the Medical Application of Nanotechnology*; Bentham Science Publishers: 2012; p. 43.

184. Delbridge, A.R.; Valente, L.J.; Strasser, A. The role of the apoptotic machinery in tumor suppression. *Cold Spring Harb Perspect Biol* **2012**, *4*, doi:10.1101/cshperspect.a008789.

185. Majtnerova, P.; Rousar, T. An overview of apoptosis assays detecting DNA fragmentation. *Mol Biol Rep* **2018**, *45*, 1469-1478, doi:10.1007/s11033-018-4258-9.

186. Lee, J.H.; Li, Y.C.; Ip, S.W.; Hsu, S.C.; Chang, N.W.; Tang, N.Y.; Yu, C.S.; Chou, S.T.; Lin, S.S.; Lino, C.C.; et al. The role of Ca2+ in baicalein-induced apoptosis in human breast MDA-MB-231 cancer cells through mitochondria- and caspase-3-dependent pathway. *Anticancer Res* **2008**, *28*, 1701-1711.

187. Rizvi, S.A.A.; Saleh, A.M. Applications of nanoparticle systems in drug delivery technology. *Saudi pharmaceutical journal* **2018**, *26*, 64-70, doi:https://doi.org/10.1016/j.jsps.2017.10.012.

188. Lu, J.; Zhao, W.; Huang, Y.; Liu, H.; Marquez, R.; Gibbs, R.B.; Li, J.; Venkataramanan, R.; Xu, L.; Li, S. Targeted delivery of doxorubicin by folic acid-

decorated dual functional nanocarrier. *Molecular pharmaceutics* **2014**, *11*, 4164-4178, doi:https://doi.org/10.1021/mp500389v.

189. Liu, F.; Chen, Y.; Li, Y.; Guo, Y.; Cao, Y.; Li, P.; Wang, Z.; Gong, Y.; Ran, H. Folate-receptor-targeted laser-activable poly (lactide-co-glycolic acid) nanoparticles loaded with paclitaxel/indocyanine green for photoacoustic/ultrasound imaging and chemo/photothermal therapy. *International journal of nanomedicine* **2018**, *13*, 5139, doi:10.2147/IJN.S167043